CO_2 SELECTIVE METAL ORGANIC FRAMEWORK ZIF-8 MODIFIED THROUGH IL ENCAPSULATION: A COMPUTATIONAL STUDY

A Thesis

by

AMRO MAMOON OSMAN MOHAMED

Submitted to the Office of Graduate and Professional Studies of
Texas A&M University
in partial fulfillment of the requirements for the degree of

MASTER OF SCIENCE

Chair of Committee,	Ioannis G. Economou
Committee Members,	Marcelo Castier
	Othmane Bouhali
Head of Department,	M. Nazmul Karim

May 2018

Major Subject: Chemical Engineering

ABSTRACT

Nano-scale porous solids are alternate candidates for CO_2 handling towards the development of materials for post-combustion CO_2 capture with low energy demands and milder operating conditions. Zeolitic imidazolate framework-8 (ZIF-8) is one of the most investigated Metal Organic Frameworks (MOFs) for separation of gas mixtures. In this work, we investigate a new approach of tailoring MOF separation efficiency, by confining pairs of three different ionic liquids (ILs) in the cages of ZIF-8 (IL@ZIF-8). ILs comprising 1-butyl-3-methylimidazolium cation [$bmim^+$] and three distinct anions, bis(trifluoromethylsulfonyl)imide [Tf_2N^-], tricyanomethanide [TCM^-], and tertracyanoborate [$B(CN)_4^-$], were used in this study. Molecular force fields, previously developed by Economou and co-workers for both the ZIF-8 framework and the ILs, are used in the molecular simulations of these systems. Monte Carlo simulations, employing an appropriate set of constraints, are utilized for the calculation of sorption of CO_2/CH_4 and CO_2/N_2 mixtures. The results show an increase of the CO_2 sorption compared to pristine ZIF-8 due to the presence of the IL, which increases the CO_2 selectivity and capacity dramatically. Recently reported experiments agree with our findings. Moreover, we explore how CO_2 selectivity and capacity vary with IL composition in the IL@ZIF-8 complex, as a mean to define an optimum IL composition in terms of the separation efficiency. As a result of the pore volume reduction in the structure, a tradeoff between capacity and selectivity is present. Therefore, a sorbent selection parameter that combines working capacity and equilibrium selectivity proposed by Range and Yang, alongside a regenerability factor, are used to further determine the best sorbent among other known

materials. The regenerability factor is adopted to reflect the fractional percentage of adsorption sites that are available for regeneration

ACKNOWLEDGEMENTS

I would like to thank my committee chair, Dr. Ioannis G. Economou, and my committee members, Dr. Marcelo Castier, and Dr. Othmane Bouhali, for their guidance and support throughout the course of this research.

Also, I would like to thank Dr. Panagiotis Krokidas for his help with molecular simulation techniques and gas separation topics.

Thanks also go to my friends and colleagues and the department faculty and staff for making my time at Texas A&M University a great experience.

CONTRIBUTORS AND FUNDING SOURCES

This work was supervised by a thesis committee consisting of Professor Ioannis Economou [Principal Advisor] and Professors Marcelo Castier of the Chemical Engineering Program and Professor Othomane Bouhali of the Science Program of Texas A&M University at Qatar.

This work was made possible thanks to financial support from NPRP grant number 7-042-2-021 (Qatar National Research Fund of Qatar Foundation). We are grateful to the High Performance Computing Center of Texas A&M University at Qatar for generous resource allocation.

TABLE OF CONTENTS

Page

LIST OF FIGURES

Page

LIST OF TABLES

Page

1. INTRODUCTION AND MOTIVATION

CO_2 emissions from industrial sources and power plants affect the environment and are directly linked to global warming and climate change. The Intergovernmental Panel on Climate Change (IPCC) predicted that the mean global temperature could rise by as much as 1.9 ^oC, by the year 2100 [1]. Combined with the unprecedented high CO_2 levels in the atmosphere of more than 400 ppm [2], the scientific community faces challenging problems related to the mitigation of emissions, refinement of energy production using fossil fuels, as well as methods for Carbon Capture and Sequestration (CCS). The latter although a promising approach usually it consists of cycles of subsequent heating and cooling which are energy demanding [2]–[5]. A major research effort worldwide is on the development of materials with high CO_2 selectivity, capacity, and permeability for post-combustion CO_2 capture. For this purpose, nanomaterials with pore diameters covering a broad range in the nm-μm scale can be employed. Typical examples are shown in Figure 1.

In order to separate gas mixtures, one may exploit adsorption based methods or kinetic driven separation. Adsorption based gas separation is a process based on the interaction of gases with the surface of the pores, which leads to their energetically favorable positioning at areas of the pores called "sorption sites". The affinity of various species with the wall differs, leading to preferential adsorption between components in a gas mixture. Kinetic driven separation is based on size and shape differences between the species of a mixture and morphology of the solids pores. The relatively small pores of the material slow down the larger components, while smaller components diffuse at higher rates and a separation of the mixture

is achieved [6], [7]. An example of kinetic separation refers to the separation of air in carbon molecular sieves, in which O_2 diffuses 30 times faster than N_2 [8].

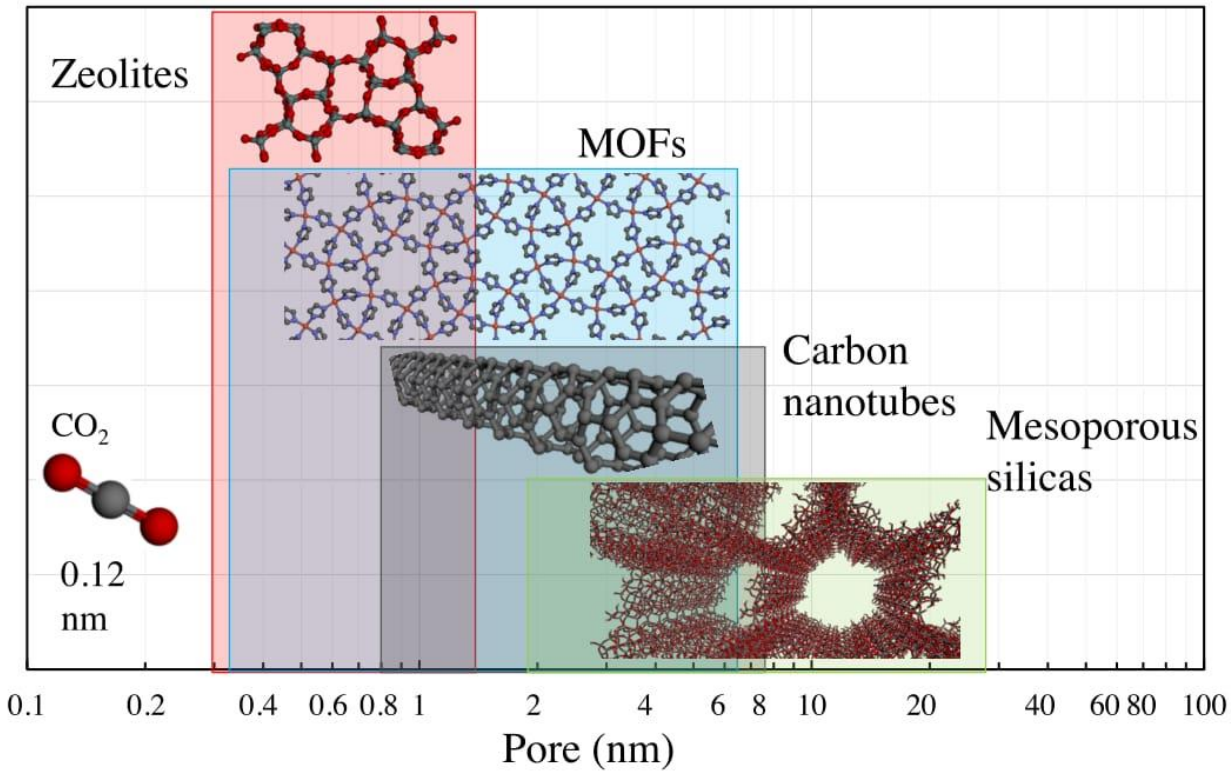

Figure 1: Pore size variation for various families of nanoporous materials.

In an adsorption process, molecules, atoms, or ions, diffuse to the surface of a solid, where they bond with the solid surface or are held by weak intermolecular forces. Adsorbed solutes are referred to as adsorbates, whereas the solid material is the adsorbent [9].

During adsorption, the solid separating agent becomes saturated or nearly saturated with adsorbates transferred from the fluid phase. To recover the sorbed substances and allow the sorbent to be reused, the adsorbent is regenerated by desorbing the sorbed species. Accordingly, these two separation operations are carried out cyclically. The adsorption process

may be classified as purification or bulk separation, depending on the concentration in the feed of the components to be adsorbed.

The capacity of a material is considered a substantial element in selecting adsorbents as it directly influences the capital cost of an adsorber. In general, the term selectivity is defined as the ratio of the capacity of an adsorbent for one component to its capacity for another. It has a similar implication as the relative volatility in ordinary thermal distillation. The higher the selectivity, the smaller the equipment required to perform a targeted separation process. Besides saturation capacity and selectivity, regaining the capacity is also an indispensable aspect.

The regeneration of an adsorbent is usually attained by pressure swing (change in pressure). Thermal swing (change in temperature), or chemical treatment (by supercritical extraction or elution) are additional methods that can be utilized for the regeneration [10]. Breakthrough curves, which show the concentration of the adsorbate of interest in the effluent leaving a fixed bed column, are required to identify kinetic and transport properties for adsorption. Obtaining a sharp breakthrough curve is desirable for rapid adsorption. Adsorption isotherm type I is a favorable isotherm (concave downward (section 2.3)). Moreover, for commercial applications, a sorbent should be compatible with the separation conditions and have low cost. An adsorbent must have high stability, high resistance to fouling and excellent mechanical properties such as hardness and strength (attrition resistance due to equipment vibration and volumetric flow rate). Further, it is important that the adsorbent does not promote undesired chemical reactions considering feed and regenerant streams [10].

Depending upon the forces between fluid molecules and solid molecules, adsorption may be classified as physical adsorption (van der Waals adsorption) or chemisorption

(activated adsorption). Physical adsorption from a gas occurs when attractive intermolecular forces between solid and gas molecules are more significant than those between gas molecules so that gases adsorb in higher densities than bulk densities. In effect, the resulting adsorption is like condensation, which is exothermic and accompanied by a release of heat. The magnitude of the adsorption heat can be higher or lower than the heat of vaporization and varies with the amount of adsorption. Chemisorption includes the formation of chemical bonds between adsorbent and adsorbate in a monolayer, where typically the amount of heat released is larger than the heat of vaporization. In adsorption processes, physical adsorption is preferred as the heat of adsorption is usually lower than the heat of vaporization. Low heat of adsorption values are looked-for since they give a measure of the regeneration energy necessary [10].

ZIF-8 (ZIF: Zeolitic imidazolate framework) is one of the most investigated Metal Organic Frameworks (MOFs) for gas mixtures separations, and that is due to its excellent thermal and chemical stability, and its robust structure [11], [12]. ZIF-8 is composed by interconnecting Zn atoms with the organic linker in 2-methylimidazolate, where Zn atom is connected with four N atoms to form a tetrahedral as shown in Figure 2. We have higher partial charges on Zn (1.34 e), N (-0.68 e), and C2 (0.75 e), and lower partial charges on H atoms. ZIF-8 has sodalite topology and comprise of a cubic unit cell (length = 16.991 $\dot{A}$). Also, ZIF-8 is characterized by spherical cages, called sodalite cages. The sodalite cages are connected by 4-ring windows, and separated by 6-ring windows of small apertures. According to experimental data from the literature, gas molecules characterized by a size larger than the aperture accessing the primary pores can diffuse in ZIF-8 [13]–[15]. ZIFs are unique in terms of adaptability to modify their frameworks towards the desired pore size through metal

substitution [16]–[18] or ligand exchange [19], [20]. These methods mainly target kinetic-based selectivity.

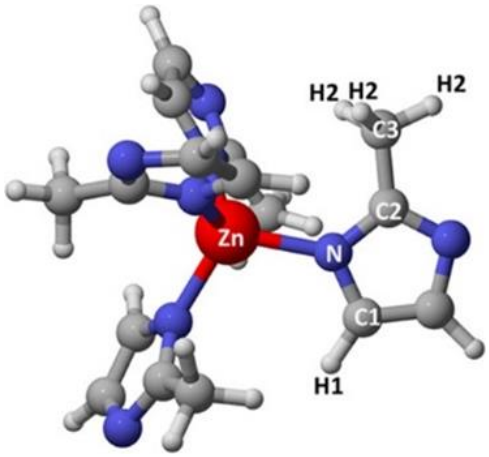

Figure 2: Basic Zn(N-mIM)$_4$ unit of ZIF-8 framework. (Adapted from [50])

Ionic liquids (ILs) are salts comprised of an organic cation and an organic/inorganic anion, which maintain liquid phase at room temperatures, and are formed by positive and negative ions. ILs are non-volatile, non-flammable, with high thermal stability and undertake competitive adsorption capacity for gases. These aforementioned properties reflect upon the span of ILs' possible applications such as separation techniques [21], catalysis [22], [23] and extraction [24]. Different ILs have been involved in chemical processes playing an effective role in improving catalytic reactions. The reactions include Friedel-Craft, halogenation, and Diel-Alder reactions [53]. Throughout cation or anion selection, one can control the IL physiochemical properties. Among the enormous number of ILs, the imidazolium class is the most widely investigated [25], [26].

A new approach for improving the sorption-based selectivity of MOFs is the cage modification with cavity occupants (cage decoration), in which additional molecules are incorporated in the pores of the material [27]. This relatively new approach enhances the

adsorption affinity for targeted molecules. Recent findings show that ILs are promising as adsorption selective materials towards CO_2 [26], [28].

Ban et al. [29] employed cage decoration to develop a new ZIF type (namely IL@ZIF-8), by introducing IL molecules as cavity occupants in the ZIF-8 framework. This material exhibits enhanced CO_2 selectivity in mixtures [29], which is higher compared to both in the pure ZIF framework and in bulk IL [29], [30]. More specifically, Ban et al. reported a 5-fold increase of CO_2/CH_4 and CO_2/N_2 ideal separation in IL@ZIF-8 membrane. This corresponds to an ideal sorption selectivity (ratio of adsorbed quantities): $CO_2/CH_4 = 100$; $CO_2/N_2 = 41$. The selection of IL 1-butyl-3-methylimidazolium bis(trifluoromethyl-sulfonyl) imide ($[bmim^+][Tf_2N^-]$) was justified since $[Tf_2N^-]$ is favorable towards CO_2 adsorption [31] and $[bmim^+]$ provides the sufficient cavity occupancy [29], [32].

The concept of IL encapsulation in the ZIF cages takes advantage of hybrid materials called mixed matrix membranes (MMMs), in which a polymer matrix is filled with inorganic [33] or inorganic-organic hybrid [34] nanoporous material. This approach combines the transport performance of said fillers with the processibility, low cost and mechanical properties of the polymers [35]. MMMs are introduced to further develop membrane with extraordinary separation performance. Many IL/filler/polymer MMMs were prepared and their performance checked for gas separation [25]. IL@ZIF-8 employment as filler in polysulfone (PSF) polymer matrix yields remarkable permeability and selectivity that places this hybrid material on the top of the competition against the remaining polymer membranes studied for CO_2/CH_4 and CO_2/N_2 separation.

In fact, IL@ZIF-8 composites, prepared by ionothermal synthesis, were inserted at different volume fractions in the polymer matrix. It was revealed that the volume fraction has

an important role in determining the efficiency of the separation. At the optimum volume fraction, the CO_2 selectivity of the MMM was probed against different fillers, ZIF-8, IL, and IL-ZIF-8 in PSF. Ban showed that IL@ZIF-8/PSF MMM is superior over all other combinations in both CO_2/CH_4 and CO_2/N_2 selectivities [29].

A limited number of computational based studies investigated MOF supported ILs (IL@MOF) to study CO_2 adsorption and detect preferential adsorption of CO_2 over N_2 [36]–[38]. In these studies, molecular representation and interaction between molecules were achieved by utilizing commercial codes and generalized (generic) force fields. In addition, these studies were reported without considering the influence of IL composition on the adsorption selectivity. Also, the impact of IL anion has not been discussed adequately.

Although the outcome of such alteration is impressive, similar experimental attempts in ZIF-8 are very rare, due to the demanding and complex synthesis. Molecular simulation can overcome such intricacies, help the design and further investigation of such systems, allowing scientists to avoid dealing with inherently dangerous systems or experiments conducted at elevated temperatures and pressures. In addition, it comprises a tool that offers remarkable insight into processes taking place in principal at a molecular level by providing a path from the microscopic details of a system to macroscopic properties of industrial importance [39]. Consequently, it has applications in many fields. For instance, in material science and engineering, computational biology and computational chemistry. More specifically, it has been applied successfully in zeolites, MOFs and ZIFs [40]–[44].

One of the most vital pieces in molecular simulations is the force field. In a molecular model, force field is the combination of functional form with a set of parameter that describes

the interaction between molecules. Force fields play a major role in determining the accuracy of molecular modeling studies.

Regarding the ongoing research on ZIF-8, sorption of gas molecules has been analyzed successfully in ZIF-8 with MC simulations [45]–[47], which is regarded as the most widely used computational approach for the estimations of nanoporous gas adsorption properties. Although the computational studies of IL encapsulation in ZIF-8 are helpful, either they are simple investigations on the structure conformation of the IL pair in the framework [29] or sorption selectivity calculations with force fields developed for generic purposes [48], which, according to our opinion, do not provide the level of accuracy required in calculations for a more thorough investigation of this system.

In light of Ban et al. findings, we solely investigate here the ZIF-8 separation performance and the merits of the introduction of ILs in the ZIF framework by employing MC simulations. We study the effect of ($[bmim^+][Tf_2N^-]$) encapsulation in ZIF-8 framework. In our study, we utilized force fields for the $[bmim^+][Tf_2N^-]$ IL [49] and the ZIF-8 framework [50] developed by the research group of the principal supervisor of this thesis. The performances of force fields have been very successful in multiple applications [18], [49], [51]. Moreover, we compare our CO_2 selectivity and capacity results with the recently reported experiments by Ban et al.

2. LITERATURE REVIEW

2.1. Carbon capture techniques

The most important of the greenhouse gases (GHGs) is by far CO_2 [52]. Besides CO_2 being the driving force of pollution by human activities, CH_4 is considered the second highest contributor to the climate change with one-fifth of the impact. Nitrous oxide is third in the impact with 6% of the overall impact [52]. Carbon capture and storage (CCS) has been highlighted as an effective way to mitigate the CO_2 emission to the atmosphere. Beside CCS, other approaches are considered and investigated. These include enhancing the efficiency of existing energy conversion and end-use, leaning towards the use of renewable energy and less intensive carbon fuels (natural gas), and improve biological based absorption capacity in soils. The process of CCS involves capturing, compressing, transporting and storing CO_2 in deep geological formations [53]. The obstacles that are needed to overcome among others is the energy requirement and cost associated with gas separation.

There are three main systems for capturing CO_2, here; the three schemes will be discussed in terms of their features and drawbacks. First, the post-combustion processes are associated with capturing CO_2 from flue gases streams prior to the discharge practice to the atmosphere. Flue gases are usually at atmospheric pressure, and the composition of the stream varies depending on the fuel utilized [54]. The advantage of this system is that the installation of the carbon capture unit does not require major modification to the plant. Gas absorption on solvents is the favored option to perform post-combustion [53]. Absorption and stripping for the removal of acid gases (CO_2, SO_2, H_2S) is a mature technology and it was patented in 1930 [55]. The performance of such CO_2 removal technique using monomethanolamine (MMA) [56] and monoethanolamine (MEA) [57] has been discussed in the literature. Other emerging

and promising technologies include adsorption processes by solids and membranes separations. Disadvantages of post-combustion systems include the low CO_2 partial pressure in the flue gas stream, energy extensive process, and captured CO_2 is at pressure low for storage purposes. Figure 3 shows a process flow diagram for post-combustion CO_2 capture system utilizing MEA, highlighting the adsorber and stripper columns.

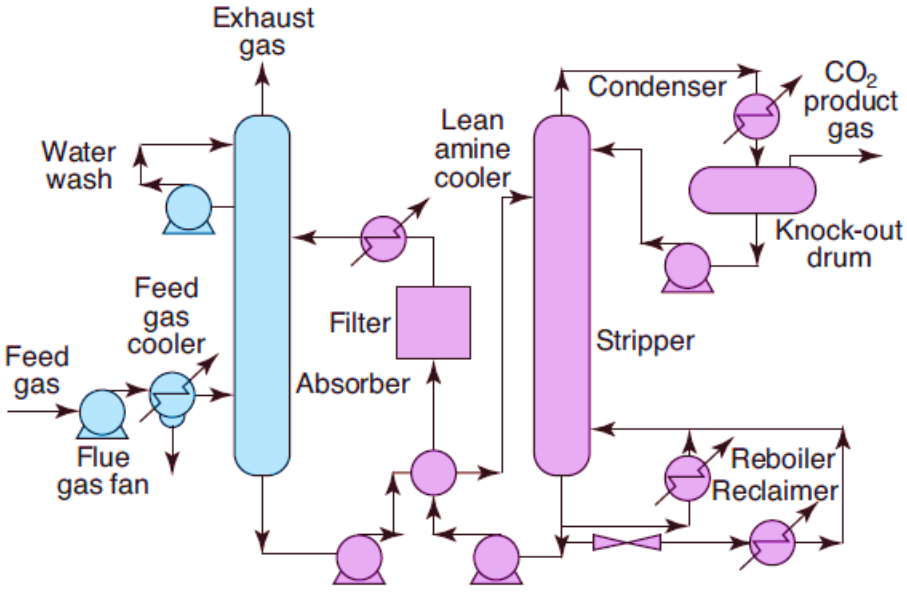

Figure 3: Process flow diagram for CO_2 capture from flue gas with chemical solvent. (Adapted from [56])

In the second system, the pre-combustion processes involve CO_2 separation from pre-combusted fuels [58]; in other words, prior to fuel entry to a combustion chamber. The shift catalytic converter reacts the synthesis gas, mainly composed of CO and H_2 (biomass or fossil fuel after reforming/gasification stage), with additional steam to obtain CO_2 and surplus of H_2 following water-gas-shift reaction. Subsequently, CO_2 is separated, the H_2-rich stream is utilized as a fuel for different application/operating units in the plant. A schematic flowsheet illustrated the main section of a pre-combustion CO2 capture scheme is shown in Figure 4.

Commercially, this technology is applied in many downstream production processes, for instance, ammonia production. The process is characterized by high operating pressure, and higher CO_2 concentration in the stream than those in flue gas [53], [59]. The implementation is constraint by the high capital cost and relatively high energy requirement.

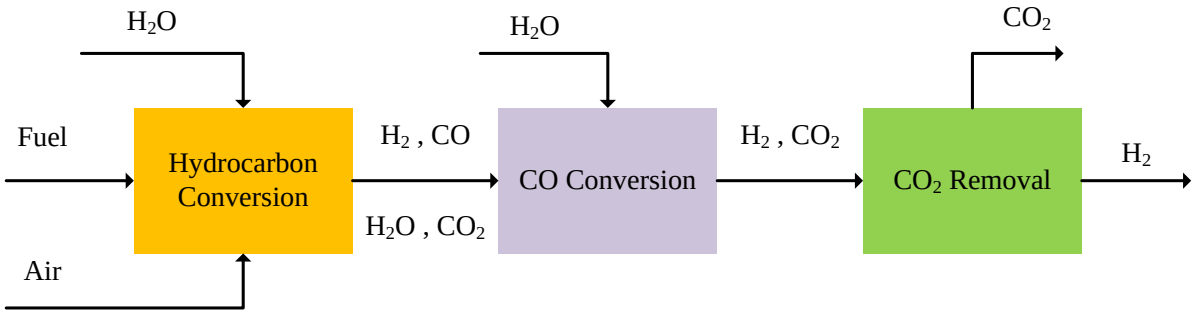

Figure 4: The basic sections of a pre-combustion CO_2 capture process. (Adapted from [58])

The third system, the oxy-fuel process involves the injection of pure O_2, produced from cryogenic air separation units (ASUs) by separating O_2 from N_2 in the combustion chamber as a replacement for air. CO_2 and water are the main constituents of the flue gas. When combusting fossil fuel with almost pure O_2 feed, the flue gas produced contains above 90% of CO_2, which allows for inexpensive purification process from noble gases and NO_x [60], [61]. A simple block chart of the oxy-fuel process is shown in Figure 5. However, one of the main challenges that faces oxy-fuel combustion is the high energy penalty associated with ASU. Another issue is that the method has not been yet established on a large scale [61].

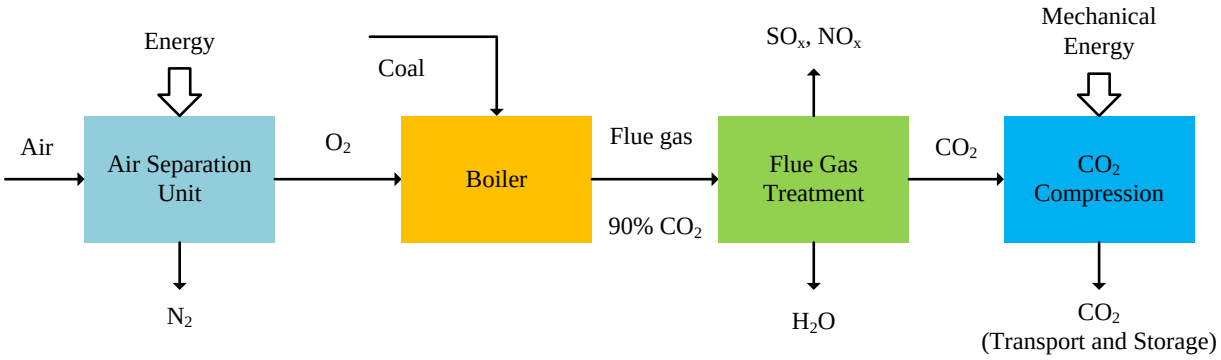

Figure 5: Block flow diagram of oxy-fuel process illustrated for coal-fired boilers. (Adapted from [60])

An emerging combustion technique is the so-called Chemical-looping combustion (CLC). The process was first proposed by Lewis et al. [62]. CLC involves two reactors (air reactor and fuel reactor) in the combustion process as revealed in Figure 6. Typically, the process is conducted in a fashion similar to Fluid Catalytic Cracking (FCC), that it, using a fluidized bed reactor setup. So, the process allows for the intrinsic removal of CO_2 from the fuel gas. This is accomplished by introducing a metal oxide (oxides of Fe, Cu, Ni, Mn, and CO metals are typically used) as oxygen carriers; thus avoiding direct reaction between fuel and air. Gaseous or solid fuel is introduced into the fuel reactor; where, an endothermic reaction takes place between hydrocarbons with the metal oxide. The gaseous stream containing CO_2 and water vapor is produced, and water is separated inexpensively by condensation. For regeneration purposes, the reduced metal oxide reacts with oxygen in the air reactor to regenerate the carrier. Therefore, if the loop seals work properly, portion of energy demand for gas separation would be saved, since CO_2 is not diluted with N_2 [63].

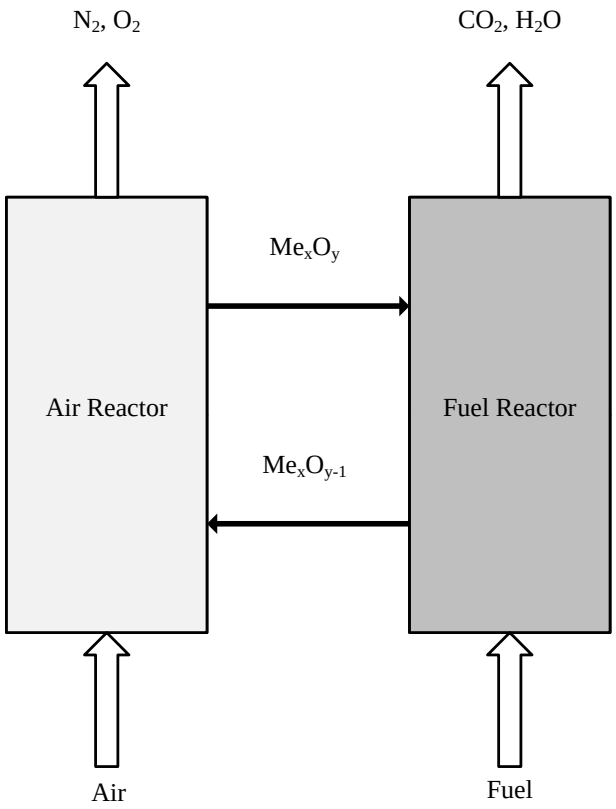

Figure 6: Chemical-looping combustion setup. (Adapted from [63])

2.2. Molecular simulation

A brief introduction to molecular simulation is provided in this section. A significant amount of information must be provided and clearly specified to perform molecular simulations. Such information includes the geometry of the system on the study, the molecular connectivity, the interaction energies (potential), and the thermodynamic constraints. Simulation products can provide a mean to examine theory and test accuracy of models as can be illustrated by Figure 7. Force field based computational approaches (molecular mechanics) have the capability to study larger systems than quantum mechanical calculations. Unlike quantum mechanical methods, molecular mechanics computes the system energy based on the nuclear positions only. In other words, it discards the electronic motion. Monte Carlo (MC)

and molecular dynamic (MD) simulation types of force field based approaches calculate a broad range of properties (thermophysical, transport, and structural), while quantum mechanical calculations are more appropriate to examine chemical properties such as bond breakage and formation [64], [65]. MD is a deterministic approach, where it is feasible to predict the trajectory of the system as a function of positions, velocities, and accelerations. In other words, all microstates are connected relative to time in MD simulation. Unlike MD simulation, in MC simulation, the time factor is eliminated, where a given configuration depends only on the previous configuration (Markov chain) [64].

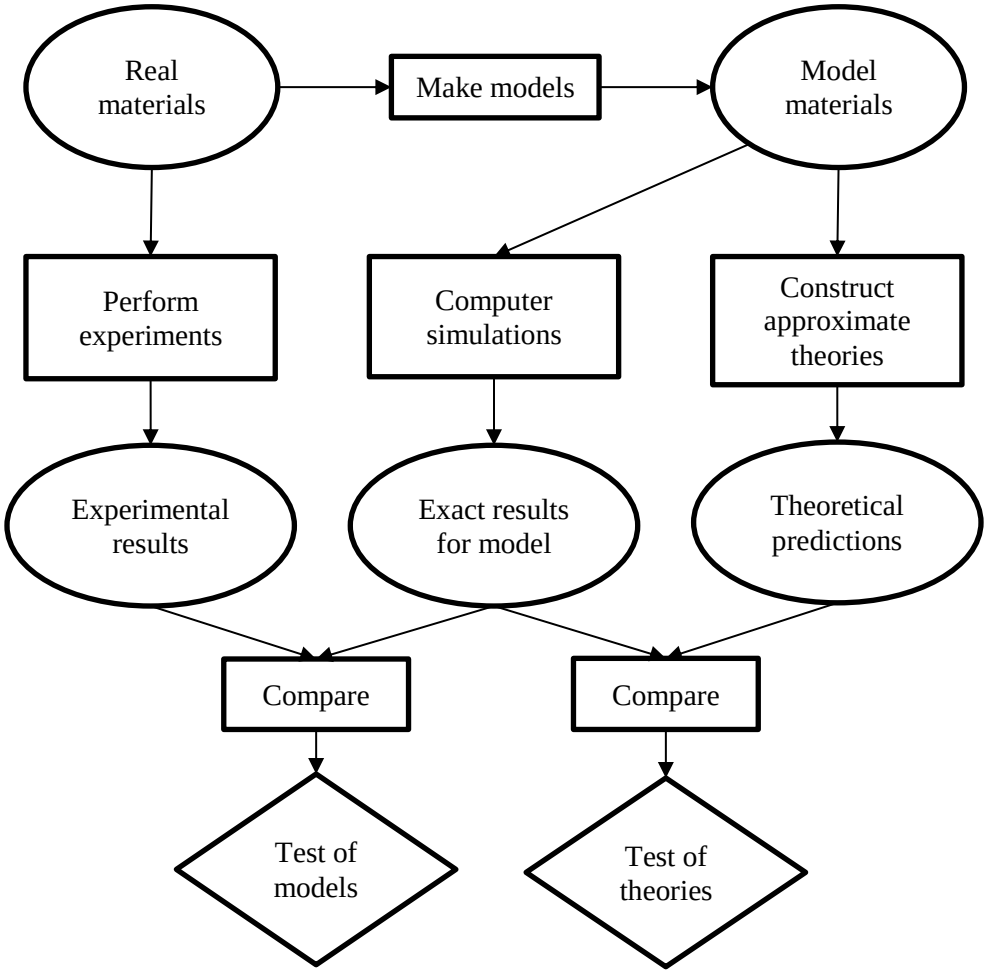

Figure 7: The connection between experiment, theory, and computer simulation. (Adapted from [66])

The main difference between these two methods is the element of time (MD) and the stochastic generation of configuration (MC). In MD, the total energy has a contribution from kinetic and potential energies, whereas the total energy in MC is evaluated from the potential energy function. Traditionally, MD is performed under thermodynamic constraints of the microcanonical ensemble (maximizing entropy). On the other hand, MC is more associated with the canonical ensemble (minimizing Helmholtz free energy). Because MD simulation investigates how a given system propagate in time, it has the advantage over MC methods to calculate time dependent properties (such as transport properties). On the other hand, employing MC simulation is considered to be convenient especially in constant temperature and pressure simulations, and gives flexibility in particular applications [67]. In addition, the non-physical moves in MC simulation can assist in exploring phase space in some cases. Therefore, it is more effective for conformational changes, unlike MD which can provide useful local phase space exploration. Some efforts have been devoted towards the development of hybrid MD/ MC methods to enhance sampling and convergence. The hybrid algorithm makes use of both molecular simulation procedures by alternating between them [68] or by following an MD simulation by Metropolis criterion [69], [70].

2.2.1. Monte Carlo simulation

The following section will demonstrate how MC simulation is capable of computing thermodynamic properties, considering that the simulation does not include the contribution from momentum. MC samples a 3N-dimensional space of the particles' position, while the phase space is 6N- dimensional. We can demonstrate this by looking at the canonical (NVT) partition function for N indistinguishable particles, each of mass m:

$$Q_{NVT} = \frac{1}{N!}\frac{1}{h^{3N}} \iint dp^N dr^N \exp\left[-\frac{\mathcal{H}(p^N, r^N)}{k_B T}\right] \quad (1)$$

where $\mathcal{H}(p^N, r^N)$ is the Hamiltonian that represents the total energy of the system (kinetic+ potential energy), N is the number of particles and r^N and p^N are the position and momentum vectors, respectively:

$$r^N = (x_1, y_1, z_1, x_2, \dots, y_N, z_n) \quad (2)$$

$$p^N = (p_{x,1}, p_{y,1}, p_{z,1}, p_{x,2}, \dots, p_{y,N}, p_{z,N}) \quad (3)$$

Given that the potential energy $\mathcal{U}$ is not a function of velocities, the double integral can be split into two parts (momentum and position), in which the integration over the momentum has an analytical solution:

$$\int \mathrm{dp^N} \exp\left[-\frac{|p|}{2mk_B T}\right] = (2\pi m k_B T)^{\frac{3N}{2}} \quad (4)$$

$$Q_{NVT} = \frac{1}{N!}\left(\frac{2\pi m k_B T}{h^2}\right)^{\frac{3N}{2}} \int dr^N \exp\left[-\frac{\mathcal{U}(r^N)}{k_B T}\right] \quad (5)$$

The second part of the partition function (integration over the positions) is named the configurationally internal:

$$Z_{NVT} = \int dr^N \exp\left[-\frac{\mathcal{U}(r^N)}{k_B T}\right] \quad (6)$$

The partition function can be divided into an ideal and a non-ideal part. This is shown by assigning zero interaction between the molecules

$$\mathcal{U}(r^N) = 0 \Rightarrow Z_{NVT} = V^N \Rightarrow Q_{NVT}^{ideal} = \frac{1}{N!}\left(\frac{2\pi m k_B T}{h^2}\right)^{\frac{3N}{2}}$$

$$Q_{NVT}^{excess} = \frac{Q_{NVT}}{Q_{NVT}^{ideal}} = \frac{1}{V^N} \int dr^N \exp\left[-\frac{(r^N)}{k_B T}\right] \tag{7}$$

Based on statistical thermodynamics, thermodynamic quantities can be related to the canonical partition function [71], for instance:

$$\text{Internal energy } (U) = k_B T^2 \left(\frac{\partial \ln Q_{NVT}}{\partial T}\right)_{N,V} \tag{8}$$

$$\text{Entropy } (S) = k_B \ln Q_{NVT} + k_B T \left(\frac{\partial \ln Q_{NVT}}{\partial T}\right)_{N,V} \tag{9}$$

$$\text{Helmholtz free energy } (A) = -k_B T \ln Q_{NVT} \tag{10}$$

Whenever an integral cannot be resolved analytically, one may use numerical methodologies to evaluate the integral. Examples of numerical integration methods are trapezium rule and Simpson's rule (Kepler's rule) to approximate a definite integral. In our case, we need to evaluate the following multidimensional integral over the 3N degrees of freedom (average of potential energy):

$$\langle \mathcal{U}(r^N) \rangle = \int dr^N \mathcal{U}(r^N) \rho(r^N) \; ; \; \rho(r^N) = \frac{\exp\left[-\frac{\mathcal{U}(r^N)}{k_B T}\right]}{\int dr^N \exp\left[-\frac{\mathcal{U}(r^N)}{k_B T}\right]} \tag{11}$$

It is unrealistic to estimate this integral using Simpson's rule, since a massive amount of points are essential to determine the integral in only one dimension. Consequently, scientists attempted to achieve this by simple MC integration (random analysis). The following steps are involved in estimating the average potential energy of a desired system as shown in Figure 8.

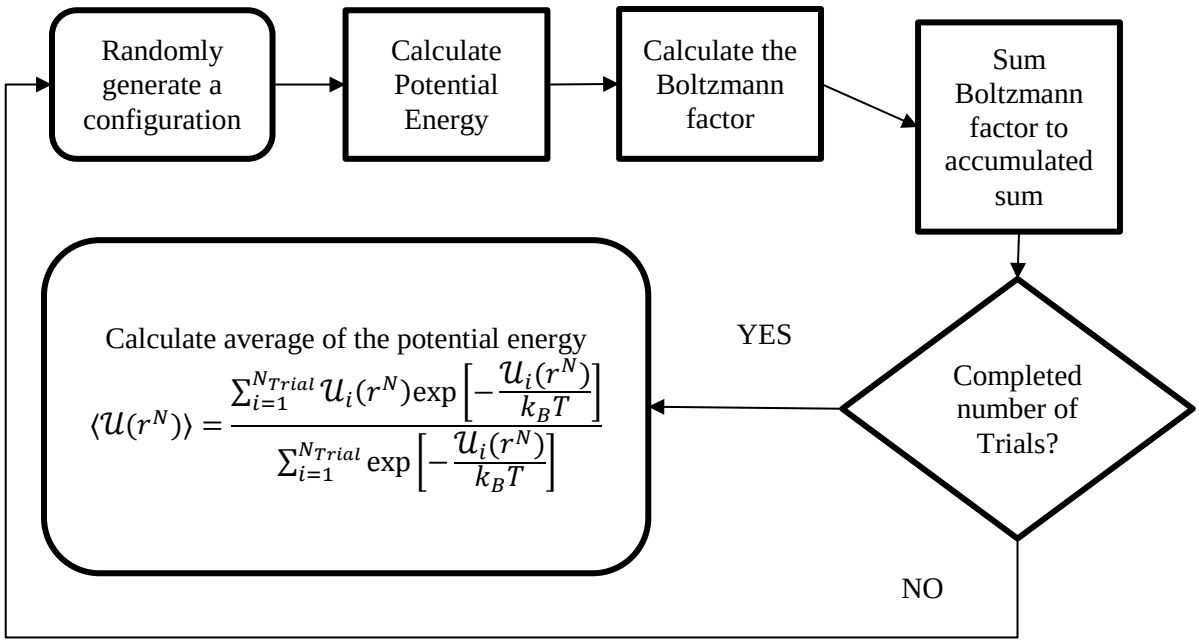

Figure 8: Flowchart of evaluating average of potential energy using simple MC simulation method. (Adapted from [64])

2.2.1.1. The Metropolis Monte Carlo method

The major issue that makes simple MC method impractical is that one or more pairs of molecules will overlap and the likelihood of this event increases with density [11]. Starting from an acceptable configuration is the initial and substantial step towards an efficient MC simulation. This step is followed by an algorithm which is biased to generate and converge to lower energy configurations which have significant contribution to the integral [64]. The averaging process must consider this bias and the most widely implemented MC method is the one reported by Metropolis et al [72].

To fully understand Metropolis method, Markov chains must be considered. The Markov chain is defined as a stochastic process that involves a sequence of trials. It has to fulfill two conditions. The outcome of each trial, first, depends solely on the outcome of the immediately preceding trial, and second it belongs to a countable set of outcomes. In this

algorithm, a transition probability matrix π is placed to link two states of the system, in which the matrix encloses all information on the evolution of the Markov chain [39], [64]. The probability of obtaining a system in a given state *i* is represented by p_i. Equilibrium distribution of the Markov chain, is reached by applying the transition matrix infinite times. An important characteristic of the limiting distribution is that it is independent of the initial conformation.

The Metropolis MC method starts with an arbitrarily overlap-free state of the system. Next, using random numbers, perturbation of a randomly selected particle's position (coordinates) is made from old positions (x_o, y_o, z_o) to new position (x_N, y_N, z_N) respecting a maximum displacement factor.

$$\begin{aligned} x_N &= x_O + \xi_x \delta r_{max} \\ y_N &= y_O + \xi_y \delta r_{max} \\ z_N &= z_O + \xi_z \delta r_{max} \end{aligned} \tag{12}$$

For each of the Cartesian coordinates, a unique random number [-1, 1] assigns (ξ_x, ξ_y, ξ_z) to a maximum allowable displacement δr_{max} which can be modified throughout the course of the simulation to sustain a particular acceptance ratio. In order to accept or reject a move, importance sampling is utilized, and one can define a parameter $\mathcal{P}$ [71].

$$\mathcal{P} = \exp\left(\frac{\Delta[-\mathcal{U}(r^N)]}{k_B T}\right) \tag{13}$$

There are two possible outcomes:

1- $\mathcal{P} > 1$; move is accepted to a lower energy configuration

2- $\mathcal{P} < 1$; move is subject to the second test where the acceptance condition is as follows,

$$rand(0,1) \leq \exp\left(\frac{\Delta[-\mathcal{U}(r^N)]}{k_B T}\right)$$

2.2.1.2. Monte Carlo simulation codes

Several simulation packages have been developed to study specific molecular simulation technique and applications. In Table 1, some simulations codes are listed with their molecular simulation capabilities in terms of simulation methods accessibility and designed applications. Other molecular simulation codes are presented by Dubbeldam et al. [73].

Table 1: Selected commercial and freely available molecular simulation codes

Code	Type of Simulation	Applications	Reference
DLPOLY	MD/ MC (Metropolis sampling)	Macromolecules/ polymers/ ionic systems/ solutions	[74]
TINKER	MD/ MC	biopolymers	[75]
LAMMPS	MC, MD	Biomolecules/ polymers/ metals/ semi-conductors	[76]
GROMACS	MD	Proteins/ lipids/ nucleic acids	[77]
MCPRO	MC	Peptides/ proteins/ nucleic acids	[78], [79]
Towhee	MC	Fluid phase equilibria	[80], [81]
MedeA Gibbs	MC	Gibbs ensemble/ adsorption isotherms	[82]
Cassandra	MC	oligomers/ILs/ organic compounds NVT/NpT/GCMC	[21,22]
MUSIC	Hybrid MC, MD and NEMD	Diffusion and adsorption in nanoporous/ GCMC/ NVT/NpT	[83]
RASPA	MC/MD/Optimization	CBMC/CFMC/Gibbs	[65]
MAPS	MC/MD	Polymers, nano-composites materials, biological and metallic systems	[84]

In this work, Cassandra Code (Version 1.2) [85], [86] was utilized throughout all MC simulations. Cassandra is an open source MC free software package developed by Prof. Ed

Maginn and co-workers at the University of Notre Dame (U-ND) that uses OpenMP parallelization. The current version of the code is capable of executing molecular simulations in a variety of ensembles. These are canonical (NVT), isothermal-isobaric (NpT), grand canonical (μVT), and Gibbs (NVT and NpT). A number of force field parameterization expressions are implemented in the code that covers small organic molecules, oligomers, and most importantly ILs. Moreover, the employed MC code uses a random number generator proposed by L'Ecuyer [87]. Inserting, deleting, and regrowing of a molecule is accomplished by the Configurational Bias Monte Carlo method (CBMC). Table 2 reviews the supported types of force fields and other options currently in the version 1.2 of the Cassandra code (user guide) [88].

Table 2: Supported options in Cassandra

Force field		**Supported Options**		
Bonded	Bond	Fixed		
	Angle	Fixed	Harmonic	
	Dihedral	OPLS	CHARMM	Harmonic
	Improper	Harmonic		
Non-bonded	Van der Waals	Mie	LJ (specific case of Mie potential)	
	Electrostatics	Coulombic		

Some features were introduced in version 1.2. Besides Ewald summation [89], the Dampled shifted force method [90] for computing long-range electrostatic energies is also available. Tail correction is established in the two alternatives accessible for repulsion-dispersion non-bonded interactions. For interactions between unlike atoms, two mixing rules are available in the code: The Lorentz-Berthelot (LB) and the geometric mixing rules. One worth mentioning point is that Cassandra does not support flexible bond lengths. Two ways

can be used to circumvent this, either by using equilibrium bond lengths as the fixed length or, by conducting minimization of energy through molecular mechanics and apply the bond length corresponding to the lowest energy. However, significant deviation from the equilibrium value is rather rare in molecular mechanics computations [64]. Energetic penalties are associated with the deviation of bonds and angles away from their reference values [64]. Many functional forms are used to model the variation of bond energy as a function of interatomic separation. One of these is the Morse potential which has the following form:

$$u(l) = D_e\{1 - \exp[-a(l - l_0)]\}^2 \tag{14}$$

where D_e is the depth of the potential energy minimum, and $a = \omega\left(\frac{\mu}{2D_e}\right)^{\frac{1}{2}}$, where μ is the reduced mass and ω is the frequency of the bond vibration. Because of the inefficient computation and the need for three parameters (D_e, a and l_0), the Morse potential form is not used in MD simualtions. Therefore, a simple approach is adopted in which the bond energy changes with the square of the displacement from the equilibrium bond length (Hooke's law):

$$u(l) = \frac{k_l}{2}(l - l_0)^2 \tag{15}$$

The harmonic functional from offers a good representation of the potential energy at the bottom of the potential well. However, it not accurate away from the equilibrium. Cubic, quadratic, and higher terms can be added to Hooke's law to obtain better accuracy away from equilibrium.

Force constant in angle bending potential (k_θ) are typically smaller than those in bond stretching, therefore, it requires less energy to distort an angle from equilibrium (reference) than to altering a bond length (compressing or stretching). The force field can be improved by higher order terms as well.

$$u(\theta) = \frac{k_\theta}{2}(\theta - \theta_0)^2 \tag{16}$$

To achieve desired conformation and geometry of molecules, and desired energy profiles, torsional terms and out-of-plane bending are incorporated in the force field. Most of the times, torsional potentials are expressed as a cosine series expansion (Equation 17).

$$u(\varphi) = \sum_{n=0}^{N} V_n \left[1 + \cos(n\varphi - \gamma)^2\right] \tag{17}$$

where V_n is the relative barriers to the rotation, n is the number of minimum points in the potential function, γ is the phase factor, and φ is the torsion angle. Correct modeling of dihedral angles correctly is substantial in computing liquids properties. There are various methods that can be used to incorporate out-of-plane bending. A first way is to describe an improper torsion angle in which a central atom is bonded to three atoms. Other ways to identify out-of-plane bending involve the calculation of the angle between the plane determined by the central atom and a bond from the central atom. The following harmonic functional form (Equation 18) is widely used in the calculation of improper energy.

$$u(\psi) = k_\psi(\psi - \psi_0)^2 \tag{18}$$

One conventional manner to represent the electronic properties of molecules is by assigning partial atomic point charges throughout the molecule. Then, the electrostatic interaction is calculated by Coulomb law.

$$u(r_{ij}) = \frac{1}{4\pi\epsilon_o}\frac{q_i q_j}{r_{ij}} \tag{19}$$

The same formula is used when calculating interactions between two molecules or between different sections of the same molecule. There are numerous techniques to determine the charges. Partial charges can be determined by MD or MC simulations to fit them to

reproduce some thermophysical properties. Moreover, there are some high-speed methods, which rely on information about the atoms and their connectivity in the molecule (Gasteiger and Marsili method [91]) which includes an iterative partial equalization of orbital electronegativity.

2.2.2. Ensembles

2.2.2.1. Grand canonical ensemble

In a setup that permits the simulation of open systems (exchange energy and mass with surroundings), grand canonical ensemble imposed variables are chemical potential, volume, and temperature. The system is coupled to heat bath and an infinite particles reservoir. Ensemble's partition function can be expressed as:

$$\Xi = \sum_{N} \left(Q_{NVT} \exp\left[\frac{N\mu}{k_B T}\right] \right) \tag{20}$$

where the average number of molecules in the system $\langle N \rangle$ is computed as:

$$\langle N \rangle = \frac{\sum_N \left(N\, Q_{NVT} \exp\left[\frac{N\mu}{k_B T}\right] \right)}{\sum_N \left(Q_{NVT} \exp\left[\frac{N\mu}{k_B T}\right] \right)} \tag{21}$$

Typically, GCMC simulation is used to compute adsorption properties. Cracknell et al. [92] employed GCMC in their study on the simulation of the adsorption of methane-ethane mixture onto a graphite surface. Both of the guest molecules were modeled as united atoms, implementing four different MC moves (Displacement, deletion, insertion, and particle exchange). One method to calculate the chemical potential in molecular simulation is by inserting a particle in the system and monitor the change in the internal energy, regularly determined by [93]. The mentioned approach is applicable in MD as well as MC. It is possible to calculate the excess chemical potential by the following equation in the canonical ensemble.

$$\mu_{excess} = -k_B T \ln \langle \exp \left[\frac{-\mathcal{U}(r^{test})}{k_B T} \right] \rangle \quad (22)$$

In this work, GCMC simulations of the bulk fluid phase were carried out to determine the correlation between the imposed chemical potential and the pressure. Thus chemical potential was not computed using insertion methods as in Equation 22.

The united atom representation, which is usually accomplished by lumping the hydrogen atoms into the atoms they are bonded to, can significantly reduce the computational effort required by minimizing the number of sites. However, one problem that is associated with united atom force field has to do with stereochemistry at the chiral centers. Also, it is a common practice to ignore the hydrogen atoms when placing the van der Waal's united atom center. The whole weight is given to the heavy non-hydrogen atom. To provide higher accuracy, the center should be shifted slightly to imitate the hydrogen atoms presence [94].

2.2.2.2. Isothermal-Isobaric ensemble

The MC simulation method was extended to the isothermal-isobaric ensemble in 1968 [95]. The ensemble's partition function is given by:

$$\Delta = \int \left(Q_{NVT} \exp \left[-\frac{PV}{k_B T} \right] \right) dV \quad (23)$$

The Gibbs free energy is calculated as:

$$G = -k_B T \ln \Delta \quad (24)$$

In the work of McDonald (1972), the move of volume change was introduced, and results from the presented algorithm were reported [67]. The importance of study is that excess thermodynamic properties of binary Lennard-Jones mixtures were tested and comparison with theories performed successfully.

2.2.2.3. Gibbs ensemble

The primary goal of the Gibbs ensemble MC simulation was to provide a handful tool to compute liquid-vapor and other fluid phase equilibria. The ensemble was created and developed by Panagiotopoulos [96], [97]. Two simulation boxes are used to initiate the simulation without an interface present. Respecting the nature of the phase equilibria, three distinct moves can be implemented in the simulations: Displacement of particles within a box (center of mass translation), particle transfer from box to another, and interchange boxes' volume. The list of different classical ensembles is shown in Table 3.

Table 3: Comparison of the classical ensemble types (non-reactive systems). (Adapted from [98])

Ensemble	Constraints	Fluctuating properties	Thermodynamic	
			System	Potential
Micro-Canonical	N, V, E	Quantum state Energy of each particle (ε_i)	Isolated	Min (S)
Canonical	N, V, T	Internal Energy (E_j)	Closed	Min (A)
Grand Canonical	μ, V, T	Number of particles N_i and Internal Energy (E_j)	Open	Min (-pV)
Isothermal-Isobaric	N, P, T	Volume (V_i) Internal Energy (E_j)	-	Min (G)

2.3. Adsorption

Adsorption isotherms can be classified into six types [99], as shown in Fig. 4. The process of identifying the adsorption isotherm form assists in understanding the mechanism

and the nature of the adsorption process. In addition, it indicates the type of pores that an adsorbent possesses. Type I isotherm is the most widely observed isotherm in microporous solids such as zeolites and activated carbon. The accessible micropore volume controls the maximum capacity of the material. Unrestricted monolayer-multilayer adsorption with nonporous or macroporous adsorbent gives Type II isotherm. Type III and Type V are uncommon; both are characteristic by the weak adsorbate-adsorbent interactions. However, Type III is obtained with nonporous carbons, while, some porous adsorbent exhibit Type V isotherm form. The main feature of Type IV is the capillary condensation in the mesoporous industrial adsorbent. The shape of isotherm of Type VI refers to stepwise multilayer adsorption, where physisorption is achieved layer by layer. The step height exemplifies the capacity for each adsorption layer [99], [100].

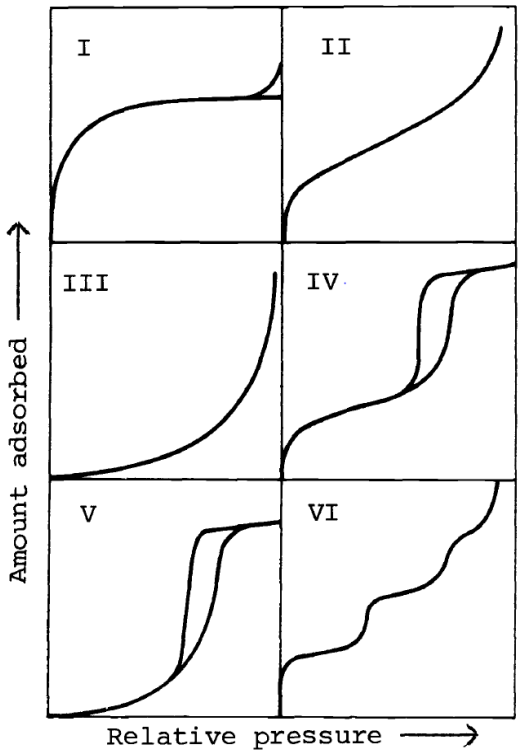

Figure 9: Types of physical adsorption isotherms. (Adapted from [99])

2.3.1. Langmuir isotherm

The most commonly used adsorption isotherm is the Langmuir isotherm type. The importance of this isotherm rises from its accuracy in predicting and correlating Type I and the initial section of Type II isotherms. The implicit assumptions of this isotherm are three. First, localized adsorption, which is adsorbed phase is held at the restricted site. Second, every available site can accommodate only one molecule or atom. Third, there is no interaction between adjacent adsorbed molecules and the energy of adsorption is constant. The Langmuir isotherm equation for a pure component is:

$$\theta = \frac{BP}{1 + BP} \; ; B = \frac{\alpha \exp\left(\frac{E}{RT}\right)}{\beta (2\pi m k_B T)^{\frac{1}{2}}} \tag{25}$$

$where\ \theta$ is the fractional coverage, B is the Langmuir constant (also called Henry's law constant), α is the sticking probability (accommodation coefficient for adsorption upon a collision on the surface), β is the rate constant for desorption, and E is the activation energy of desorption (value equals the heat of adsorption). Starting from the dynamic equilibrium between rates of adsorption and desorption, the above equation is derived. The isotherm approaches unity at high pressure and reduce to Henry's law form at low pressure. As temperature increases, B decreases dramatically since Q is positive or in other words, the adsorption phenomena is exothermic. Change in entropy is negative due to the reduction in degrees of freedom, and, change in Gibbs free energy must be negative (spontaneous process) in order to physical adsorption process to take place [8], [100].

The Langmuir isotherm equation can be derived from statistical thermodynamics by starting from the partition function for a single adsorbed molecule (Appendix D. 1), in the harmonic oscillator approximation, and including some assumptions. Mainly, the solid

material is unperturbed by the presence of gas molecules on its surface [101]. In other words, forces that hold the solid together are much stronger than the adsorption forces.

There are many models developed to predict equilibrium adsorption of gas mixtures. The main purpose is to reduce experimental effort in evaluating gas mixtures isotherms. Here, I will discuss two examples illustrating two categories out of the three.

1- Extended Langmuir equation

The extension from single gas adsorption isotherm to gas mixture one is determined by applying;

$$\theta_{Total} = \frac{\sum B_i P_i}{1 + \sum_{j=1}^{n} B_j P_j} \tag{26}$$

where index i corresponds to component in the gas mixture in study.

2- The adsorbed solution theory of Myers and Prausnitz [102].

Thermodynamic equations for the adsorbed phase (for liquids) treating the adsorbed mixture as a two-dimensional mixture:

$$dU = T\,dS - \pi\,dA + \sum \mu_i dn_i \tag{27}$$

$$dG = -S\,dT + A\,d\pi + \sum \mu_i dn_i \tag{28}$$

A is the surface area, and π is the spreading pressure (dimensions of energy per unit area). The spreading pressure is the difference between the surface tension of the clean and monolayer surface.

$$\pi = -\left(\frac{\partial U}{\partial A}\right)_{S,n_i} \tag{29}$$

From the Isothermal Gibbs adsorption isotherm, one calculates the spreading pressure by:

$$\pi = \frac{RT}{A}\int_0^P \frac{q}{P}dP \tag{30}$$

where q is the amount adsorbed in $mol_{adsorbate}$ per $mass_{adsorbent}$.

In this model, the spreading pressures are equal at equilibrium and activity coefficients are unity for all component in the adsorbed mixture. In case that an adsorption behavior follows Langmuir isotherm, the theory is identical to the extended Langmuir equation for gas mixtures.

2.3.2. Adsorbate – nanoporous adsorbent interactions

According to Yang[8], adsorptive separation can be accomplished by steric, kinetic, or equilibrium effect. Steric effects strictly exploit the molecular sieving properties of nanoporous media, whereas, kinetics separation is achieved by utilizing the difference in diffusivity [8]. Equilibrium separation target molecules' electronic properties; polarizability, magnetic susceptibility, permanent dipole moment and quadrupole moment [8]. When is required to target high polarizability and magnetic susceptibility, but no polarity, carbons with high surface areas would be considered as good candidates. High dipole moment molecules and high polarizability are targeted by any sorbent with high polar surface, for instance alumina, silica gel or zeolites. High quadrupole moment, then one requires high electric field gradient surface like zeolites because cations are dispersed above the negatively charged oxide.

The total potential energy between the adsorbent and adsorbate molecules consists of adsorbate-adsorbate and adsorbate-adsorbent interactions. Three different interactions contribution to adsorbate-adsorbent interactions. These are the dispersion, electrostatic and chemical bond [8].

$$\mathcal{U} = \mathcal{U}_D + \mathcal{U}_R + \mathcal{U}_{Ind} + \mathcal{U}_{F\mu} + \mathcal{U}_{\dot{F}Q} \tag{31}$$

where,

$\mathcal{U}_D$: Dispersion Energy (non specific)

$\mathcal{U}_R$: Close-range Repulsion (non specific)

$\mathcal{U}_{Ind}$: Induction energy (interaction between electric field and an induced dipole) (specific-charges)

$\mathcal{U}_{F\mu}$: Interaction between electric field F and a permanent dipole μ (specific-charges)

$\mathcal{U}_{\dot{F}Q}$: Interaction between field gradient and a quadrupole Q (specific-charges)

The nonelectronstaic interactions directly related to polarizability and dispersion energy include influence from magnetic susceptibility, which increases with the molecular weight as does the polarizability since more electrons are available for polarization [8].

For instance, N_2 molecule has a moderate quadrupole moment but does not possess permanent dipole, so $\mathcal{U}_{F\mu}$ term is zero. If the surface is without charges, electrostatic contributions are zero. Also, due to the mentioned potential, the adsorption of water is dominated by the strong dipole moment.

Certain electronic properties of surface atoms of an adsorbent must be taken into consideration when analyzing the adsorption process. The polarizability of elements increases as atomic weight increases in the same family, and decreases with increasing atomic weight for elements in the same row of the periodic table as the outer-shell orbitals are being increasingly filled. Hence, alkali and alkaline earth metal atoms have high polarizability. For electrostatic interactions, the charges (q) and the van der Waals radii of the surface atoms (or ions) are most important.

2.4. Nanoporous materials

According to the pore size, The International Union of Pure and Applied Chemistry (IUPAC) categorizes porous materials into three main groups [99]. Microporous (diameter less

than 2 nm), mesoporous (diameter between 2 and 50 nm), and macroporous materials (diameter larger than 50 nm). Microporous and mesoporous materials are conventionally called nanoporous materials [99]. Nanoporous materials can be classified as being organic, inorganic or inorganic-organic hybrid materials. Organic nanoporous materials include amorphous porous polymers and covalent organic framework. On the other hand, examples of inorganic materials are zeolites, mesoporous silica (silica) and carbon. The hybrid category contains the emerging MOFs and organic functionalized silica.

2.4.1. Zeolites

One of the most important materials are the inorganic zeolites. Zeolites are crystalline aluminosilicate solids with a regular well-defined pore size of molecular dimension and structure. They are aluminosilicate frameworks made from sharing SiO_4 and AlO_4 tetrahedral units. The Si:Al ratio controls the acidity and polarity of the zeolites. The pore size in zeolites is controlled by the number of oxygen atoms, altering the number of oxygen atoms in the framework affects size and shape of the pore [103]. Higher silica content increases the thermal stability of molecular sieves. In the presence of steam, properties of zeolites are affected [104]. Applications of zeolites in the chemical industry include catalytic cracking, hydrocracking, hydroisomerisation and iso/n-paraffins separation [104]. Because of the hydrophilic nature [105], zeolites are used as drying agent especially in natural gas moisture removal. Simulation studies of selective adsorption in zeolites have been successful [106]–[108]. Review on the utilization of molecular simulations in zeolites has been presented by Smit and Maesen [109]. The paper investigated the effect of cations and the mechanism under which the adsorption process takes place.

2.4.2. Metal Organic Frameworks (MOFs)

MOFs are a relatively new class of nanoporous materials. These materials are inorganic-organic hybrid materials. Several MOFs showed excellent gas separation performance by both kinetic and adsorptive processes, such as IRMOFs (Zn-O), ZIFs (Zn-N) and HKUST-1 (Cu-O). IRMOF-1 which is known as MOF-5 and one among MOFs undergoing exceptionally high H_2 storage capability [110]. HKUST-1 microporous structure and robustness [111] makes it eligible for many gas purification processes. Furthermore, MOFs have the unique combination of physiochemical and thermochemical characteristics, which mark them as candidates for a variety of novel applications. MOFs potential applications evolve around energy, environmental, and even biomedical uses [112]. Advancement in MOFs research targets improvement in CO_2 capture from different sources, and towards separation of hydrocarbon mixtures [113]. The viability of MOFs as desalination and water purification solution has not been explored in depth. Due to the tunability and capacity of MOFs, MOFs can act as a drug carrier, and storing and delivering medium of gasotransmitter gases [112].

There are some factors that essentially make MOFs more favorable than zeolites [114]. MOFs are easier to fabricate due to synthesis lower activation energy in comparison to the high pressure-temperature condition for zeolites synthesis. Zeolites require lengthy and energy consuming calcination and activation processes.

2.4.3. Zeolitic Imidazolate Frameworks (ZIFs)

ZIFs are a subclass of MOFs, most of them have identical topologies with zeolites [115]. Imidazolate Im units connect a transition metal M (usually, Zn or Co). The angle of M-Im-M is close to 145^o, commonly found in zeolites' Si-O-Si angle [11] (Figure 10). Greater cavities and consequently larger pore volumes are expected for ZIFs since M-Im-M bonds in

ZIFs are longer than that Si-O-Si in zeolites [47]. A gate-like pore aperture connects between internal cavities in ZIFs.

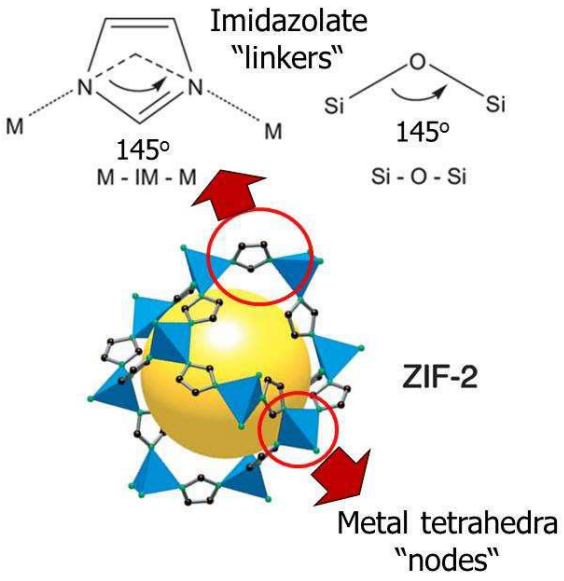

Figure 10: Comparison of the angle formed by O–Si–O and the angle formed by imidazolates bridging with transition metals in some ZIFs. (Adapted from [116])

The topology of ZIFs is controlled through ligand substitution, solvent, preparation time, metal source and some additives which have structure directing property [11], [117]. The capability of substituting functional groups at three distinct positions of the imidazole ligand (2, 4, and 5 positions) (Figure 11), allows for some control over the final topology of the structure. Substitution at 2 position led to SOD and ANA topologies; while substitution at 4 and 5 positions generated RHO topology (ZIF-25, -71, -93, -96, and -97) [118]. The other factor is the type of solvent utilized in the synthesis because of vacancy occupancy and the influence on ligand-ligand interactions [11]. An example of the solvent effect can be demonstrated by ZIF-7 and ZIF-11, which have the same composition but different zeolitic

topology. Moreover, it has been shown that final topology depends on the starting metal precursors.

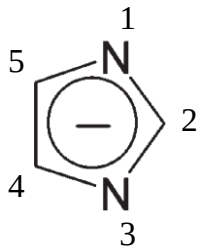

Figure 11: Imidazole ligand positions numbering

ZIF-8, which has sodalite (SOD) zeolite like topology (Figure 12(a)), has high surface area (1947 m^2/g) and experimental pore volume (0.663 cm^3/g) [11]. Figure 12(b) shows the structure of one cage that comprises the building block of ZIF-8. The yellow ball indicates the free volume (inner cavity) inside the largest cage. The pore aperture diameter is found to be 3.4 *Å* in the 6-ring (Figure 12(c)); whereas, the 4-rings' aperture size is negligible (too narrow for gas molecule to pass through it) [11].

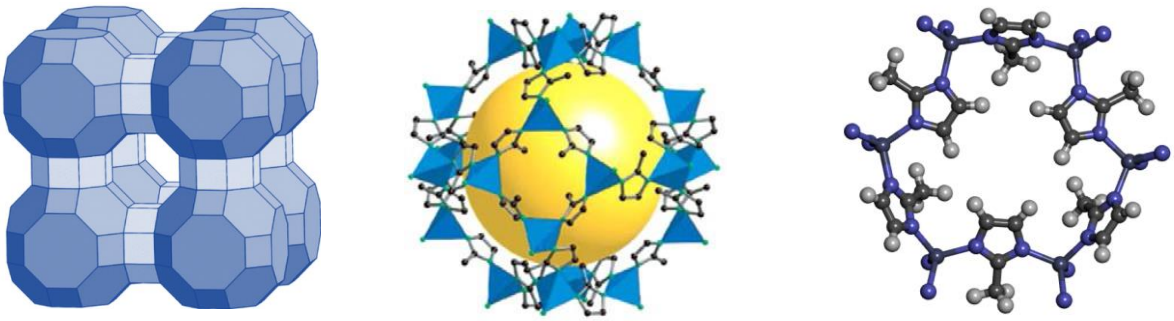

(a) (b) (c)

Figure 12: (a) ZIF-8 SOD crystal structure, (b) structure of one ZIF-8 cage (c) 6-ring ZIF-8 pore aperture

Both chemical and thermal stabilities are essential for materials to be utilized in gas separation applications. In general, ZIFs are the most stable structure series among MOFs. Thermal gravimetric analysis (TGA) was performed to assess ZIFs thermal stability. ZIF-8 and ZIF-11, for example, showed impressive thermal stability. In fact, the thermal stability of ZIFs, up to 550^{o} C in N_2, is superior over many MOFs structures [11], [116], and comparable to coordination polymers containing metal ions $M(pymo)_2$ [119] and metal silicate MOFs [120]. Lower thermal stability has been reported for other ZIFs structure (ZIF-68 to ZIF-70) of up to 390^{o}C [115].

The chemical stability of these structures has been examined by imposing extreme typical industrial processing conditions. This was accomplished by suspending samples of the structures in a variety of solvents for a duration of 1-7 days at three temperature (ambient, 50 degrees Celsius, and boiling point). The solvents were boiling water, methanol, benzene, and two concentrations of aqueous sodium hydroxide [11]. Samples of ZIF-8 and ZIF-11 were monitored by an optical microscope. It was clearly seen that ZIF samples maintained their crystallinity and porosity in organic solvents at boiling temperature. Only ZIF-8 was impervious to the boiling water and sodium hydroxide solutions at 100^{o}C for the whole studying period. On the other hand, ZIF-11 was shown to undergo some crystalline change after 3 days of immersion in boiling water [11]. The strong binding energy between IM and metal center (Zn (II) and Co (II)) and the hydrophobic nature of the ZIFs' pore and surface are the reason behind the observed excellent hydrolysis resistance. ZIF-8 is considered the most structural stable MOF against steam [121]. The water stability of a MOF will actually determine the possibility of utilizing such material in real applications [122].

One can exploit the hydrophobicity of ZIFs for efficient alcohol/water separation and bio-alcohol recovery [123], [124]. Among the studied ZIFs, are ZIF-8 and ZIF-71 [125]. ZIF-8 showed that it has no tendency to adsorb water in the gas phase reflecting the hydrophobicity of the structure and this has been explained by water vapor adsorption isotherm shape, heat of adsorption, and radial distribution function [126]. From radial distribution function for water adsorbed in ZIF-8 at saturation, it has been revealed that water structure is almost identical to that of pure water in bulk. However, ZIF-65 and ZIF-90 exhibited hydrophilic nature [126]. Park et al. claimed that the exposed edges and faces of the imidazolate units are responsible for ZIFs' exceptional high surface area and gas uptake performance [11].

Yaghi and coworkers studied the capacity of three ZIF-68 to 70 for CO_2 storage and CO_2/CO binary selectivity based on 50:50 volume ratio stream. These ZIFs structures have a similar zeolitic topology and have relatively large pore volumes [115]. Seemingly, CO_2/CO selectivity increases as the pore volume and surface area of the ZIF increase. They also reported that at 273K approximately 83 liters of CO_2 could be hold up to 1 liter of ZIF-69 [115] and 28 liter per liter of ZIF-100 at standard conditions [116], which are outstanding compared to the maximum loading observed in MOFs (MOF-177).

One of the highest CO_2 capacities between a ZIFs series (ZIF-68, 69, 70, 78, 79, 81, 82, 95, and 100) is the one reported for ZIF-78 (60.2 v/v). Moreover, ZIF-78 has been shown to have higher CO_2/CH_4, CO_2/N_2, and CO_2/O_2 selectivities among the considered ZIFs [127]. Many experimental and simulations studies have been reported that test specific MOFs for CO_2/(CH_4, N_2, CO or H_2) separation. Measured and simulated CO_2/CH_4 selectivity ranges from 2 to 12 from 50/50 compositions, and from 1 to 10 bar, mostly at 298K. On the other hand, CO_2/N_2 are typically higher and have a wider value range than CO_2/CH_4 selectivity. The

selectivity of the CO_2/N_2 mixture is higher in ZIF-78 (20–25) than ZIF-79 (15–20) under the same conditions, and this was attributed to the electronic structure and polarity of the imidazolate linkers [128].

The molecular sieving properties of ZIFs have also been studied in steric type gas separation because of the possibility of tuning the pore volume substantially with exchanging either the metal center or the organic linker. For instance, iso-butane and iso-butene, normal butane and iso-butane in ZIF-8 [129], propane and propylene in ZIF-8 and ZIF-67 [18], [50], and propane and propene in ZIF-8 [130]. The work by Zhang et al. illustrated how the thermodynamic diffusivity of molecules in ZIF-8 is influenced by the molecular diameter [129].

2.5. Ionic liquids (ILs)

2.5.1. Properties

Research work has been conducted to relate physiochemical properties of ILs to either the cation or the anion. Properties such as miscibility and thermal stability have been linked to the anion; whereas, the cation's shape, symmetry, and length of alkyl constitutes have great impact upon properties such as viscosity, density and surface tension [21]. As a result of them being designer solvents, viscosity, density and solubility of ILs vary over a wide range. It has been observed that ILs composed of large and asymmetrical ions possess low melting points [131]. Berthod et al. showed how the melting point is affected by considering multiple alkyl chain lengths and symmetry [131], [132].

Emphasis on IL viscosity is made because this property is one of the most vital ones in determining the pumping power requirement in separation processes, especially adsorption-based gas separation [133]. Among ILs, $[emim][C(CN)_3]$ has been reported to have one of the

lowest viscosities, at 7 cP at T = 323.15K [132]. ILs viscosities increase with alkyl chain length linearly [28]. Important factors that lead to higher viscosities are the presence of van der Waals interaction and hydrogen bonding [134]. The vapor pressure of IL changes by varying the alkyl chain length. Examining vapor pressure reported experimental data, vapor pressure do decrease as one increases the chain length of the cation.

Furthermore, some works split IL into two major categories; these are, protic and aprotic ILs. Protic ILs are those which prepared by proton transfer to a Bronsted base from a Bronster acid, and the importance of such classification is that the protic type is associated with lower melting point and higher fluidity [134], [135].

On the other hand, some commonly utilized ILs have been revealed to have a toxicity aspect. Soil contamination driven by degradation, sorption and desorption of ILs and toxicity to microorganisms marked the ILs as a potential risk to the environment [136]. Ramdin et al. [28] summarized the influence of anion, cation and functional groups on the toxicity. It has been stated that toxicity rises with alkyl chain length and carbon number on the cation. A trend of cation toxicity has been established, ammonium < pyridinium < imidazolium < triazolium < tetrazolium; however, one cannot consider this trend as universal due to many reported cases. Generally, ILs that involve halogens, chain branching, tertiary amine, nitro, nitroz, azo, and heterocyclic residues (imidazole) result in poor biodegradability; whereas, amides, hydroxyl, and linear alkyl chains improve the biodegradability of IL. Pyridinium and cholinium based ILs are more biodegradable than imidazolium and phosphonium ILs [28].

2.5.2. CO_2 affinity

Physical adsorption is considered the major mechanism of adsorbing CO_2 by ILs [25]. COSMO-RS (Conductor-like Screening Model for Real Solvents) [137] is a predictive model

that is used heavily to reduce the experimental efforts by screening a wide range of IL combination by theoretical calculations and to provide initial steps toward selection of IL for a particular application [138]–[141]. Some studies were directed to investigate the factors that dominate the CO_2 affinity of different ILs. The CO_2 solubility increases with pressure and decreases with temperature [142].

Maginn and coworkers concluded that the nature of the anion is responsible for CO_2 solubility by comparing between [BF_4], [PF_6], and [Tf_2N] anion based ILs. Also, they pointed out that C2 carbon in the imidazolium cation (2-position), see Figure 13, has a small contribution to CO_2 solubility [143]. From experimental measurements [143], atomic-scale simulations [28] and COSMO-RS calculations [138] show that ILs containing fluroalkyl groups have higher CO_2 solubility [142]. The common reason why [Tf_2N] has the highest solubility relative to [BF_4] and [PF_6] is that [Tf_2N] has two fluoroalkyl groups (CO_2-philic) [143], [144]. Subsequently, anions containing a higher number of fluoroalkyl groups possess higher CO_2 solubility, such as [methide][142].

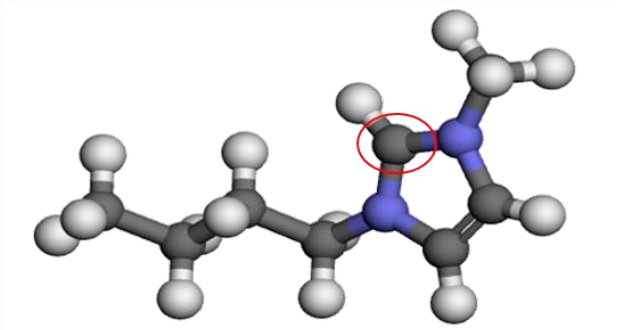

Figure 13: 1-butyl-3-methylimidazolium cation. The circle shows the location of C2

Zhang et al. study that covered 408 ILs combinations revealed that Tris(pentafluoroethyl)triflurophosphate [FEP] based ILs as strong candidates for carbon

capture [138]. The investigation continues with CO_2 presented to undergo higher solubility than n-alkanes, CO, H_2 and N_2 in imidazolium based ILs. Water and benzene have shown greater solubility in ILs than CO_2. The trend can be explained by exploiting molecules' electronic properties. Properties such as quadrupole moment (CO_2) or large dipole moment (water) lead molecules to hold higher solubilities. In other words, gas solubility in ILs is influenced profoundly by the anion nature, followed by gases electronic properties, and finally, to a lesser degree, cation group and substituents [145], [146].

Concerning the impact of changing cation in CO_2 solubility, cations with higher alkyl length experience marginal CO_2 solubility improvement [28], [142]; whereas, replacing the acidic hydrogen in the imidazolium cation with short alkyl substitute lowers the solubility [28]. Additionally, CO_2 solubility rises with molecular weight and free volume [147]. It should be mentioned that using ILs in capturing CO_2 processes suffer from the elevated ILs cost and high viscosities that translate into high operating cost.

2.5.3. CO_2 selectivity

The two most relevant mixtures in CO_2 gas purification cases are; CO_2/CH_4 and CO_2/N_2 for pre-combustion and post-combustion processes, respectively. CO_2 presence is reported to have a low impact on N_2 adsorption in ILs; therefore, real CO_2/N_2 selectivity is anticipated to be close to ideal selectivity [28]. However, ideal CO_2/CH_4 selectivity drops because of the CH_4 solubility with temperature trend versus that of CO_2. Table 4 shows a selected list of different possible ILs combination with their ideal selectivity towards CO_2. Additional selectivities can be extracted from solubility data by calculating Henry's law constant. The CO_2 selectivity in Table 4 are mostly generated from experimental values; however, selectivity found by COSMO-RS or optimized COSMO-RS or atomistic-scale simulations can be found in the

literature for an enormous number of ILs. In general, CO_2/CH_4 selectivity decreases with temperature and length of the alkyl chain in the IL's cation [148].

Table 4: Experimental ideal CO_2 selectivity of common ILs

IL		Temperature	Ideal Selectivity		Ref
Cation	Anion	K	CO_2/N_2	CO_2/CH_4	
emim	Tf_2N	313.15	24 ± 2	11.6 ± 0.3	[149], [150]
		298.15	35.9 ± 0.4	14.9 ± 0.1	[151]
		313.15	24.0 ± 0.5	11.20 ± 0.06	
		328.15	15.9 ± 0.3	8.57 ± 0.02	
		343.15	11.67 ± 0.06	6.79 ± 0.04	
		298.15	45.7	14.0	[139]
bmim		313.15	-	18.5	[147]
		333.15	32	7.6	[152]
		298.15	31	-	[153]
hmim		313.15	22.3 ± 0.8	8.7 ± 0.3	[149]
		298.15	44.4	10.1	[139]
		298.15	29.4 ± 0.4	10.3 ± 0.1	[151]
		313.15	19.3 ± 0.2	8.14 ± 0.07	
		328.15	13.6 ± 0.3	6.4 ± 0.1	
		343.15	10.3 ± 0.2	5.31 ± 0.08	
emim	TCM	288.15	92 ± 5	-	[154]
bmim		288.15	154 ± 10	-	[154]
mmim	$MeSO_4$	298.15	123 ± 10	35 ± 1	[155]
		313.15	33 ± 1	17.6 ± 0.4	
		328.15	16.4 ± 0.2	10.5 ± 0.2	
		343.15	10.8 ± 0.2	7.7 ± 0.1	
emim	$B(CN)_4$	298.15	53 ± 6	-	[156]
bmim		298.15	40 ± 2	-	[26]
emmim		298.15	46 ± 5	-	[26]
emim	dca	313.15	51 ± 8	21 ± 1	[149]
emim	CF_3SO_3	313.15	37 ± 3	16.9 ± 0.9	[149]
emim	BF_4	298.15	89 ± 5	36 ± 9	[155]
		313.15	38 ± 1	20 ± 2	
		328.15	21.5 ± 0.8	13 ± 1	
		343.15	14.4 ± 0.6	9.4 ± 0.7	
bmim		303.15	28.8	15.6	[157]
		313.15	26.4	14.9	

2.6. IL/MOF composites

As a result of the possibility to tune MOFs' micropores and structural properties, these systems have potential to be used as dynamic controller hosts for ILs [158]. Encapsulating IL in MOFs can reduce the amount of IL required and the viscosity [36]. Mainly due to the experimentally demanding and complicated method of synthesis, the vast majority of the literature work on MOFs supported ILs has been achieved by computational tools [25]. Jiang and coworkers had published two computational studies dealing with IL encapsulation in MOFs [32], [36]. Their first work examined the effect of incorporating IL [bmim][PF_6] in cavities of MOF (IRMOF-1)(IL/MOF) on CO_2/N_2 selectivity. They concluded that at a weight ratio of IL to MOF of 1.5, the selectivity was 3-4 times higher than that in pure IL. Next, they attempted to understand the influence of the IL's anion selection guided by quantum calculation information gathered from the COSMO-RS method. According to cited paper, small anions are located nearby the metal center; whereas, bulky anions are located in proximity to the phenyl ring. Another study was reported, in which ILs encapsulated in Cu-BTC MOF [37]. CO_2 adsorption was enhanced, but no significant effect on CH_4 or N_2 adsorptions were detected. Furthermore, the impact of encapsulating [bmim][SCN] on five different MOFs/COFs has been achieved by introducing the effect of IL dispersion in the studied MOFs. The MOFs included ZIF-8, IRMOF-1, and UiO-66 [6]. One of the most important outcomes of this work was that the separation performance is enhanced with better IL dispersion in the composite. Experimentally, Kinik et al. [48], and da Silva et al. [159] have explored the encapsulation of [bmim][PF_6] IL but in different MOF, ZIF-8, and Cu-BTC, respectively. The former demonstrated that the presence of IL (IL/ZIF-8) doubled the CO_2 selectivity, however, gas uptake was lower than pristine ZIF-8 [48].

3. SIMULATION METHODOLOGY

3.1. Computational reconstruction of ZIF-8 and IL@ZIF-8 unit cells

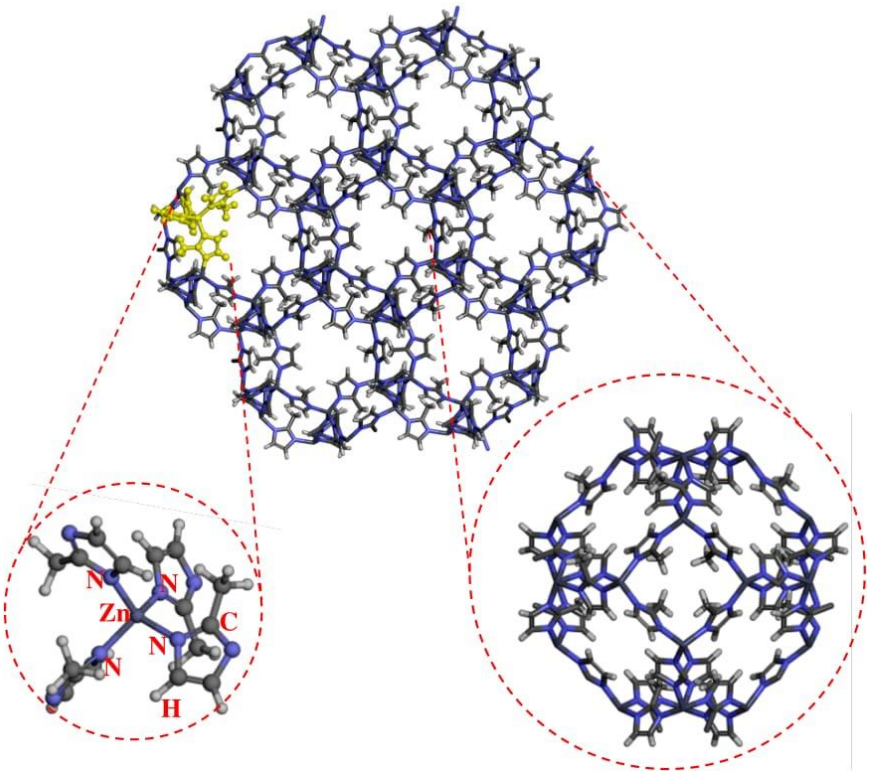

Figure 14: Atomistic representation of the ZIF-8 structure: the super-cell as used in our simulations (top), the basic building tetrahedral unit (bottom left) and one of the cages of the framework (bottom right).

ZIF-8 framework is a crystal with a builiding unit of a metal ion (Zn) tetrahedrally bridged with 2-methyl-imidazolate groups (mIM) that results in the tetrahedral building unit shown in Figure 14. ZIF-8 consists of cages connected with an aperture through which molecules have access to the cages. The unit cell of ZIF-8 was reconstructed in atomistic level from single crystal X-ray diffraction data reported by Parker et al. [11] (molar mass, *M*, of one ZIF-8 unit cell = 2,730.98 g mol^{-1}). A super-cell of eight (2×2×2) unit cells was used in all the simulations. The simulation in larger super-cells (3×3×3) displayed no additional accuracy or

finite-size effects. The framework in the simulation was rigid because it has been shown that the structure flexibility does not reveal a significant impact on the adsorption properties of small molecules at low pressure, such as Henry's law constant or the heat of adsorption, unlike molecules like iso-butene and *n*-heptane which demonstrate inflection behavior [160]. The IL consisted initially of the 1-butyl-3-methylimidazolium ([bmim$^+$]) cation and the bis(trifluoromethyl-sulfonyl) ([Tf_2N^-]) anion (molar mass M= 419.36 g mol^{-1}). The work has been extended to other ILs, tricyanomethanide [TCM^-], and tertracyanoborate [$B(CN)_4^-$], while keeping the same cation. The molecular representation of the ILs pair, as used in our simulations, is shown in Figure 15(a). The encapsulation of IL molecules in the ZIF-8 cages was carried out with a procedure described below, resulting in the confinement of ion-cation pairs in the framework cages. Figure 15(b) shows a representative encapsulation with [bmim$^+$][Tf_2N^-] as an example.

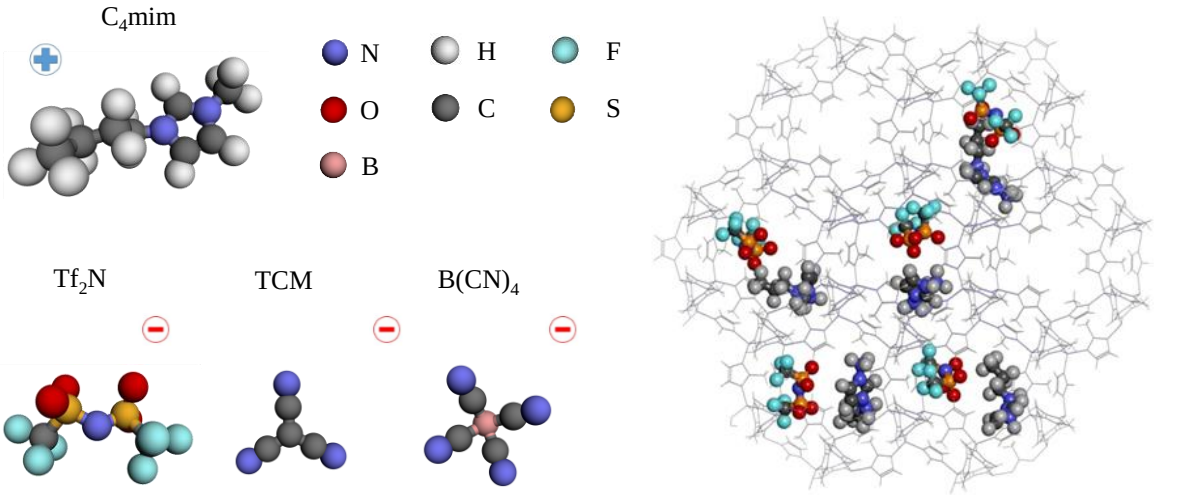

Figure 15: Atomistic depiction of (a) the ILs used, and (b) encapsulation of [bmim$^+$][Tf_2N^-] in ZIF-8 cages

3.2. Interaction parameters (force field) for the ZIF-8 framework, [bmim$^+$][Tf_2N^-] IL and the guest molecules (adsorbate)

Models for adsorbent and the adsorbate and force fields to model the energetic interaction between them are necessary to simulate adsorption in a nano-scale porous system. The force field for ZIF-8 framework consists of bond stretching (Equation 32), bond angle bending (Equation 33) and torsional angle distortion (Equation 34) terms for bonded intra-molecular interactions, and Lennard Jones (LJ) and electrostatic terms for non-bonded intra- and inter-molecular interactions (Equation 35), according to the expressions:

$$u(l) = \frac{k_l}{2}(l - l_o)^2 \tag{32}$$

$$u(\theta) = \frac{k_\theta}{2}(\theta - \theta_o)^2 \tag{33}$$

$$u(\varphi) = k_\varphi[1 + \cos(m\varphi - \varphi_o)^2] \tag{34}$$

where $k_l, k_\theta \; and \; k_\varphi$ are force constants, $l, \theta \; and \; \varphi$ are bond lengths, bond angles, and dihedral angles, respectively.

$$u(r_{ij}) = 4\varepsilon_{ij}\left[\left(\frac{\sigma_{ij}}{r_{ij}}\right)^{12} - \left(\frac{\sigma_{ij}}{r_{ij}}\right)^{6}\right] + \frac{1}{4\pi\epsilon_o}\frac{q_i q_j}{r_{ij}} \tag{35}$$

where q_i and q_j are the partial charges of atom i and j, respectively, ϵ_o is the vacuum permittivity and r_{ij} is the distance between the i and j atoms.

The force field used for the [bmim$^+$][Tf_2N^-] IL accounts for bond stretching and bond bending (Equation 32 and Equation 33), and non-bonded interactions given by (Equation 35). The dihedral angle distortion is expressed through the expression:

$$u(\varphi) = k_\varphi[1 + \cos(m\varphi - \varphi_o)] \tag{36}$$

Additionally, there are improper torsions whose interactions are expressed through:

$$u(\psi) = k_{\psi}(\psi - \psi_0)^2 \tag{37}$$

where ψ denote improper angle.

The transferable potential for phase equilibria (TraPPE) force field was used for the interaction of all guest molecules in this study [161]. In TraPPE, CO_2 is modeled as a linear rigid triatomic molecule with three charged LJ interaction sites located at each atom. N_2 is described by two LJ interaction sites. The three charges required to model N_2 quadrupole moment are distributed among the two atoms and a third massless pseudo-atom placed at the center of the N-N bond. The values for all the parameters of the TraPPE force field for the guest molecules in this work can be found in Appendix B. For the CH_4 molecule two different models were used: the first is the TraPPE united atom (TraPPE-UA) model [161], where CH_4 is depicted as a single, chargeless particle. In addition, CH_4 was modeled with OPLS-AA [162], which accounts for the hydrogen atoms explicitly and considers partial charges for C and H atoms.

Interactions between unlike atoms were calculated using the Lorentz-Berthelot combining rules:

$$\sigma_{ij} = \frac{\sigma_{ii} + \sigma_{jj}}{2} \tag{38}$$

$$\varepsilon_{ij} = \sqrt{\varepsilon_{ii}\varepsilon_{jj}} \tag{39}$$

The van der Waals interactions were computed with a 14 Å cutoff radius. Electrostatic interactions were evaluated by Ewald summation with a real space cutoff of 12 Å and accuracy of 1×10^{-5}; no tail corrections were used.

3.3. Methodology for the adsorption affinity calculations (Monte Carlo simulations)

In this work, Grand Canonical Monte Carlo (GCMC) simulations were employed for all adsorption calculations by utilizing the Cassandra Code (Version 1.2) [85], [86]. In GCMC simulations, one specifies the temperature (T), the volume (V) and the chemical potential (μ) of the species, and allowing the number of molecules (N) in the system to fluctuate. The average number of molecules adsorbed in ZIF is computed and reported in units of $moles_{absorbate}$ per $gram_{adsorbent}$, or $gram_{adsorbate}$ per $gram_{adsorbent}$. In order to achieve efficient sampling of guest molecules in the structure, one of five different trial moves at each MC step is being selected: translation of the center of mass of a gas molecule, rotation of the center of mass of a gas molecule, molecule insertion, molecule deletion and molecule regrowth. Molecular insertion, deletion and regrowth moves were attempted by employing the Configurational Bias Monte Carlo (CBMC) scheme. In CBMC, a molecule is divided into fragments prior to the simulation. These fragments are used to build new conformations if a regrowth or an insertion move is applied in a step, or gradually deconstruct the molecule if a deletion move is applied. Distinct positions, orientations, and the resulted molecular conformations are accepted using appropriate criteria based on Boltzmann type of weighting by taking into account internal degrees of freedom. Further information on the CBMC scheme is available in the manual accompanying the Cassandra code [88].

At thermodynamic equilibrium, the chemical potential of an adsorbate in the adsorbed and in the bulk phase should be equal. Thus, one can relate the chemical potential of an adsorbate in both phases. For the purpose of building the adsorption isotherms, it is important to correlate the input chemical potential to pressure. This can be attained by independent simulations for the bulk gas: a simulation box is built entirely from the gas of interest. The box

undergoes a GCMC simulation, which is post-processed by block averaging the pressure output.

For the simulation of gas adsorption in IL@ZIF-8, the initial structure of the encapsulated IL pairs in the framework cages was prepared using MC simulations in the canonical (NVT) ensemble in which the desired number of IL pairs was added in the ZIF-8 structure by CBMC. At this point, it is important to identify that different initial configurations of a given IL composition result in a different performance concerning gas selectivity. This is attributed to the variety of IL occupancy combinations in the available cages, which leads to multiple adsorption sites distribution. This is highlighted not only for the researcher interested in simulating such systems, but also can explain the experimental discrepancy in performance that can be ascribed to different realizations among the synthesized membranes of an IL@ZIF system. Consequently, for a given IL composition, multiple initial configurations of the IL in the ZIF-8 framework are produced. Each configuration is subjected to a GCMC simulation of gas adsorption and the final result is an average over the multiple simulations of the configurations of a given composition. Our efforts to ensure higher statistical accuracy are further realized by considering the IL as flexible and free to move during the course of the adsorption simulations. The motion of IL molecules is accounted by translation, rotation and regrowth within the ZIF-8 cage.

We prepared IL@ZIF-8 structures with varying IL compositions to quantify the effect of IL on the material separation efficiency. The IL incorporated into ZIF-8 (denoted as IL@ZIF-8) was obtained at a widespread range of IL to ZIF-8 composition (mol IL / mol ZIF-8), following the definition introduced by Ban et al. [29]. The composition spanned over the

capacity of the ZIF-8 to accommodate IL, ranging from 0.010 to 0.332, which corresponds to 0.02 to 0.38 IL weight fraction in the system.

In this work, four different types of simulations were performed: (1) GCMC simulations of the fluid phase to determine μ-P correlation; (2) GCMC simulations for the gas adsorption in pure ZIF-8; (3) canonical MC simulations of IL insertion into ZIF-8 cages, for the creation of the initial IL@ZIF-8 conformations; (4) GCMC simulations of gas adsorption in IL@ZIF-8. In the first three types of simulation, 1×10^6 MC equilibration steps were succeeded by 2×10^6 MC steps for every pressure point considered. To ensure better sampling, prolonged simulations were carried for the adsorption in IL@ZIF-8, so that $7 - 15\times10^6$ MC equilibration steps were utilized depending on the IL composition in the structure. The adsorbed amount determined by molecular simulation is the absolute thermodynamic adsorption. GCMC molecular simulations output is in absolute terms; the absolute total energy including gas-gas and gas-solid interaction, and absolute adsorption [163].

Regardless of the method utilized to measure the adsorption isotherm experimentally, the loading corresponds to excess adsorption [164]. Experimental measurements yield Gibbs surface excess adsorption and net adsorption [163], [165]. Experimentalists use two different approached to quantify adsorption, these are, volumetric and gravimetric methods. Volumetric method is considered as the standard procedure [163]; in gravimetric method, a spring balance is used to observe the weight of the solid material [166]. Pore volume is determined from helium adsorption experimentally by introducing the assumption of negligible adsorption of helium [163] at room temperature and low pressure [167].

Excess adsorption can be defined as the absolute amount of gas contained in the pores subtracted by the amount of gas that would be present in the pores in the absence of gas-solid

interaction [168]. The difference between these two values is close to zero at low sub-atmospheric pressure. On the other hand, at elevated pressures, the difference grows significantly. Evaluation of the excess amount of the adsorbed gases is required to compare the simulation results to experimental measurements. The following expression was used to transform absolute into excess adsorption:

$$N_{excess} = N_{absolute} - \rho_{Bulk} V_{pore} \quad (40)$$

The deviation between absolute and excess adsorption second virial coefficients is the pore volume of the adsorbent. Therefore, the importance of conversion to excess adsorption can be gauged by comparing pore volume to the virial coefficient. Absolute and excess adsorbed amount can be considered equal if the second virial coefficient is much higher than the pore volume [163], and the magnitude of difference growth with pore size. In great number of cases, this difference is large for the weakly adsorbed species [163]. Moreover, comparison between bulk density with pore density ($\frac{N_{absolute}}{V_{pore}}$) can be employed as a mean to judge the difference [165].

$$\rho_{pore} \gg \rho_{Bulk}$$

The difference between absolute adsorption from simulation and excess adsorption from experiment is negligible for adsorption of vapors near their boiling points [169] and the difference between them in terms of zero pressure limit of isosteric heats is finite [169].

The adsorption isotherm, which is the amount of gas adsorbed in the pores of the adsorbent over a pressure range at a fixed temperature, is the most prominent way of accessing an adsorbent's sorption efficiency towards specific gases. The isotherms reflect upon the adsorption affinity, which is crucial in evaluating gas selectivity [170].

4. RESULTS AND DISCUSSION

4.1. Testing Cassandra code

4.1.1. Density

Molecular simulations in the isobaric-isothermal (NpT) ensembles are used to determine density of bulk systems. The importance of such analysis is not only to check consistency and identify any problems in the code, but also to compare with experiments. Moreover, the density in the bulk phase is critical to convert absolute to excess adsorption (section 3.3). Through this study, the necessity of tail correction was emphasized. Also, the impact of increasing the total number of molecules in a NVT simulation on statistical error was demonstrated.

Simulations of methane (C1), propane (C3) and butane (C4) in the bulk phase at liquid state conditions (T= 300 K, P= 10-100 bar), and bulk methane (C1) at supercritical conditions (T=250, P= 200-300 bar) were carried out. An NVT equilibration run was used initially followed by NpT production run for property computation. Absolute standard errors ranged from 0.03 to 0.16%. Through this study, I investigated the influence of tail correction, simulation length and number of molecules. In these simulations, the TraPPE-UA force field was used. Calculations are compared to experimental data from the NIST database in Figure 16 and calculated density values are in Appendix E. Overall, the MC simulations reveal very good agreement with experimental results. The absence of tail correction in the TraPPE force field showed an underestimation in propane isothermal density plot. Figure 17 demonstrates how the number of molecules in simulation affect the error of the simulation in the standard deviation (SD). As it is well-known from theory and practice, the SD decreases linearly as a function of the inverse of square root of number of molecules.

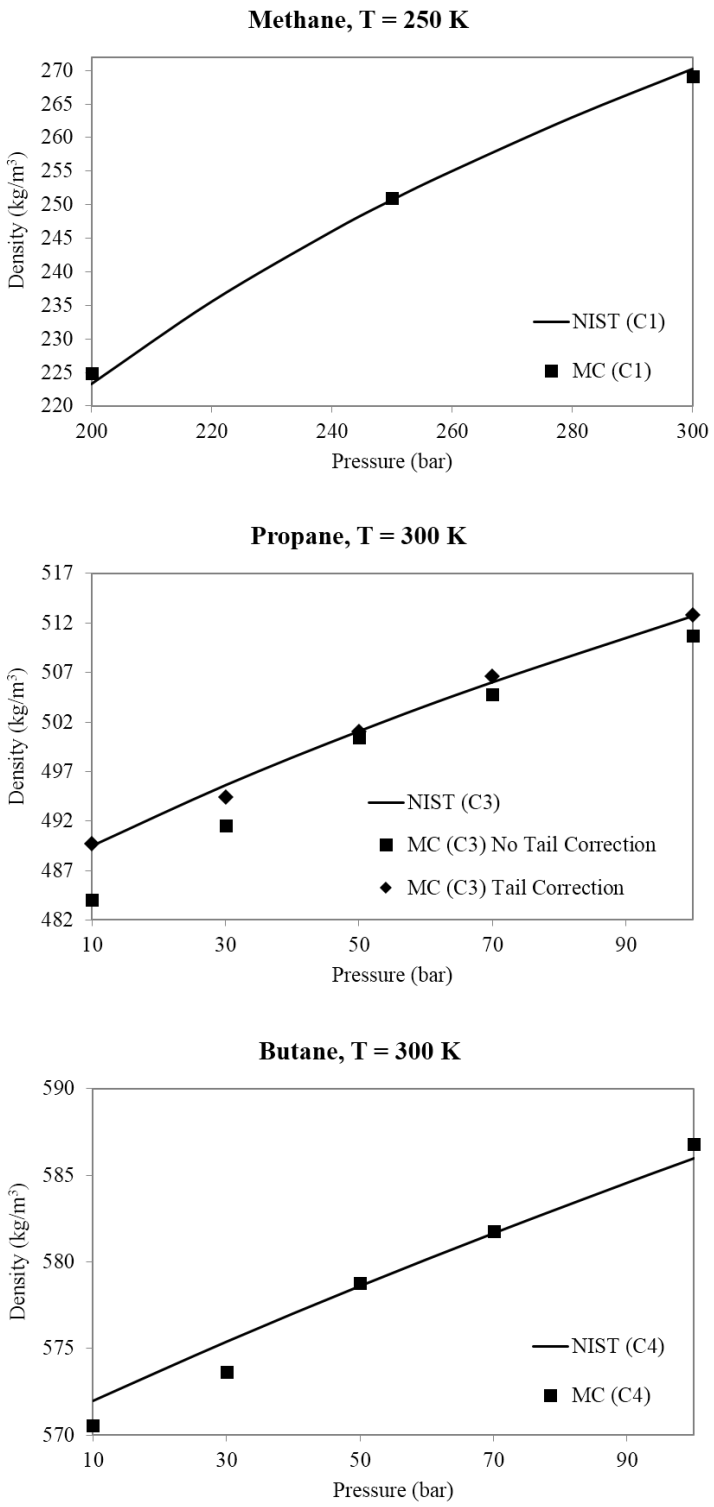

Figure 16: Density isotherms (C1, C3, and C4) from MC simulations, and experimental values (NIST database)[171]

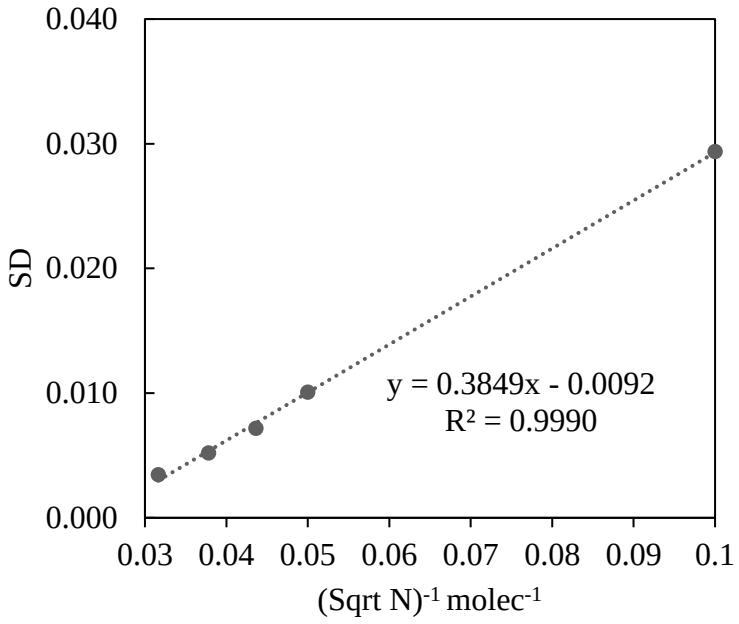

Figure 17: Standard deviation (SD) vs inverse of square root of number of molecules in simulation. SD calculated by considering block averaging of bulk C3

4.1.2. Vapor Liquid Equilibria (VLE) computations

In order to validate simulation methods that make use of CBMC and insertion and deletion of molecules schemes in Casandara code, I investigated the vapor-liquid equilibria of CH_4 using Gibbs ensemble and compared to experimental measurements. The outcome of this short study reflects upon the difficulty in capturing critical points by molecular simulations. Simulation of CH_4 in the Gibbs ensemble is compared with experimental VLE data points in Figure 18. The plot shows the agreement with experimental measurement away from the critical point, whereas, the deviation grows as one gets closer to the critical point of CH_4.

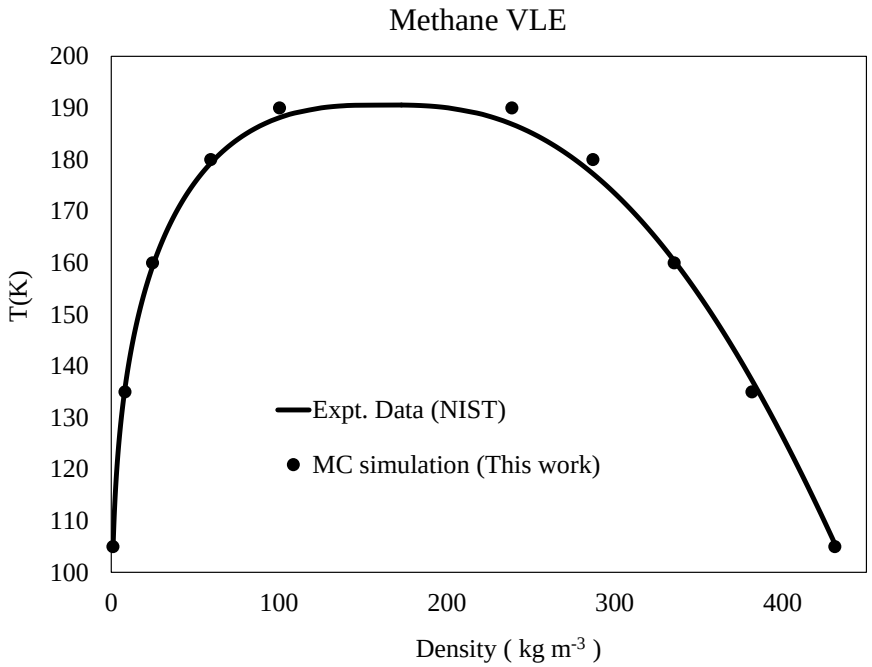

Figure 18: CH_4 vapor-liquid equilibrium curve

4.2. Adsorption in pristine ZIF-8

As a verification process of the accuracy of our ZIF-8 force field, the adsorption of guest species in ZIF-8 framework was calculated over a wide pressure range and compared against existing literature results. The adsorption isotherms of pure components are shown in Figure 19. It is worth highlighting the differences between the different experimental CO_2 adsorption isotherms. Calculations show satisfactory agreement with experimental data over the pressure range for the gases studied. It should be pointed out that modeling CH_4 with OPLS-AA yields a better agreement with the experimental values than TraPPE-UA force field. This indicates the importance of explicit hydrogen representation and electrostatic contribution to adsorbent – adsorbate interactions.

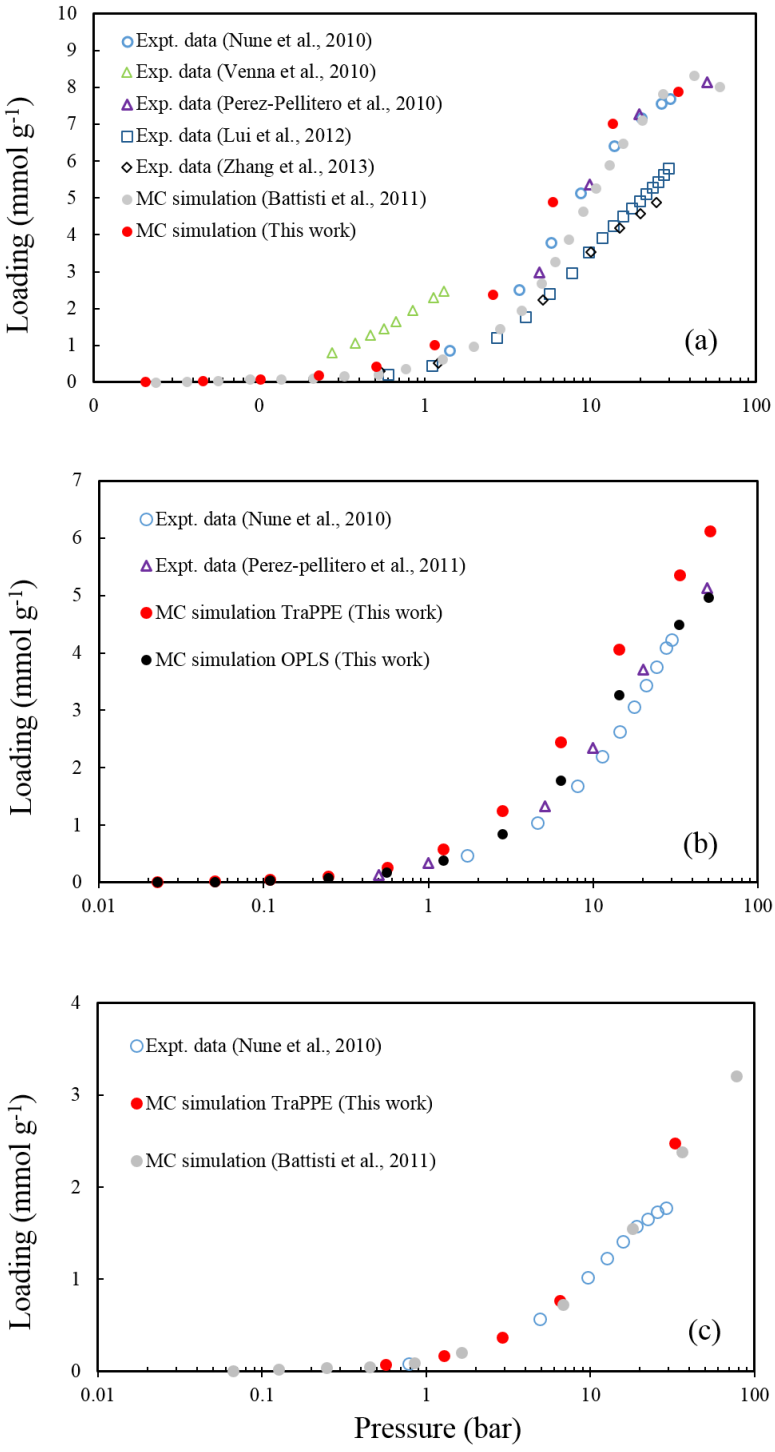

Figure 19: Adsorption isotherms. Comparison between literature data [47], [172]–[176] **and calculations in this work (red symbols), of (a) CO_2, (b) CH_4 and (c) N_2 in ZIF-8. The error bars are smaller than symbol size.**

4.2.1. Study on force field modification

In molecular simulations, ZIFs can be described by general purpose force fields, dedicated rigid force field, or dedicated flexible force fields [128]. Some studies described ZIFs by combining generic force field such as universal force field (UFF) with density functional theory (DFT) or by combining DREIDING and OPLS-AA force fields. Accounting for ZIFs structure flexibility might be very important when dealing with particular gases' diffusion.

It is a common observation that molecular simulations overestimate adsorption isotherms in the adsorption of gases in porous materials when applying force fields developed for pure gas in the bulk [45], [47], [176], [177]. For this reason, a common approach is to adjust LJ interaction parameters to fit experimental data, such as adsorption properties. There are additional reasons explaining the deviation between experimental and simulation adsorption results: simulations assume a perfect crystal structure neglecting imperfections or stacking faults, leftover solvents from synthesis, water adsorption, and partial pore collapse that can affect dramatically the adsorption performance of a material [164].

Perez-Pellitero and coworkers studied the adsorption of CO_2, CH_4, and N_2 on ZIF-8 [47]. They proposed a modified UFF to describe the interaction between the host-guest framework interactions of CH_4 adsorbed accurately. A scaling factor (ξ in Equation 41) was optimized to adsorption CH_4 isotherm. CH_4 was chosen because one can neglect electrostatic interactions safely [47]. The transferability of force field parameters were tested with CO_2 and N_2 sorption on ZIF-8. Employing the modified force field, results of adsorption of mentioned gases were improved, and additional adjustment was needed to totally fit the isotherm. The work reported by Battisit et al on adsorption of gases in multiple ZIFs structure were also

conducted using the same modification [174]. By following similar approach, other works introduced different scaling factor to better agreement with experimental measurement [45], [176], [177].

$$\left(\varepsilon_{ij}\sigma_{ij}^{6}\right)_{New} = \xi\left(\varepsilon_{ij}\sigma_{ij}^{6}\right)_{UFF} ;\ \xi: Scaling\ factor \tag{41}$$

Table 5: Summary of parameters adjustment in the Literature (adsorbate-ZIF-8), crossed LJ interactions calculated by applying Lorentz-Berthelot combining rules

Work by	ξ	ε	σ	Reference
Perez-Pellitero et al.	0.507	0.69 ε_{UFF}	0.95 σ_{UFF}	[47]
Battisti et al.	0.507	0.69 ε_{UFF}	0.95 σ_{UFF}	[174]
Liu et al.	0.899	-	-	[35]
Wu et al.	0.507	0.635 ε_{UFF}	1.0 σ_{UFF}	[34]

After many trial moves to optimize the TraPPE-UA force field, I present the in Figure 20 two most suitable parameters tweaking combinations. The force field intramolecular interaction for the structure and partial charges on all atoms remained the same.

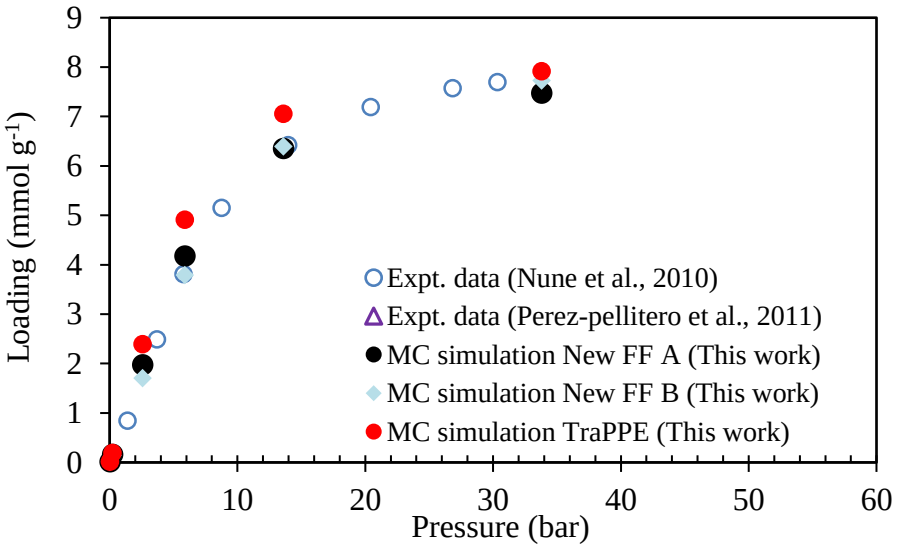

Figure 20: Adsorption Isotherm (298K) of CO_2 on ZIF-8. The error bars are smaller than symbols size. Parameters of Force Field A & B are listed in Table 6.

Table 6: LJ parameters of the selected Force Fields, crossed LJ interactions calculated by applying Lorentz-Berthelot combining rules

Force Field	ε	σ
A	0.95 ε_{TraPPE}	1.0 σ_{TraPPE}
B	0.95 ε_{TraPPE}	0.977 σ_{TraPPE}

It can be seen from Figure 20 that we achieve better representation of experimental data with using marginally adjusted parameters. Force field B was adopted because of the excellent agreement with targeted experimental measurement especially at low pressure where special attention was paid to obtain adsorption selectivity in the zero-pressure limit (Henry's regime). The adjusting factor resulted from this study reflects the reduction of the dispersion- repulsion interactions (van der Waals) cohesive energy of CO_2 in comparison to the TraPPE force field.

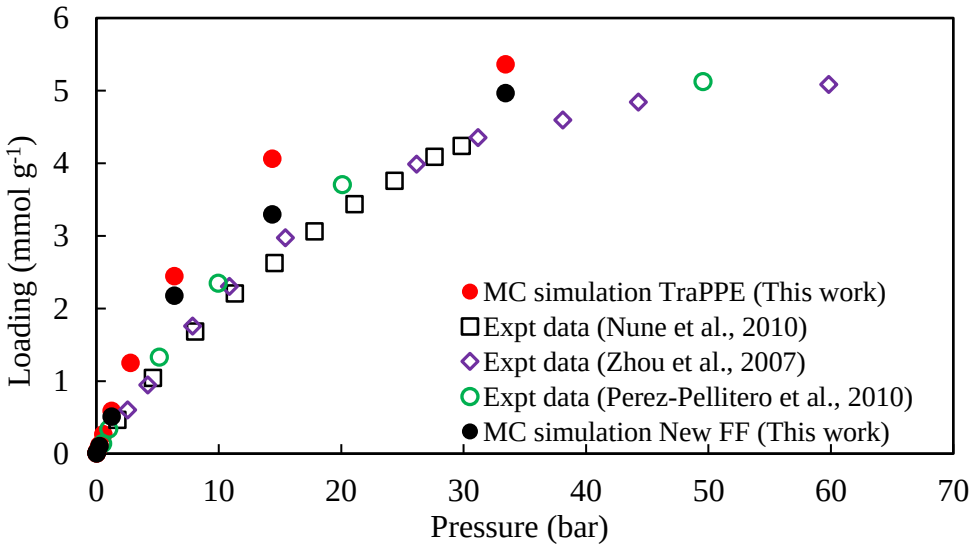

Figure 21: Adsorption Isotherm (298K) of CH_4 on ZIF-8

Utilizing the same modifications on LJ parameters from CO_2 on CH_4 adsorption, Figure 21 demonstrates the improvement achieved when transferring the chosen new force field (FF

B). However, one can clearly see that further parameter adjustment is needed to accurately correlate the experimental measurements. Similar behavior was reported from other modeling parts of several papers when they were fitting the LJ parameter on CH_4 isotherm. The mentioned method resulted in an enhancement in CO_2 isotherm but not to similar extent in CH_4 adsorption case, keeping into consideration that no further adjustments were implemented. The figure is not plotted in a semi-log plot to exploit the deviation between simulation and experimental points. It would be interesting to observe how new adjusted force fields perform at various temperatures. Unfortunately, this analysis has not been done because of the lack of consistency and availability of experimental results at temperatures other than 298 K.

In this work, we calculated the so-called Henry's law solubility constant used in atmospheric chemistry and other disciplines according to which for a component *i*:

$$K_{H,i} = \frac{c_i}{P_i} \tag{42}$$

where c_i and P_i are the concentration and partial pressure of component *i* [178], [179]. It can be clearly seen from Table 7 that the CO_2 Henry's constant with the new force field (2.66 bar^{-1}) is the same statistically with Nune et al. constant (2.64 bar^{-1}). This outcome illustrated the effectiveness of the force field alteration. The parameters adjustment procedure did not include pressure-adsorption point in Henry's regime, but still, the new force field captured more or less the whole in-study trend. CH_4 Henry's constant has decreased if one compared it with the previous (TraPPE) force field (11% decrease), but did not reach Nune's value because no further force field modifications has been used. In comparison to results from the work of Battisiti on ZIF-8, both of my modified force field and his (by Perez-Pellitero et al.) obtained an ideal CO_2/CH_4 selectivity of approximately 4.

Table 7: Henry's constants and selectivities from experimental and simulated adsorption isotherms for ZIF-8 at 298K

	T (K)	Henry's Constants (bar $^{-1}$)			Selectivity	
		CO_2	CH_4	N_2	CO_2/CH_4	CO_2/N_2
Expt. Data [172]	298	2.64	0.435	0.335	6.1	8.1
MC simulation with TraPPE	298	3.69	0.764	0.398	4.7	9.3
MC simulation with New FF	298	2.66	0.58	0.302	4.6	9.0

It is important to point out that the upcoming results and analysis in this work were obtained without further adjustment on the force fields. In other words, generalized adsorbate force fields were used through this work for two particular reasons. First, selectivities outcome determined by employing modified and unmodified force fields resulted in similar values statistically as listed in Table 7. The second reason is the intention to have a predictive study by using force fields developed independently for each molecule or structure.

4.2.2. Additional calculations

One can estimate the low-high pressure limit based on the analysis of the importance of electrostatic interactions. At elevated pressure range, fluid-fluid interactions are more important than at low pressure. Therefore, absence or presence of electrostatic interactions should reflect upon the determination of low and high-pressure sides. Figure 22 shows the deviation percentage observed on the amount of CO_2 adsorbed for various ZIFs structures. The deviation percentages were calculated relative to the adsorbed amount of CO_2 considering full

interactions between the host framework and CO_2. The plot shows high deviation at low pressure reflecting the importance of considering effects of electrostatic interaction [4].

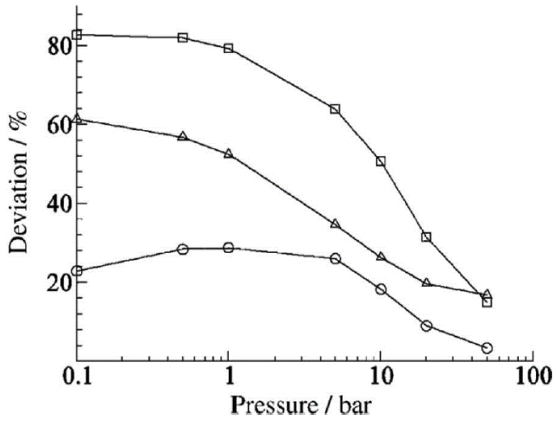

Figure 22: Deviation Percentage of adsorbed CO_2 amount for ZIF-8 (circles), ZIF-69 (triangles), ZIF-76 (squares) without taking into account electrostatic interaction. (Adapted from [4])

Also, I have attempted to study such influences not only with electrostatic interactions but also with tail correction, and the later shows the opposite trend of electrostatic interactions. Projecting the indication of Figure 22, I have defined the low and high pressure regimes of CO_2-ZIF8 as follows:

Low Pressure	P < 10 bars
High pressure	P > 10 bars

4.3. Ideal Adsorption Selectivity

Several factors influence the design of gas separation processes. Selectivity alongside material adsorption capacity gives a proper indication on the mixture separation efficiency. The most substantial factor is the material performance on the adsorption selectivity for the desired gas relative to an undesired gas [7]. In order to evaluate adsorbent selectivity, several

methods were proposed in the literature. Table 8 summarizes the parameter defined by each method to serve as an evaluation factor of the separation efficiency.

The adsorption-based separation efficiency is assessed by the so-called equilibrium selectivity. This is defined as the ratio of the adsorption isotherms slopes of the two components at low pressures (Henry's law regime), where the loading is governed by guest-host interactions (guest-guest are negligible), and has a linear dependency on the pressure [8]. Therefore, to achieve valuable comparison between the capacity and selectivity of a structure towards an adsorbate, the ideal selectivity was estimated by the ratio of Henry's law constants [32]. These constants can be determined given a solid configuration and models for adsorbate-adsorbent interactions. Consequently, the ideal selectivity of component *i* over component *j* in the Henry's law regimes is defined as:

$$S_{i/j}^{H} = \frac{K_{H,i}}{K_{H,j}} \tag{43}$$

In order to quantify the ideal selectivity, adsorption isotherms were determined at low pressure and results are shown in Figure 23. Regarding the adsorption in pure ZIF-8, there is a slight underestimation of CO_2 adsorbed amount relative to Ban et al. experiments [29].

Table 8: Various sorbent selection parameters proposed in the literature

Proposed by	Key parameter(s)	Factor(s)	Notes on the Parameters	Ref.
Knaebel (1995)	$S = \frac{K_i}{K_j}$	• K_i and K_j (Henry's law coefficient for component i and j)	• Adsorption isotherms follow Langmuir behavior • The components on the adsorbed phase surface are the more strongly adsorbed species • Constant at a given T	[10]
Gaffney et al. (1993)	$\alpha(i/j) = \frac{N_i}{Yi}\frac{Y_j}{N_j}$ $IBWS = \frac{D1}{D2}$	• N_i (Amount coadsorbed at component i partial pressure in the feed); Y_i (Mole fraction of component i in the feed) • Isothermal Binary Working Selectivity (IBWS) (Binary mixture capacities) • D_i working capacity of component i using IAST	• Higher IBWS gives higher recovery and therefore lower power requirements	[180]
Notaro et al. (1998)	$AFM = \Delta N_2 \frac{\alpha_{ads}^2}{\alpha_{des}}$	• Adsorption Figure of Merit (AFM) • ΔN_2 (Difference between N_2 adsorbed amount at high and low pressures) • $\alpha_{ads}$and α_{des} (adsorption selectivity at adsorption and desorption conditions)	• Empirical rule of thumb • No theoretical development was made to reach the separation parameter AFM	[183]

Table 8 Continued

Proposed by	Key parameter(s)	Factor(s)	Notes on the Parameters	Ref.
Ackley (1998) **Ackley et al. (2000)**	$\alpha = \frac{\Delta X_i}{\Delta X_j} = \frac{L_i(y_i, P_H, T_1)_{ads} - L_i(y_i, P_L, T_2)_{des}}{L_j(y_i, P_H, T_1)_{ads} - L_j(y_i, P_L, T_2)_{des}}$	• α (Adiabatic separation factor) • ΔX (Working capacity) • L_i (Loading or amount of adsorbate) • y_i (composition: mole fraction) • T_1, T_2 (Temperature at adsorption and desorption) • P_H , P_L (Pressure at adsorption and desorption)	• Ratio of working capacities under (nonisothermal and multicomponent conditions) • Analysis assumes equilibrium throughout adsorbent bed at the end of the adsorption and desorption steps	[181], [182]
Rege and Yang (2001)	$S = W\alpha_{1,2}$	• Working capacity: $(W) = \frac{\Delta q_1}{\Delta q_2}$ • Equilibrium selectivity: $(\alpha_{1,2}) = \frac{q_{m1} b_1}{q_{m2} b_2}$	• Adsorption isotherms follow Langmuir behavior • The components on the adsorbed phase surface are the more strongly adsorbed species	[184]

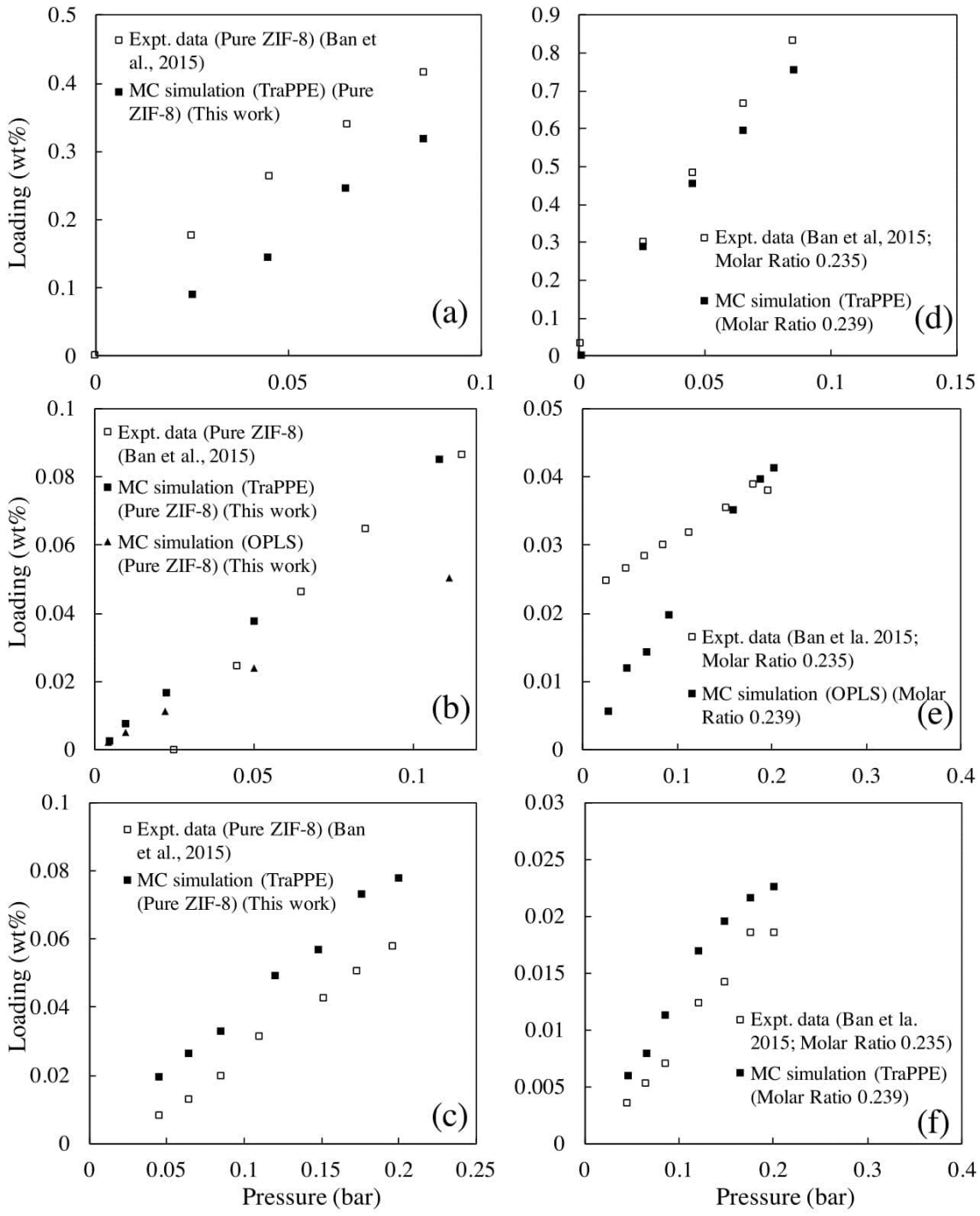

Figure 23: Adsorption Isotherms in Henry's law regime of CO_2, CH_4 and N_2 in ZIF-8 at 298 K ((a), (b) and (c) respectively) and in IL@ZIF-8 ((d), (e) and (f), respectively) at different molar ratios.

Computations were carried out in the new, modified system, IL@ZIF-8, with an IL composition matching that of the experimental data, which correspond to a molar ratio of 0.239. Henry's law constants and ideal binary selectivity for pristine and modified ZIF-8 are listed in Table 9.

Table 9. Henry's law solubility constant and ideal adsorption selectivity from experimental and simulated adsorption isotherms for various gases in ZIF-8 and IL/ZIF-8 at 298K

Source	System	IL/ZIF-8 (Molar Ratio)	Henry's Law Solubility Constant (bar^{-1})			Ideal Adsorption Selectivity	
			CO_2	CH_4	N_2	CO_2/CH_4	CO_2/N_2
Expt. data [29]	ZIF-8	0.0	5.2±0.7	0.70±0.05	0.28±0.02	7.50±0.08	19±3
	IL@ZIF-8	0.235	10.2±0.8	0.25±0.08	0.10±0.02	41±10	100±20
This work	ZIF-8	0.0	3.7±0.1	0.49±0.02	0.40±0.01	7.4±0.4	9.3±0.3
	IL@ZIF-8	0.239	9.3±0.9	0.22±0.01	0.134±0.007	42±4	69±7

The incorporation of IL in ZIF-8 cages reduces CH_4 and N_2 adsorption, which can be attributed to the reduced space available for the gas molecules. The Henry's law constants for CH_4 and N_2 at 0.239 molar ratio are 2.3 times and 3.0 times, respectively, lower than that in pristine ZIF-8. In contrast, the experimental Henry's law constant for CH_4 and N_2 at 0.235 molar ratio, is 2.8 times and 2.7 times lower than that in pristine ZIF-8, respectively. Simultaneously, CO_2 adsorption is enhanced due to its strong Coulombic interactions with the $[bmim^+][Tf_2N^-]$ pairs. These interactions provide additional adsorption centers and overcompensate the decline in the available free pore volume in the modified ZIF framework.

The guest molecules collective response to the presence of IL translates into highly improved CO_2/N_2 and CO_2/CH_2 ideal adsorption selectivity values in the new modified ZIF system, as both our simulations and literature experimental data show.

4.4. Impact of IL/ZIF-8 molar ratio on ideal adsorption selectivity

To effectively screen the material for its carbon capture capability, it is important to evaluate how CO_2 selectivity varies with IL composition in this IL@ZIF composite system. Therefore, structures of IL@ZIF-8 with varying IL composition were prepared and tested using identical methodology discussed in previous sections.

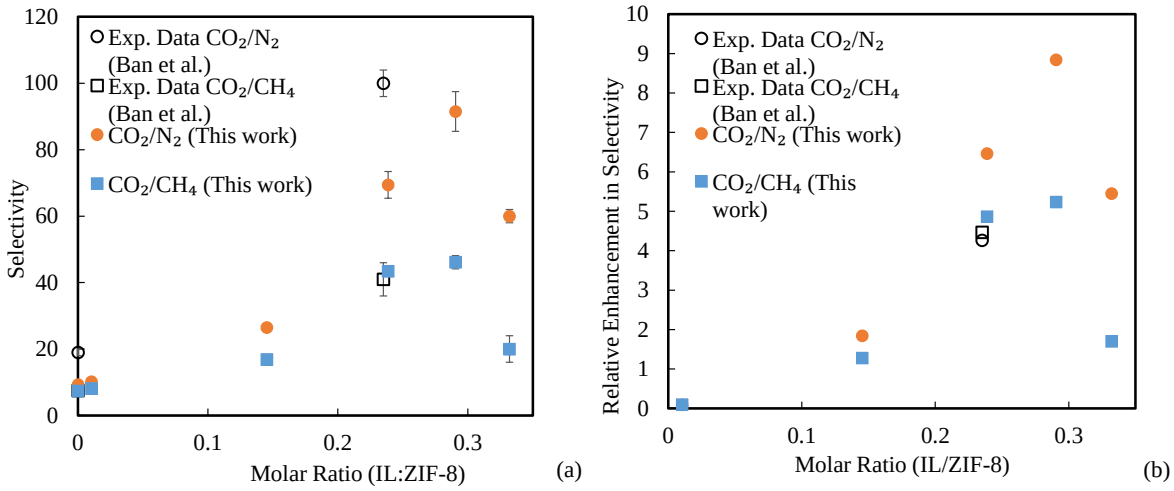

Figure 24: (a) CO_2/CH_4 and CO_2/N_2 adsorption selectivities and (b) the relative enhancement in selectivities, as a function of IL composition in ZIF-8.

Figure 24(a) shows CO_2/CH_4 and CO_2/N_2 selectivities as a function of IL composition in ZIF-8. We explored the compositions starting from the pure ZIF-8 and up to the maximum capacity of IL in ZIF-8 cages. It is critical to point out that CO_2/CH_4 selectivities reported in Figure 24 are determined by modeling CH_4 using OPLS-AA. The TraPPE-UA force field failed to capture the influence of the IL presence, as it overestimated CH_4 adsorption compared to the experiments, and was not used for these calculations. The selectivity rises exponentially

with rising IL composition at relatively low compositions. This is justified by the creation of other favorable sites for CO_2 adsorption, as the number of the encapsulated IL pairs increases. The less polar N_2 (quadrupole moments: N_2= -4.65×10^{40} C m^2 ; CO_2= -14.27×10^{40} C m^2) [185] and the non-polar CH_4 develop weaker interactions with the IL sites, therefore are mainly affected by the reduced free volume in the pores due to IL occupation; hence, their sorption is reduced. The non-specific quadrupole moment contribution to the adsorbent-adsorbate interaction can be expressed following this equation [8]:

$$\mathcal{U}_{\dot{F}Q} = 0.5\, Q\, \dot{F} = -\frac{Q\, q\, (\, 3\cos^2\theta - 1)}{4\, r^3 (\, 4\pi\, \epsilon_0)} \qquad (44)$$

θ: angle between field gradient and the axis of the linear quadrupole, Q: linear quadrupole moment. The maximum potentials in gradient-quadrupole is found when the quadrupole is arranged linearly with the charge on the surface.

From the overall trends of CO_2, CH_4 and N_2 sorption capacities in the composites, we observe a maximum adsorption CO_2 capacity of the material. This results in a maximum value in the CO_2 selectivity. There is a critical number of IL pairs above which CO_2 sorption decreases: at very high IL occupancies where some cages accommodate more than one IL pair, the tight conformation between the anion [Tf_2N^-] and the cation [$bmim^+$], decreases the available favorable CO_2 adsorption sites; this argument will be further investigated in the future. Nevertheless, this probable mechanism is reflected at the highest composition tested with a molar ratio of 0.332, at which the calculated CO_2 capacity is even lower than that in the pure ZIF-8 framework.

At 0.291 molar ratio, the simulated selectivity of CO_2/N_2 and CO_2/CH_4, reached approximately 92 and 46, respectively. These values are higher than the reported selectivities

achieved in bulk IL ([bmim$^+$][Tf_2N^-]) equal to 32 and 7.6 [186], respectively, or the selectivities reported in the pure ZIFs structures.

The relative enhancement representation was evaluated to facilitate understanding of the impact of IL presence on selectivity. Enhancement of selectivity is calculated by normalizing the selectivities in IL@ZIF-8 structures to the selectivities in pure ZIF-8. Figure 24(b) summarizes this study by plotting relative enhancement versus IL molar ratio in ZIF-8, where Relative Enhancement (RE) is defined at different IL compositions (α) in (Equation 45).

$$(\text{Relative Enhancement of A/B Selectivity})_{\alpha} = \frac{S_{A/B|\alpha@ZIF8} - S_{A/B|Pure\ ZIF-8}}{S_{A/B|Pure\ ZIF-8}} \qquad (45)$$

The sole composition point from Ban et al. was constructed and the estimated relative enhancement is included along with our results. The experimental value for the enhancement in CO_2 selectivity indicates a similar influence by IL on CO_2/N_2 and CO_2/CH_4 selectivities. On the simulation side, CO_2/CH_4 selectivity and selectivity enhancement agrees well with the reported experimental point. Moreover, it is worth pointing out that the gap between simulation data for CO_2/N_2 and CO_2/CH_4 in terms of both selectivity and enhancement grows as IL composition rises. In particular, CH_4/N_2 selectivity increases linearly as a function of IL composition. The overall comparison shows that the IL presence is modeled with a satisfactory accuracy relative to the experimental work.

4.5. [bmim$^+$][TCM$^-$] and [bmim$^+$][B(CN)$_4^-$] ILs

4.5.1. [bmim$^+$][TCM$^-$] IL

It was reported by Labropoulos et al. [154] that 1-alkyl-3-methylimidazolium tricyanomethanide [$C_n$mim][TCM] IL family has ideal CO_2/N_2 selectivities that are

competitive to selectivities recorded by most ILs. Labropoulos investigated two alkyl chains (ethyl and butyl) of the imidazolium cation. In that work, the selectivity of CO_2/N_2 reached 154 and 92 for [bmim] and [emim], respectively, with [TCM] anion at 308.15K. An Arrhenius relationship of Henry's constant was achieved by presenting values of Henry's constants at three temperature (288.15K, 308.15K, and 323.15K), which indicate enormous improvement in CO_2 solubility by a decrease of few degrees. By focusing on Henry's constants determined in the work of Hou et al. [187], Ramadin et al. [152] and Labropoulos et al. [154], both $[bmim^+][Tf_2N^-]$ and $[bmim^+][TCM^-]$ ILs share similarities in terms their affinity towards CO_2 (Also look at figure 2.(a) from Labropoulos et al. [154]). Therefore, examining [bmim][TCM] incorporation into ZIF-8 can show the influence of incorporating less bulky anion (effective radius $[\mathrm{TCM}] = 2.84$ Å ($\approx 96 Å^3$) [188]) in the structure.

Vergadou et al. [189] optimized a force field to represent [TCM] IL family. In the optimization process, 1-butyl-3-methylimidazolium tricyanomethanide was selected as a benchmark system at 298.15K and 1 bar to accurately predict thermophysical and transport properties by altering LJ parameters and tuning charge distribution concurrently. The force field developed has been verified by comparing computed various thermophysical and transport properties to experimental measurements over a broad range of temperatures. Properties such density, viscosity, and self-diffusivity were thoroughly studied. Densities found employing the developed force field resulted in a maximum deviation of 1.2% relative to the experimental values and results illustrated the force field capability to capture temperature dependence of density. The experimental NMR measurements for the cation diffusivity were also plotted against those determined from MD simulations. In addition to the

mentioned properties, structural properties (relying on radial distribution function), and dynamic behavior of the IL have been examined, and some trends explained [189].

An all-atom representation was used in the force field to describe potential energy of the molecular systems. The force field is segmented into two major parts; bonded and no-bonded. Vergadou et al. also argued that calculating partial charges on the IL atoms is better achieved instead of computing the charges from isolated ions, imposing +1e or -1e to cation or anion, respectively. Rescaling the total ionic charge to $\pm 0.75e$ was defined as the optimum set of parameters to realistically describe the IL because of the charge transfer nature between cation and anion reduce the total charge and polarizability effects. The set of partial charges was adopted as it achieved the higher degree of transferability in addition to theexcellent agreement with available experimental data [189]. Counting on the pure IL ideal CO_2 selectivity and previous analysis on [bmim][Tf_2N]@ZIF-8 composite analysis, one should expect improved capacity and selectivity with [$C_n$mim][TCM]@ZIF-8 structures. To obtain a good understanding of the influence of the anion in the structure, [bmim][TCM]@ZIF-8s were prepared, covering the whole range of possible compositions of IL into ZIF-8. The selectivity/capacity analysis should be extended to examine the effect of alkyl chain length on material's performance on carbon capturing abilities.

Inserting IL was again accomplished by CBMC scheme established in Cassandra MC code. For the results in this thesis, five different and unique initial configuration were used a mean to evaluate a particular IL composition. The molar volume of [bmim][TCM] (217.4 cm^3 mol^{-1}) [189] is lower than the reported molar volume of [bmim][Tf_2N] (285.7 cm^3 mol^{-1}) [49] at 298.15K. Consequently, the number of IL pairs that can be inserted into a ZIF-8 cage increased by 1.

4.5.2. [bmim$^+$][B(CN)$_4^-$] IL

ILs that contain the tertracyanoborate [B(CN)$_4^-$] anion showed potential towards carbon capture (40 ± 2 and 53 ± 6 CO_2/N_2 selectivity for [bmim] [B(CN)$_4^-$] and [emim] [B(CN)$_4^-$], respectively) [26], [156]. The non-electrostatic force field terms are from (Koller et al. 2012) [190] united atom models according to the method proposed by Lui et al. [191]. It has to be noted that the [bmim] force field parameters are transferred from [emim][B(CN)$_4$] as well, except σ_{LJ} of (NC) atom (introducing n_{CT2} parameter)[192], where n_{CT2} characterize the alkyl chain length. On the other hand, the electrostatic force field terms parameterization is taken from (Koller et al.) [192], [193].

However, some concerns may arise when following the previous papers. First, here, we use the united atom for both branches in the imidazolium cation, unlike former studies in this thesis. Explicit representation of atoms has shown importance in CH_4 adsorption. Lui et al. showed that the united atom approach reduces computational effort and performs in a similar fashion as the all atom model concerning properties of pure ionic and mixtures. One can still utilize Lui et al. (2006) all atom representation provided in the same paper to keep consistency between the studies. In overall, results determined from UA model can be used to study the encapsulation qualitatively. The second concern, improper angles in UA model utilized in this work are in introduced in CHARMM form, which is not supported in the code's improper angles options. A way to tackle this issue is by introducing improper torsional angles as dihedral angles in Cassandra molecular connectivity files. Another way is to define this form in Cassandra code under the improper torsional angle, but the former method worked successfully.

As it has been demonstrated in previous sections, the insertion of [bmim][$B(CN)_4$] was also accomplished by the CBMC scheme. Unsurprisingly, following the molar volume order between ILs, the number of [bmim][$B(CN)_4$] pairs that can be enclosed in ZIF-8 cage lied between that of [bmim][TF_2N] and [bmim][TCM]. A molar volume of 245.05 cm^3 mol^{-1} is determined for [bmim] [$B(CN)_4^-$], a molar volume that lies between molar volumes of [bmim][TCM] and [bmim] [Tf_2N].

4.5.3. CO_2 selectivity

Similar to the preceding work, four different types of simulations were performed: (1) GCMC simulations of the fluid phase to determine μ-P correlation; (2) GCMC simulations for the gas adsorption in pure ZIF-8; (3) canonical MC simulations of IL insertion into ZIF-8 cages, for the creation of the initial IL@ZIF-8 conformations; (4) GCMC simulations of gas adsorption in IL@ZIF-8. In the first three types of simulation, 2×10^6 MC equilibration steps were succeeded by 2×10^6 MC steps for every pressure point considered. To ensure better sampling, prolonged simulations were carried out for the adsorption in IL@ZIF-8, so that 3×10^7 MC equilibration steps were utilized depending on the IL's type and composition in the structure. The selectivties were computed in a similar fashion as earlier calculations utilizing Henry's solubility constants at 298K.

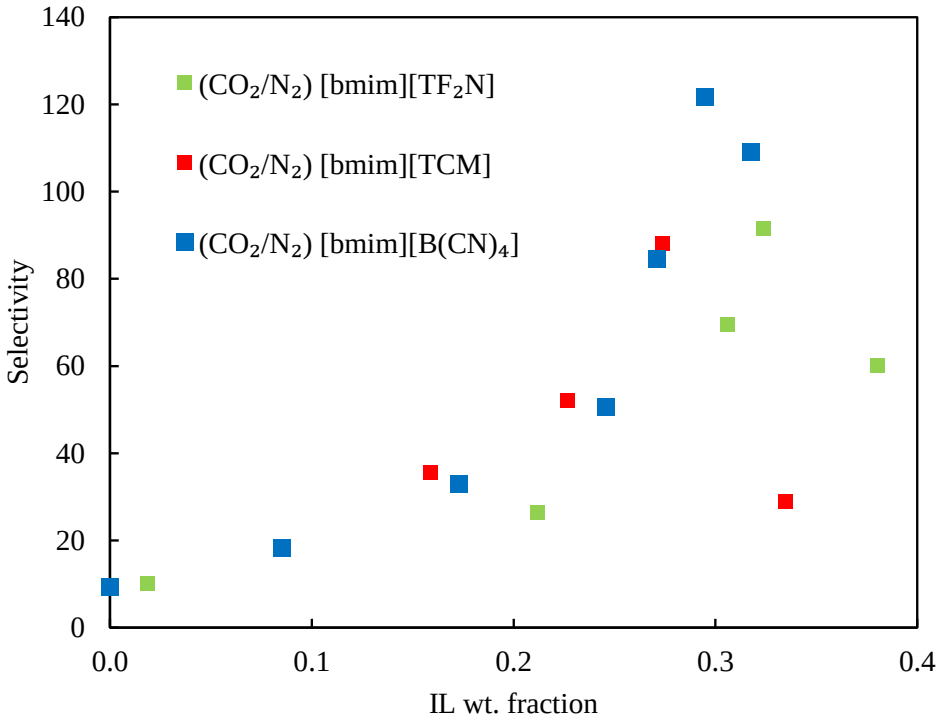

Figure 25: CO_2/N_2 Selectivity vs. IL wt. % in ZIF-8 for the three ILs

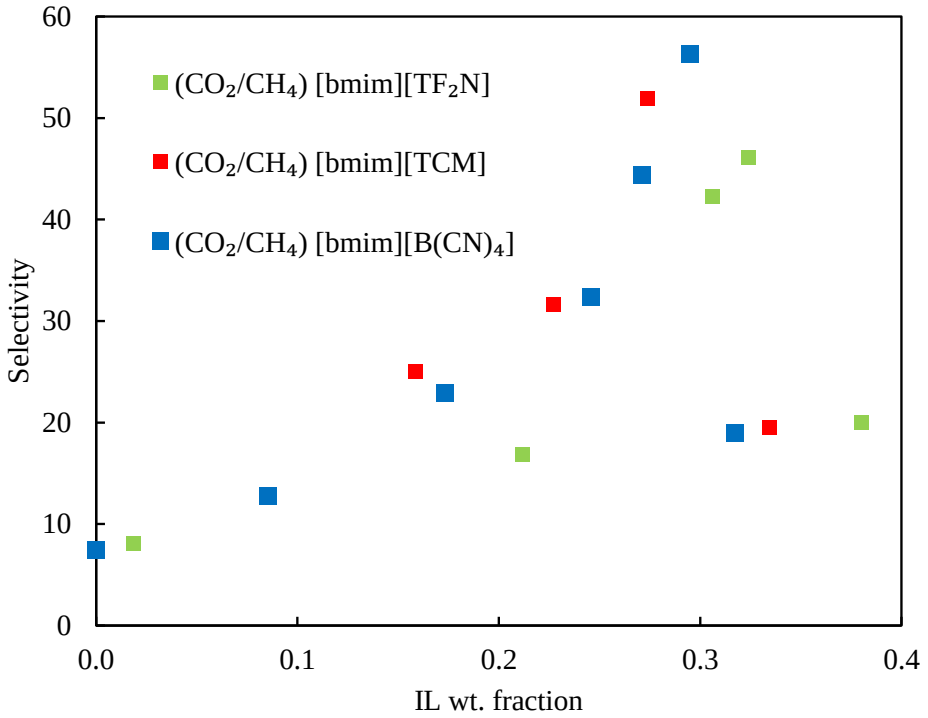

Figure 26: CO_2/CH_4 Selectivity vs. IL wt. % in ZIF-8 for the three ILs

Figure 25 and Figure 26 illustrate how selectivities vary as a function of IL weight fraction for the three ILs encapsulated into a ZIF-8 super cell. The selectivity is plotted per weight percentage to demonstrate the improvement achieved per weight of the composite ($M_{[bmim][Tf_2N]} \approx 419$ g mol^{-1}, $M_{[bmim][TCM]} \approx 229$ g mol^{-1}, $M_{[bmim][B(CN)_4]} \approx 254$ g mol^{-1}). From the CO_2/N_2 and CO_2/CH_4 selectivities values, higher enhancement is accomplished by incorporating [bmim][TCM] as an alternative to [bmim][Tf_2N] into ZIF-8. It is essential to point out that CO_2 capacity in both systems approaches an optimum value; moreover, selectivity trend is preserved, at high IL composition, as seen from Figure 25 and Figure 26. An immediate reason can be related to the size of the anion in use. Simulations showed that we can integrate up to 3 [bmim][TCM] pairs into a ZIF-8 cage, as opposed to 2 [bmim][Tf_2N] pairs. This outcome directly influences the accessible pore volume available, since the bulky 1-butyl-3-methylimidazolium cation (effective radius = 3.54 Å (≈ 186 Å^3) [188]) covers a relatively huge volume and does not contribute to CO_2 affinity significantly based on experimental and theoretical calculations. In fact, there is no adsorbed N_2 at the maximum composition explored for [bmim][TCM].

The common exponential increase in selectivites as ILs increases at lower compositions is essentially driven by immediate CO_2 capacity enhancement. CH_4 and N_2 adsorptions are not as sensitive as CO_2 adsorption and mainly influenced by the confinement effect. It can be shown that CH_4 and N_2 adsorption loadings at very low IL compositions in IL@ZIF-8 are close to the pristine ZIF-8 values. This can be looked at by highlighting the adsorption sites in ZIF-8 for the case of gases and ILs.

Usually, computational results from ZIFs are followed by an analysis of adsorption sites in ZIFs, which helps in understanding the adsorption mechanism. In ZIF-8, by calculating

potential energy surfaces, adsorption sites were divided between those controlled by van der Waals and electrostatic forces exerted by ZIF-8 on the adsorbed molecules [45], [47], [176], [177], [194]. Most of the results agree on defining adoption sites in ZIF-8. However, some defined additional sites [177]. It has been demonstrated that the primary adsorption site is where one observes a maximum in the vdW interactions [47]. The vdW interactions are higher inside the sodalite cage. Another site is at the center of the 6-ring channel, where the methyl groups are pointing, and this fact can be both explained by electrostatic or vdW interactions. At high loading, the middle of the ZIF-8 cavity is considered another site of adsorption, where it is highly influenced by the interaction between adsorbed molecules rather adsorbate-adsorbent interactions.

From computational works done on IL@MOFs composites [32], [36]–[38], it has been shown that the IL cation resides in the MOF cavity, whereas, the anion usually have a strong interaction with the metal cluster. A further structural investigation is indeed necessary, but one can point out that at a relatively low number of ILs, CH_4 and N_2 are not affected [37].

In order to understand the influence of the reduction in pore volume in determining the maximum selectivity in these composites, the selectivity vs. composition curve must be revisited. The maximum selectivity trend is derived by CO_2 capacity, which increases due to the presence of ILs pair, then decreases when confinement effect dominates. A parameter called available pore volume (APV) is used in this analysis. APV is defined as the fraction of pore volume blocked by IL pairs. A value of unity corresponds to pristine ZIF-8 pore volume; and on the other extreme, zero corresponds to total volume coverage in ZIF-8. A higher "packing factor" is expected to increase with lower molar volume ILs. Figure 27 and Figure 28 display the effect of pore volume on CO_2/N_2 and CO_2/CH_4, respectively.

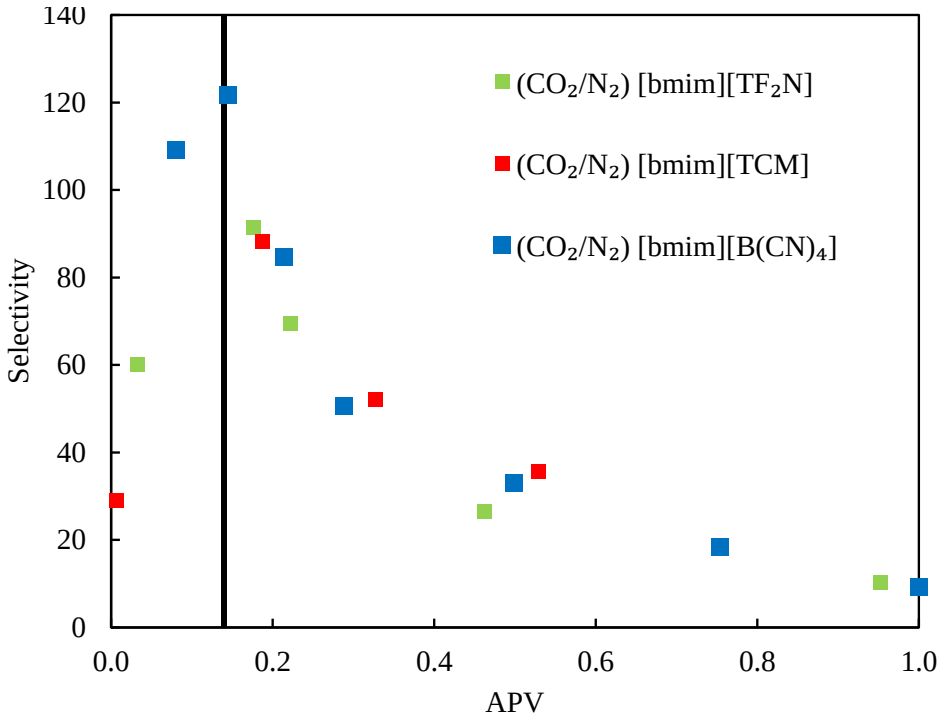

Figure 27: CO_2/N_2 Selectivity vs. APV in ZIF-8 for the three ILs

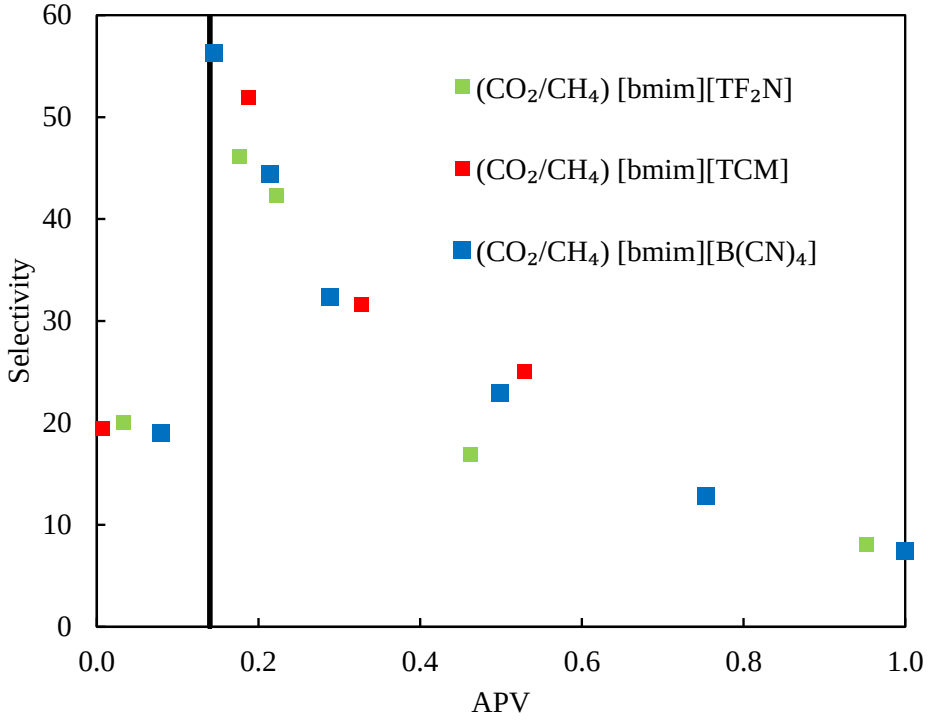

Figure 28: CO_2/CH_4 Selectivity vs. APV in ZIF-8 for the three ILs

It can be seen from these figures that the maximum CO_2 selectivties can be determined from the volume occupied by the IL. The maximum selectivity is found at very high IL composites where the adsorption of different species is extremely influenced by the reduction in pore volume. The dark straight line marks a point in which the three ILs@ZIF-8 approximately share the maximum selectivity in the composites. The values of the selectivity do differ with IL; however, the maximum is located at approx. APV=0.16. According to this analysis, one can predict the required amount of IL pairs to attain the maximum selectivity in IL@ZIF-8.

4.6. Insight into the variation/differences between initial configurations

In order to have a better assessment of the initial configuration of IL@ZIF-8, especially at intermediate compositions, labeling the specific IL formation in the composite might be necessary to ensure uniqueness among the initial configurations. A simple algorithm is used to identify the positioning of an IL pair in one of the eight unit cells in ZIF-8 (2×2×2) super cell.

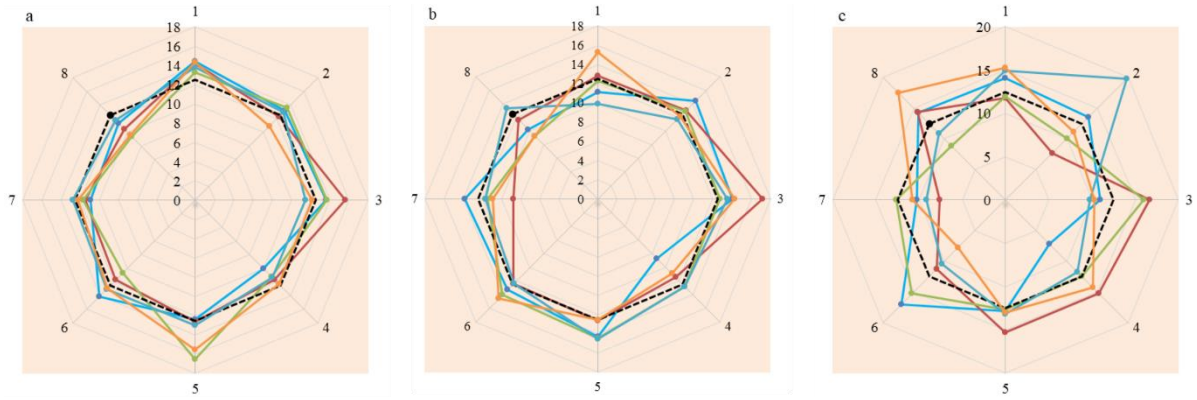

Figure 29: [bmim][TCM] distribution percentage in the 8 unit cells (1-to-8) of ZIF-8 super cell at ((a) 27.4 (b) 22.7 (c) 15.9) IL wt.%

The dashed black line in Figure 29 illustrates the uniform distribution of IL, blue, red, and green solid lines are of five distinct initial configuration. From Figure 29 we observe the

dispersity found at 15.9 wt. % compared to 22.7 and 27.4 wt. %. Given the maximum number of IL that can reside in a given ZIF-8 unit cell, one reason that justifies what Figure 29 represents is the IL formation distribution possibility in the solid structure. Moreover, the plot reveals the differences between the five studied configurations, gaging the deviation from the uniform distribution shown as a dashed black line. It is vital to point out that the uniform distribution may not be achievable.

Overall, configurations that have higher IL dispersion is reflected with higher CO_2 selectivities. The dispersity is quantified by comparisons to the uniform distribution case. Furthermore, the influence of initial configurations seems to have higher impact on CO_2/CH_4 selectivity than CO_2/N_2 selectivity by considering the coefficient of variance. This mentioned point consists with a previous research work [195].

4.7. Comparison between the three studied ILs

To investigate the properties of IL@ZIF-8 composite for CO_2 capture, the adsorbed CO_2 amount is plotted versus molar, weight and molar fractions of the different ILs in ZIF-8. The first plot (Loading versus IL to ZIF-8 molar ratio), Figure 30, demonstrates the marginal increase of adding one IL pair into the structure. At low molar compositions, one can observe the resemblance between the different ILs, avoiding the confinement effect. This can be explained by comparing pure bulk IL CO_2 Henry's constant at 298.15 K, 32.3 [26], 33.2 [154], 34.3 [187] for $[B(CN)_4]$, [TCM], and $[Tf_2N]$, respectively. Figure 31 (Loading versus weight fraction of ILs) shows that with low molecular weight (also low molar volume), we achieve an increase in capacity as [TCM] > $[(B(CN)_4]$ > $[Tf_2N]$ based at the same weight fraction. The difference can be clearly seen between the bulky $[Tf_2N]$ and smaller [TCM]; where it is possible to fit higher anions molecules into the structure at the same molecular weight. From

both Figure 30 and Figure 31, we observe some resemblance between the tendencies to adsorb CO_2 in these composites.

One way to understand and exploit this observation is by creating a plot that combines the similarities. Figure 32 is established to serve the purpose (Loading versus volume fraction ϕ), in which volume fraction is defined as the ratio of IL to the maximum capacity of IL in ZIF-8. The volume fraction ranges from 0 to 1, where 1 implies the maximum capacity of a given IL into ZIF-8. Attempting to fit all gathered data, a third degree polynomial function is used to describe the given points as can be seen in Figure 32. The black curves enclose the points within 10% of the best fitted curve. This figure can act as a general explanation of the maximum CO_2 capacity in these composites, and this is tidily relative to the maximum capacity of IL in ZIF-8.

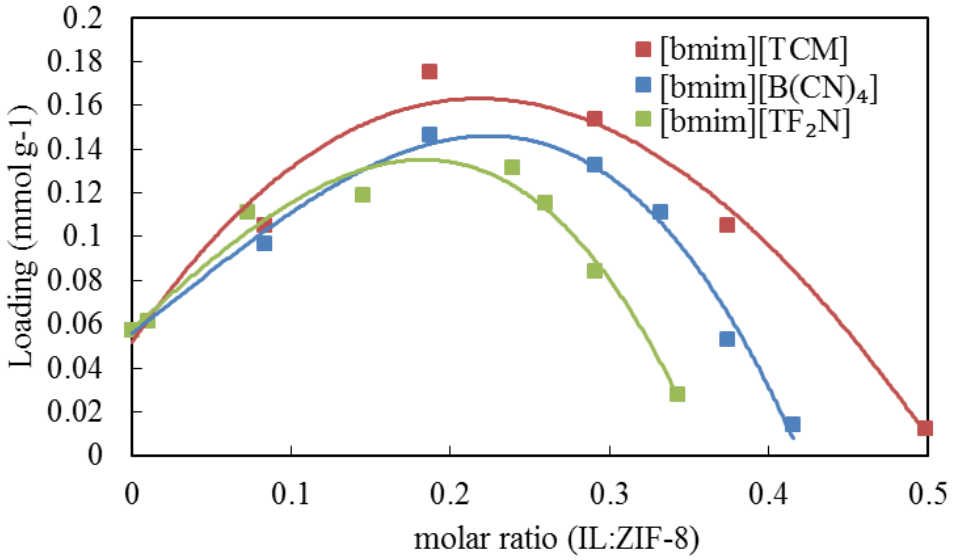

Figure 30: Loading capacity of CO_2 vs IL:ZIF-8 molar ratio at (298.15K, 0.065 bar)

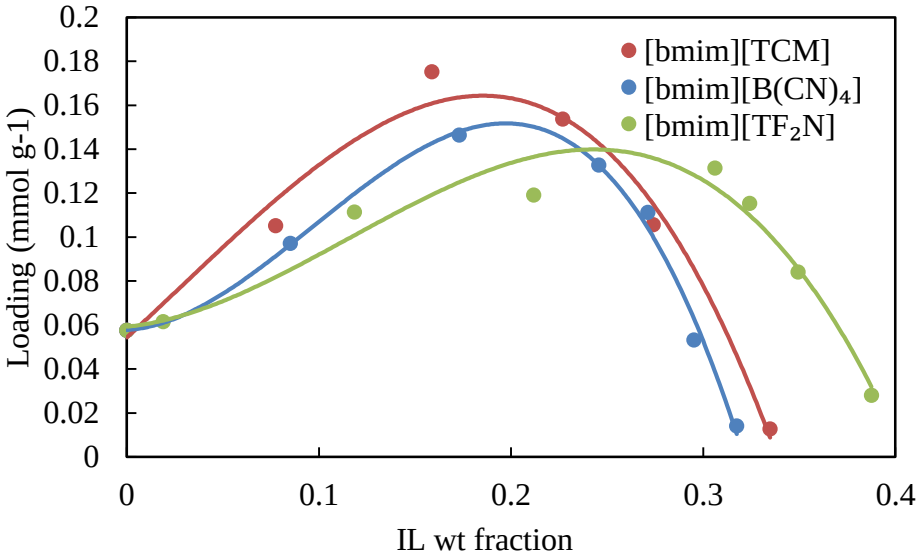

Figure 31: Loading capacity of CO_2 vs IL weight fraction at (298.15K, 0.065 bar)

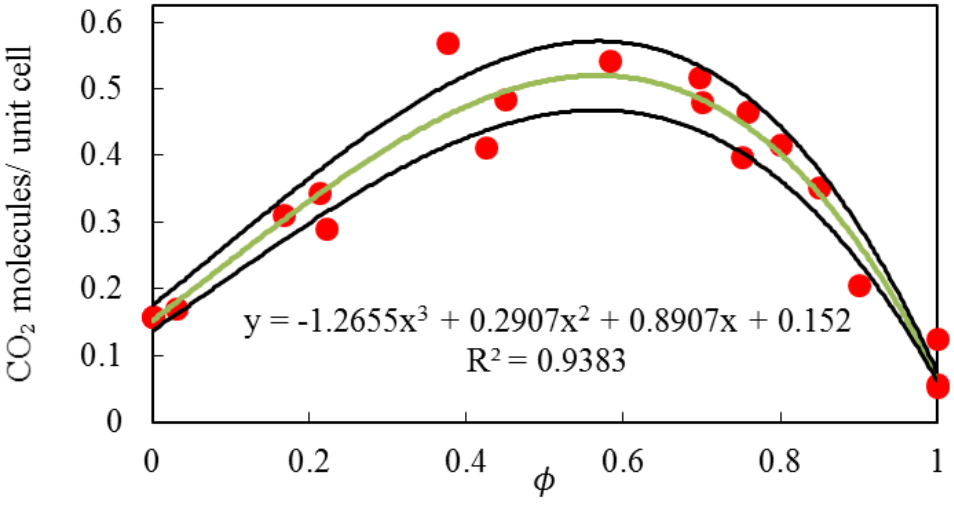

Figure 32: Number of adsorbed CO_2 (molecules/unit cell) vs volume fraction of IL at (298.15K, 0.065 bar)

4.8. Sorbent selection parameter

In commercial applications, the sorbent is required to be regenerated to fulfill smooth continuous separation operations. Different forms of cyclic adsorption routes have been

developed to achieve this objective. Temperature Swing Adsorption (TSA) is typically utilized in purification processes (less than 10 wt.% from the stream). Bulk separation, which is characterized by (more than 10 wt. % from the stream), on the other hand, is most suitably handled with Pressure Swing Adsorption (PSA) [8], [196].

First, TSA processes, the oldest and most mature cycle, is used by increasing the temperature to regenerate the sorbent by preheated gas. The time limiting step in TSA is obviously the regeneration step. The cycle length ranges from hours to days, due to the time needed for heating, desorption, and cooling down the bed. Dual bed systems are the most commonly employed for TSA. There is a characteristic temperature T_0, above which, we achieve effective desorption. It is the temperature at which the slope of the isotherm at the origin is equal to the ratio of the heat capacity of the solid phase (sorbent and adsorbate collectively) and inert carrier gas [8]. Taking into account economical evaluation, mainly operational cost of the overall process, the characteristic temperature is the optimal temperature.

Second, PSA reduces total pressure to regenerate the sorbent bed. The processes are characterized by the short cycle time, because of the possibility of fast pressure reduction. The design of PSA processes relies on product purity, product recovery, and adsorbent productivity. It is known that the recovery is proportional to the energy requirement. Also, the size of the sorbent bed decreases as sorbent productivity increases. Skarstorm and Guerom-Domine independently designed the first pressure swing processes operation [197], [198]. Skarstorm cycle (heatless adsorption) was directly implemented as a method for air drying, whereas, Guerom-Domine cycle is the core concept of vacuum swing cycles, and the design is flexible, as the number of beds can vary between 1 to 6.

Taking the separation factor proposed by Rage and Yang [184], as it based on clear theoretical background and combine both, equilibrium selectivity and capture the dynamicity of a vacuum pressure swing adsorption between desired and undesired components. The adsorption and desorption operating pressures are at 1.0 and 0.1 bar, respectively. The addition of the working capacity (W) term offers a mean to compare between various materials for gas separation based on preferential adsorption, especially in separation processes were kinetic driver separation cannot be exploited.

- Working capacity:

$$(W) = \frac{\Delta q_1}{\Delta \mathrm{q}_2} \tag{46}$$

where Δq_{i} is the working capacity of component i at the selected operating pressures.

- Equilibrium selectivity:

$$(\alpha_{1,2}) = \frac{q_{m1} b_1}{q_{m2} b_2} \tag{47}$$

where $q_{m\mathrm{i}} b_{\mathrm{i}}$ is simply the slope of the initial portion of the adsorption isotherm of component i.

We may also add a regenerability factor R (%)[199], and it is defined as the ratio of the CO_2 working capacity to the adsorbed amount at adsorption conditions. The parameter is used in this work to predict efficiency of adsorption-desorption cycle operation. The value of R (%) corresponds to the fractional percentage of adsorption sites that are available for regeneration at the adsorption-desorption cycle [199].

$$R\ (\%) = \frac{\Delta N}{N} \times 100 \tag{48}$$

Table 10 compares between different materials: a material that presents the higher sorbent parameter is considered the best sorbent, not considering other factors such as compatibility and cost.

The sorbent parameter estimation of [bmim][Tf_2N], [bmim][TCM] and [bmim][$B(CN)_4$] was selected at the given compositions that reflect the CO_2 affinity peak and equilibrium selectivity. At the listed compositions, the IL@ZIF-8 composites have a comparable capacity at Henry's regime; however, what mainly dictate the magnitude of the sorbent performance parameter is the adsorbed amount at the adsorption conditions (beyond Henry's regime pressure range for these composites) and the working capacities of CH_4 and N_2. For instance, [bmim][$B(CN)_4$] had higher capacity at the adsorption stage, but relatively higher CH_4 and N_2 adsorption than the two other ILs, which impacted the overall working capacity of the material.

It is important to mention that sorbent selection parameters reported for some adsorbent are determined from a binary mixture. In this work, pure component isotherms were used, but this gives a recognizable potential of the new composites. The mentioned study will hopefully be integrated into future studies with mixtures adsorption isotherms. The regenerability parameter value reached 72.8%, 80.1% and 83.7% with the studied [bmim][Tf_2N], [bmim][TCM] and [bmim][$B(CN)_4$], respectively. All of these R% values are comparable and even better than some familiar adsorbent at the specified adsorption-desorption conditions [199]. One would attempt to relate the R% to the total weight of the composite, but such trend is not obvious and easily generalized in this particular analysis, which echoes the adsorption loading behavioral differences between the various ILs@ZIF-8.

Table 10: Sorbent selection parameter (S) for many adsorbents

Adsorbent	Sorbent selection parameter (S)		Ref
	CO_2/N_2	CO_2/CH_4	
Zeolite-5A	**163**	**-**	**[200]**
Zeolite-13X	**128**	**19.1**	
ZIF-78	**396**	**-**	
ZIF-79	**83**	**-**	
ZIF-81	**101**	**-**	
ZIF-82	**105**	**20.5**	
Mg-MOF-74	**-**	**23.5**	
Ni-MOF-74	**83.5**	**21.0**	
HKUST-1	**-**	**19.8**	
ZIF-8[(2)]	6.1	7.7	This work
[bmim][Tf_2N]@ZIF-8 (30.6 wt. %)[(2)]	503	64	
[bmim][TCM]@ZIF-8 (22.7 wt. %)[(2)]	417	62	
[bmim][$B(CN)_4$]@ZIF-8 (24.6 wt. %)[(2)]	253	39	

[bmim][TCM] has exceptionally high sorbent parameter at effectively lower weight fraction than the studied [bmim][Tf_2N] and [bmim][$B(CN)_4$] incorporations. In overall, one can conclude the superiority of the new IL@ZIF-8 composites over all the material listed in Table 10, especially when it comes to CO_2/CH_4 mixture.

5. CONCLUSIONS AND FUTURE WORK

In this work, molecular simulation techniques were employed to investigate the adsorption-based separation of CO_2, CH_4, N_2 gases in pure ZIF-8, most importantly in ILs encapsulated in ZIF-8 (IL@ZIF-8) composites. Simulation of adsorption in pure ZIF-8 was utilized initially as a verification process. The adsorption affinity with the addition of $[bmim^+][Tf_2N^-]$ IL pairs has been quantified, and the role of IL was captured accurately. Ideal selectivity was calculated from the ratio of the initial slopes of pure adsorption isotherms of the studied components for the evaluation of adsorption-based separation performance of the material. A selectivity versus composition plot demonstrates the variation in CO_2 selectivity trend with IL composition. The plot reveals that these selectivities increase as IL composition increases up to a maximum value corresponding to a specific composition. The results suggest a trade-off between CO_2 selectivity and capacity at high IL molar ratio in ZIF-8. Respecting post-combustion gas separation operating conditions, the computed selectivities exhibit promising and competitive outcomes. Throughout similar studies, it is possible to examine different combinations of IL@ZIFs towards CO_2 capture and to propose new IL@ZIFs composites that achieve improved CO_2 selectivity and capacity.

Similar analysis of CO_2 selectivity as a function of IL@ZIF-8 compositions were also presented, featuring $[TCM^-]$ and $[B(CN)_4^-]$ based ILs. The force fields' parameters in use for the mentioned ILs families have been optimized by the research group of the principal supervisor of this thesis [189], [190]. Special emphasis was pointed at the anion effect on CO_2 affinity and selectivity, keeping the same 1-butyl-3-methylimidazolium ion. $[bmim^+][TCM^-]$ showed higher CO_2 capacity than that measured for $[bmim^+][Tf_2N^-]$ and $[bmim^+][B(CN)_4^-]$.

In addition, the highest CO_2 selectivites at a given IL weight fraction were recorded by [$bmim^+$][TCM^-], especially at relatively low IL compositions in ZIF-8.

Moreover, in order to combine both equilibrium selectivity and capture the dynamicity of vacuum pressure swing adsorption between desired and undesired components, the separation factor proposed by Rage and Yang (see Table 8) alongside a regenerability factor were adopted to further compare the new obtained structures with familiar solid sorbents. A competitive regenerability factor of 80% and 84% were determined for [$bmim^+$][Tf_2N^-] and [$bmim^+$][$B(CN)_4^-$], respectively.

Also, in order to have a better assessment of the initial configuration of IL@ZIF-8, especially at intermediate IL compositions, labelling the specific IL formation in the composite might be necessary to avoid resemblance between initial configurations. A simple algorithm was used to identify the positioning of an IL pair in one of the simulated eight unit cells in ZIF-8 (2×2×2) super cell in simulation. It was showed that the CO_2/CH_4 selectivity is more sensitive to IL dispersion than CO_2/N_2 selectivity. Overall, higher IL pairs dispersion leads to higher CO_2 selectivities.

Future work includes studying the influence of the cation on CO_2 selectivity. The cation selection has been shown to have less impact on CO_2 solubility (section 2.5.2); however, encapsulating cation [emim] instead of the currently used [bmim], will allow for additional IL pairs in the structure. Therefore, it may enhance affinity towards CO_2, while altering the CH_4 and N_2 adsorption. Due to the properties and results determined previously (section 4.5 and 4.8), investigating [emim][TCM] would be the first pick for further analysis.

REFERENCES

[1] L. Li, N. Zhao, W. Wei, and Y. Sun, "A review of research progress on CO2 capture, storage, and utilization in Chinese Academy of Sciences," in *Fuel*, 2013, vol. 108, pp. 112–130.

[2] "Earth CO2." [Online]. Available: https://www.co2.earth/. [Accessed: 24-Feb-2018].

[3] P. D. Vaidya and E. Y. Kenig, "CO2-Alkanolamine Reaction Kinetics: A Review of Recent Studies," *Chem. Eng. Technol.*, vol. 30, no. 11, pp. 1467–1474, 2007.

[4] S. Freguia and G. T. Rochelle, "Modeling of CO2 capture by aqueous monoethanolamine," *AIChE J.*, vol. 49, no. 7, pp. 1676–1686, 2003.

[5] J. D. Figueroa, T. Fout, S. Plasynski, H. McIlvried, and R. D. Srivastava, "Advances in CO2 capture technology—The U.S. Department of Energy's Carbon Sequestration Program," *Int. J. Greenh. Gas Control*, vol. 2, no. 1, pp. 9–20, 2008.

[6] S. Qiu, M. Xue, and G. Zhu, "Metal–organic framework membranes: from synthesis to separation application," *Chem. Soc. Rev.*, vol. 43, no. 16, pp. 6116–6140, 2014.

[7] S. Keskin, T. M. van Heest, and D. S. Sholl, "Can metal-organic framework materials play a useful role in large-scale carbon dioxide separations?," *ChemSusChem*, vol. 3, no. 8, pp. 879–891, 2010.

[8] R. T. Yang, *Adsorbents : Fundamentals and Applications*. Hoboken: Wiley-

Interscience, 2003.

[9] J. D. Seader, E. J. Henley, and D. K. Roper, *Separation Process Princeples*. 2011.

[10] K. S. Knaebel, "For your next separation consider adsorption," *Chem. Eng. (New York)*, vol. 102, no. 11, 1995.

[11] K. S. Park *et al.*, "Exceptional chemical and thermal stability of zeolitic imidazolate frameworks.," *Proc. Natl. Acad. Sci. U. S. A.*, vol. 103, no. 27, pp. 10186–91, 2006.

[12] J. R. Li *et al.*, "Carbon dioxide capture-related gas adsorption and separation in metal-organic frameworks," *Coordination Chemistry Reviews*, vol. 255, no. 15–16. pp. 1791–1823, 2011.

[13] H. Bux, C. Chmelik, R. Krishna, and J. Caro, "Ethene/ethane separation by the MOF membrane ZIF-8: Molecular correlation of permeation, adsorption, diffusion," *J. Memb. Sci.*, vol. 369, no. 1–2, pp. 284–289, 2011.

[14] C. Gücüyener, J. Van Den Bergh, J. Gascon, and F. Kapteijn, "Ethane/ethene separation turned on its head: Selective ethane adsorption on the metal-organic framework ZIF-7 through a gate-opening mechanism," *J. Am. Chem. Soc.*, vol. 132, no. 50, pp. 17704–17706, 2010.

[15] L. Diestel, H. Bux, D. Wachsmuth, and J. Caro, "Pervaporation studies of n-hexane, benzene, mesitylene and their mixtures on zeolitic imidazolate framework-8 membranes," *Microporous Mesoporous Mater.*, vol. 164, pp. 288–293, 2012.

[16] Y. Ban *et al.*, "Metal-substituted zeolitic imidazolate framework ZIF-108: Gas-sorption and membrane-separation properties," *Chem. - A Eur. J.*, vol. 20, no. 36, pp. 11402–11409, 2014.

[17] H. T. Kwon, H. K. Jeong, A. S. Lee, H. S. An, and J. S. Lee, "Heteroepitaxially Grown Zeolitic Imidazolate Framework Membranes with Unprecedented Propylene/Propane Separation Performances," *J. Am. Chem. Soc.*, vol. 137, no. 38, pp. 12304–12311, 2015.

[18] P. Krokidas *et al.*, "ZIF-67 Framework: A Promising New Candidate for Propylene/Propane Separation. Experimental Data and Molecular Simulations," *J. Phys. Chem. C*, vol. 120, no. 15, pp. 8116–8124, 2016.

[19] J. A. Thompson, J. T. Vaughn, N. A. Brunelli, W. J. Koros, C. W. Jones, and S. Nair, "Mixed-linker zeolitic imidazolate framework mixed-matrix membranes for aggressive CO2 separation from natural gas," *Microporous Mesoporous Mater.*, vol. 192, pp. 43–51, 2014.

[20] B. Zheng, L. L. Wang, L. Du, K. W. Huang, and H. Du, "ZIF-8 gate tuning via terminal group modification: A computational study," *Chem. Phys. Lett.*, vol. 658, pp. 270–275, 2016.

[21] A. Berthod, M. J. Ruiz-Ángel, and S. Carda-Broch, "Ionic liquids in separation techniques," *J. Chromatogr. A*, vol. 1184, no. 1–2, pp. 6–18, 2008.

[22] R. L. Vekariya, "A review of ionic liquids: Applications towards catalytic organic transformations," *J. Mol. Liq.*, vol. 227, p. 40, 2017.

[23] Z. Zhang, J. Song, and B. Han, "Catalytic Transformation of Lignocellulose into Chemicals and Fuel Products in Ionic Liquids," *Chemical Reviews*, vol. 117, no. 10. pp. 6834–6880, 2017.

[24] J. An, M. J. Trujillo-Rodríguez, V. Pino, and J. L. Anderson, "Non-conventional solvents in liquid phase microextraction and aqueous biphasic systems," *Journal of Chromatography A*, vol. 1500. pp. 1–23, 2017.

[25] I. Cota and F. Fernandez Martinez, "Recent advances in the synthesis and applications of metal organic frameworks doped with ionic liquids for CO2 adsorption," *Coord. Chem. Rev.*, vol. 35, pp. 189–204, 2017.

[26] S. M. Mahurin, P. C. Hillesheim, J. S. Yeary, D. Jiang, and S. Dai, "High CO2 solubility, permeability and selectivity in ionic liquids with the tetracyanoborate anion," *RSC Adv.*, vol. 2, no. 31, p. 11813, 2012.

[27] Y. Liu, Y. Ban, and W. Yang, "Microstructural Engineering and Architectural Design of Metal-Organic Framework Membranes," *Adv. Mater.*, vol. 29, no. 31, 2017.

[28] M. Ramdin, T. W. de Loos, and T. J. H. Vlugt, "State-of-the-Art of CO2 Capture with Ionic Liquids," *Ind. Eng. Chem. Res.*, vol. 51, no. 24, pp. 8149–8177, 2012.

[29] Y. Ban *et al.*, "Confinement of Ionic Liquids in Nanocages: Tailoring the Molecular Sieving Properties of ZIF-8 for Membrane-Based CO2 Capture," *Angew. Chemie - Int. Ed.*, vol. 54, no. 51, pp. 15483–15487, 2015.

[30] H. Li *et al.*, "Simultaneous enhancement of mechanical properties and CO2 selectivity

of ZIF-8 mixed matrix membranes: Interfacial toughening effect of ionic liquid," *J. Memb. Sci.*, vol. 511, pp. 130–142, 2016.

[31] M. Hasib-ur-Rahman, M. Siaj, and F. Larachi, "Ionic liquids for CO2 capture-Development and progress," *Chemical Engineering and Processing: Process Intensification*, vol. 49, no. 4. pp. 313–322, 2010.

[32] K. M. Gupta, Y. Chen, Z. Hu, and J. Jiang, "Metal-organic framework supported ionic liquid membranes for CO2 capture: anion effects.," *Phys. Chem. Chem. Phys.*, vol. 14, no. 16, pp. 5785–94, 2012.

[33] B. Zornoza, O. Esekhile, W. J. Koros, C. Téllez, and J. Coronas, "Hollow silicalite-1 sphere-polymer mixed matrix membranes for gas separation," *Sep. Purif. Technol.*, vol. 77, no. 1, pp. 137–145, 2011.

[34] Y. Dai, J. R. Johnson, O. Karvan, D. S. Sholl, and W. J. Koros, "Ultem®/ZIF-8 mixed matrix hollow fiber membranes for CO2/N2 separations," *J. Memb. Sci.*, vol. 401, pp. 76–82, 2012.

[35] M. A. Aroon, A. F. Ismail, T. Matsuura, and M. M. Montazer-Rahmati, "Performance studies of mixed matrix membranes for gas separation: A review," *Sep. Purif. Technol.*, vol. 75, no. 3, pp. 229–242, 2010.

[36] Y. Chen, Z. Hu, K. M. Gupta, and J. Jiang, "Ionic Liquid/Metal Organic Framework Composite for CO2 Capture: A Computational Investigation," *J. Phys. Chem. C*, vol. 115, no. 44, pp. 21736–21742, 2011.

[37] J. M. Vicent-Luna, J. J. Gutiérrez-Sevillano, J. A. Anta, and S. Calero, "Effect of Room-Temperature Ionic Liquids on CO 2 Separation by a Cu-BTC Metal–Organic Framework," *J. Phys. Chem. C*, vol. 117, no. 40, pp. 20762–20768, 2013.

[38] K. M. Gupta, Y. Chen, and J. Jiang, "Ionic Liquid Membranes Supported by Hydrophobic and Hydrophilic Metal–Organic Frameworks for CO2 Capture," *J. Phys. Chem. C*, vol. 117, no. 3, pp. 5792–5799, 2013.

[39] M. P. Allen and D. J. Tildesley, *Computer Simulation of Liquids*. New York, NY, USA: Clarendon Press, 1989.

[40] P. D. Kolokathis, G. Kali, H. Jobic, and D. N. Theodorou, "Diffusion of Aromatics in Silicalite-1: Experimental and Theoretical Evidence of Entropic Barriers," *J. Phys. Chem. C*, vol. 120, no. 38, pp. 21410–21426, 2016.

[41] J. Yu, L.-H. Xie, J.-R. Li, Y. Ma, J. M. Seminario, and P. B. Balbuena, "CO $_2$ Capture and Separations Using MOFs: Computational and Experimental Studies," *Chem. Rev.*, vol. 117, no. 14, pp. 9674–9754, 2017.

[42] M. V. Parkes, H. Demir, S. L. Teich-Mcgoldrick, D. S. Sholl, J. A. Greathouse, and M. D. Allendorf, "Molecular dynamics simulation of framework flexibility effects on noble gas diffusion in HKUST-1 and ZIF-8," *Microporous Mesoporous Mater.*, vol. 194, pp. 190–199, 2014.

[43] R. J. Verploegh, S. Nair, and D. S. Sholl, "Temperature and Loading-Dependent Diffusion of Light Hydrocarbons in ZIF-8 as Predicted Through Fully Flexible

Molecular Simulations," *J. Am. Chem. Soc.*, vol. 137, no. 50, pp. 15760–15771, 2015.

[44] R. Krishna and J. M. van Baten, "Using Molecular Dynamics simulations for elucidation of molecular traffic in ordered crystalline microporous materials," *Microporous Mesoporous Mater.*, vol. 258, pp. 151–169, 2018.

[45] X. Wu, J. Huang, W. Cai, and M. Jaroniec, "Force field for ZIF-8 flexible frameworks: atomistic simulation of adsorption, diffusion of pure gases as CH4, H2, CO2 and N2," *RSC Adv.*, vol. 4, no. 32, pp. 16503–16511, 2014.

[46] E. Pantatosaki, H. Jobic, D. I. Kolokolov, S. Karmakar, R. Biniwale, and G. K. Papadopoulos, "Probing the hydrogen equilibrium and kinetics in zeolite imidazolate frameworks via molecular dynamics and quasi-elastic neutron scattering experiments," *J. Chem. Phys.*, vol. 138, no. 3, 2013.

[47] J. Pérez-Pellitero *et al.*, "Adsorption of CO2, CH4, and N2 on zeolitic imidazolate frameworks: Experiments and simulations," *Chem. - A Eur. J.*, vol. 16, no. 5, pp. 1560–1571, 2010.

[48] F. P. Kinik, C. Altintas, V. Balci, B. Koyuturk, A. Uzun, and S. Keskin, "[BMIM][PF6] Incorporation Doubles CO2 Selectivity of ZIF-8: Elucidation of Interactions and Their Consequences on Performance," *ACS Appl. Mater. Interfaces*, vol. 8, no. 45, pp. 30992–31005, 2016.

[49] E. Androulaki, N. Vergadou, J. Ramos, and I. G. Economou, "Structure, thermodynamic and transport properties of imidazolium-based bis(trifluoromethylsulfonyl)imide ionic

liquids from molecular dynamics simulations," *Mol. Phys.*, vol. 110, no. 11–12, pp. 1139–1152, 2012.

[50] P. Krokidas, M. Castier, S. Moncho, E. Brothers, and I. G. Economou, "Molecular Simulation Studies of the Diffusion of Methane, Ethane, Propane, and Propylene in ZIF-8," *J. Phys. Chem. C*, vol. 119, no. 48, pp. 27028–27037, 2015.

[51] P. Krokidas, M. Castier, and I. G. Economou, "Computational Study of ZIF-8 and ZIF-67 Performance for Separation of Gas Mixtures," *J. Phys. Chem. C*, vol. 121, no. 33, pp. 17999–18011, 2017.

[52] K. Houghton, J.T., Y. Ding, D.J. Griggs, M. Noguer, P.J. van der Linden, X. Dai and and C. A. J. Maskell, *IPCC,2001: Climate change 2001: The scientific basis. Contribution of Working Group I to the Third Assessment Report of the Intergovernmental Panel on Climate Change*. Cambridge University Press, Cambridge, United Kingdom and New York, NY, USA, 2001.

[53] O. Dr. Bolland, *O. IPCC, IPCC Special Report on Carbon Dioxide Capture and Storage*. Cambridge University Press: Cambridge, 2009.

[54] D. M. D'Alessandro, B. Smit, and J. R. Long, "Carbon dioxide capture: Prospects for new materials," *Angewandte Chemie - International Edition*, vol. 49, no. 35. pp. 6058–6082, 2010.

[55] R. B. Robert, "Process for separating acidic gases," US Patent 1,783,901, Dec-1930.

[56] D. W. Bailey and P. H. M. Feron, "Post-combustion decarbonisation processes," *Oil*

Gas Sci. Technol., vol. 60, no. 3, pp. 461–474, 2005.

[57] G. T. Rochelle, "Amine Scrubbing for CO2 Capture," *Science*, vol. 325, no. 5948. pp. 1652–1654, 2009.

[58] L. I. Eide and D. W. Bailey, "Precombustion decarbonisation processes," *Oil Gas Sci. Technol.*, vol. 60, no. 3, pp. 475–484, 2005.

[59] P. Langlois *et al.*, "Carbon Dioxide Capture By Adsorption," vol. 51, no. 6, pp. 609–626, 2016.

[60] M. Anheden, J. Yan, and G. De Smedt, "Denitrogenation (or oxyfuel concepts)," *Oil Gas Sci. Technol.*, vol. 60, no. 3, pp. 485–495, 2005.

[61] S. Mills, "Coal-fired CCS demonstration plants," 2012.

[62] W. K. Lewis, E. R. Gilliland, and M. P. Sweeney, "Gasification of carbon. Metal oxides in a fluidized powder bed.," *Chem. Eng. Prog.*, vol. 47, pp. 251–256, 1951.

[63] J. C. Abanades *et al.*, "Emerging CO2 capture systems," *Int. J. Greenh. Gas Control*, vol. 40, pp. 126–166, 2015.

[64] A. R. Leach, *Molecular Modelling: Principles and Applications*. Harlow, England: Pearson/Prentice Hall, 2001.

[65] D. Dubbeldam, S. Calero, D. E. Ellis, and R. Q. Snurr, "RASPA: Molecular simulation software for adsorption and diffusion in flexible nanoporous materials," *Mol. Simul.*, vol. 42, no. 2, pp. 81–101, 2016.

[66] M. P. Allen and D. J. Tildesley, *Computer simulation of liquids*, vol. 179, no. 1–3. 2008.

[67] I. R. McDonald, "NpT-ensemble monte carlo calculations for binary liquid mixtures," *Mol. Phys.*, vol. 23, no. 1, pp. 41–58, 1972.

[68] F. Guarnieri and W. C. Still, "A rapidly convergent simulation method: Mixed Monte Carlo/stochastic dynamics," *J. Comput. Chem.*, vol. 15, no. 11, pp. 1302–1310, 1994.

[69] S. Duane, A. D. Kennedy, B. J. Pendleton, and D. Roweth, "Hybrid Monte Carlo," *Phys. Lett. B*, vol. 195, no. 2, pp. 216–222, 1987.

[70] M. E. Clamp, P. G. Baker, C. J. Stirling, and A. Brass, "Hybrid Monte Carlo: An efficient algorithm for condensed matter simulation," *J. Comput. Chem.*, vol. 15, no. 8, pp. 838–846, 1994.

[71] S. I. Sandler, *An Introduction to Applied Statistical Thermodynamics*. John Wiley & Sons, 2010.

[72] N. Metropolis, A. W. Rosenbluth, M. N. Rosenbluth, A. H. Teller, and E. Teller, "Equation of State Calculations by Fast Computing Machines," *J. Chem. Phys.*, vol. 21, no. 6, pp. 1087–1092, 1953.

[73] D. Dubbeldam, A. Torres-Knoop, and K. S. Walton, "On the inner workings of monte carlo codes," *Molecular Simulation*, vol. 39, no. 14–15. Taylor & Francis, pp. 1253–1292, 2013.

[74] I. T. Todorov, W. Smith, K. Trachenko, and M. T. Dove, "DL_POLY_3: new

dimensions in molecular dynamics simulations via massive parallelism," *J. Mater. Chem.*, vol. 16, no. 20, p. 1911, 2006.

[75] J. W. Ponder, "TINKER software tools for molecular design." [Online]. Available: http://dasher.wustl.edu/tinker.

[76] S. Plimpton, "Fast parallel algorithms for short-range molecular dynamics," *J. Comput. Phys.*, vol. 117, no. 1, pp. 1–19, 1995.

[77] H. J. C. Berendsen, D. van der Spoel, and R. van Drunen, "GROMACS: A message-passing parallel molecular dynamics implementation," *Comput. Phys. Commun.*, vol. 91, no. 1–3, pp. 43–56, 1995.

[78] J. Jorgeonsen, William; Tirado-Rives, "MCPRO, Monte Carlo Simulations for Biomolecules," 2004. [Online]. Available: http://www.cemcomco.com/MCPROman.pdf. [Accessed: 07-Mar-2018].

[79] J. P. Ulmschneider and W. L. Jorgensen, "Polypeptide Folding Using Monte Carlo Sampling, Concerted Rotation, and Continuum Solvation," *J. Am. Chem. Soc.*, vol. 126, no. 6, pp. 1849–1857, 2004.

[80] M. G. Martin, "Towhee." [Online]. Available: http://towhee.sourceforge.net/.

[81] M. G. Martin, "MCCCS Towhee: A tool for monte carlo molecular simulation," *Mol. Simul.*, vol. 39, no. 14–15, pp. 1212–1222, 2013.

[82] Materials Design, "MedeA," 2018. [Online]. Available:

http://www.materialsdesign.com/medea. [Accessed: 07-Mar-2018].

[83] A. Gupta, S. Chempath, M. J. Sanborn, L. A. Clark, and R. Q. Snurr, "Object-oriented programming paradigms for molecular modeling," *Mol. Simul.*, vol. 29, no. 1, pp. 29–46, 2003.

[84] "Scienomics – Explore anything in the world of materials." [Online]. Available: http://www.scienomics.com/.

[85] J. K. Shah and E. J. Maginn, "A general and efficient Monte Carlo method for sampling intramolecular degrees of freedom of branched and cyclic molecules," *J. Chem. Phys.*, vol. 135, no. 13, 2011.

[86] J. K. Shah *et al.*, "Cassandra: An open source Monte Carlo package for molecular simulation," *J. Comput. Chem.*, vol. 38, no. 19, pp. 1727–1739, 2017.

[87] P. L'Ecuyer, "Tables of maximally equidistributed combined LFSR generators," *Math. Comput.*, vol. 68, no. 225, pp. 261–270, 1999.

[88] E. J. Maginn *et al.*, "Computational Atomistic Simulation Software At Notre Dame for Research Advances, User Manual 1.2." 2014.

[89] P. P. Ewald, "Die Berechnung optischer und elektrostatischer Gitterpotentiale," *Ann. Phys.*, vol. 369, no. 3, pp. 253–287, 1921.

[90] C. J. Fennell and J. D. Gezelter, "Is the Ewald summation still necessary? Pairwise alternatives to the accepted standard for long-range electrostatics," *J. Chem. Phys.*, vol.

124, no. 23, 2006.

[91] J. Gasteiger and M. Marsili, “Iterative partial equalization of orbital electronegativity-a rapid access to atomic charges,” *Tetrahedron*, vol. 36, no. 22, pp. 3219–3228, 1980.

[92] R. F. Cracknell, D. Nicholson, and N. Quirke, “A grand canonical monte-carlo study of lennard-jones mixtures in slit pores; 2: Mixtures of two centre ethane with methane,” *Mol. Simul.*, vol. 13, no. 3, pp. 161–175, 1994.

[93] B. Widom, “Some Topics in the Theory of Fluids,” *J. Chem. Phys.*, vol. 39, no. 11, pp. 2808–2812, 1963.

[94] S. Toxvaerd, “Molecular dynamics calculation of the equation of state of alkanes,” *J. Chem. Phys.*, vol. 93, no. 6, pp. 4290–4295, 1990.

[95] W. W. Wood, “Monte Carlo Calculations for Hard Disks in the Isothermal- Isobaric Ensemble,” *J. Chem. Phys.*, vol. 48, no. 1, pp. 415–434, 1968.

[96] A. Z. Panagiotopoulos, “Direct determination of phase coexistence properties of fluids by monte carlo simulation in a new ensemble,” *Mol. Phys.*, vol. 61, no. 4, pp. 813–826, 1987.

[97] A. Z. Panagiotopoulos, N. Quirke, M. Stapleton, and D. J. Tildesley, “Phase equilibria by simulation in the gibbs ensemble alternative derivation, generalization and application to mixture and membrane equilibria,” *Mol. Phys.*, vol. 63, no. 4, pp. 527–545, 1988.

[98] G. Raabe, *Molecular Simulation Studies on Thermophysical Properties: With Application to Working Fluids*. Springer Singapore, 2017.

[99] K. S. W. Sing, "Reporting physisorption data for gas/solid systems with special reference to the determination of surface area and porosity (Provisional)," *Pure Appl. Chem.*, vol. 54, no. 11, 1982.

[100] R. T. Yang, *Gas Separation by Adsorption Processes*. Boston: Butterworths, 1987.

[101] T. L. Hill, *An introduction to statistical thermodynamics*. Addison-Wesley Pub. Co., 1960.

[102] A. L. Myers and J. M. Prausnitz, "Thermodynamics of mixed- gas adsorption," *AIChE J.*, vol. 11, no. 1, pp. 121–127, 1965.

[103] V. V. Guerrero, "Nanoporous Materials For Carbon Dioxide Seperation and Storage," Texas A&M University, 2011.

[104] C. H. Bartholomew and R. J. Farrauto, *Fundamentals of Industrial Catalytic Processes: Second Edition*, 2nd ed. Wiley-AlChE, 2010.

[105] M. E. Davis, "Zeolites and Molecular Sieves: Not Just Ordinary Catalysts," *Ind. Eng. Chem. Res.*, vol. 30, no. 8, pp. 1675–1683, 1991.

[106] T. J. H. Vlugt, W. Zhu, F. Kapteijn, J. A. Moulijn, B. Smit, and R. Krishna, "Adsorption of linear and branched alkanes in the zeolite silicalite-1," *J. Am. Chem. Soc.*, vol. 120, no. 22, pp. 5599–5600, 1998.

[107] S. Ban, A. Van Laak, P. E. De Jongh, J. P. J. M. Van Der Eerden, and T. J. H. Vlugt, "Adsorption selectivity of benzene/propene mixtures for various zeolites," *J. Phys. Chem. C*, vol. 111, no. 46, pp. 17241–17248, 2007.

[108] Z. Z. Du, G. Manos, T. J. H. T. Vlugt, and B. Smit, "Molecular simulation of adsorption of short linear alkanes and their mixtures in silicalite," *AIChE J.*, vol. 44, no. 8, pp. 1756–1764, 1998.

[109] B. Smit and T. L. M. Maesen, "Molecular simulations of zeolites: Adsorption, diffusion, and shape selectivity," *Chem. Rev.*, vol. 108, no. 10, pp. 4125–4184, 2008.

[110] B. Panella, M. Hirscher, H. Pütter, and U. Müller, "Hydrogen adsorption in metal-organic frameworks: Cu-MOFs and Zn-MOFs compared," *Adv. Funct. Mater.*, vol. 16, no. 4, pp. 520–524, 2006.

[111] S. S.-Y. Chui *et al.*, "A chemically functionalizable nanoporous material," *Science*, vol. 283, no. 5405, pp. 1148–50, 1999.

[112] M. R. Ryder and J.-C. Tan, "Nanoporous metal organic framework materials for smart applications," *Mater. Sci. Technol.*, vol. 30, no. 13, pp. 1598–1612, 2014.

[113] Z. Bao, G. Chang, H. Xing, R. Krishna, Q. Ren, and B. Chen, "Potential of microporous metal–organic frameworks for separation of hydrocarbon mixtures," *Energy Environ. Sci.*, vol. 9, no. 12, pp. 3612–3641, 2016.

[114] M. Shah, "Synthesis and characterization of films and membranes of Metal-Organic Framework (MOF) for gas separation applications," MSc Thesis, Texas A&M

University, 2012.

[115] R. Banerjee *et al.*, “High-throughput synthesis of zeolitic imidazolate frameworks and application to CO2 capture,” *Science (80-.).*, vol. 319, no. 5865, pp. 939–943, 2008.

[116] B. Wang, A. P. Côté, H. Furukawa, M. O’Keeffe, and O. M. Yaghi, “Colossal cages in zeolitic imidazolate frameworks as selective carbon dioxide reservoirs,” *Nature*, vol. 453, no. 7192, pp. 207–211, 2008.

[117] H. Kwon, “Developing Synthesis Techniques for Zeolitic-Imidazolate Framework Membranes for High Resolution Propylene/Propane Separation,” PhD Thesis, Texas A&M University, 2015.

[118] W. Morris *et al.*, “A combined experimental-computational investigation of carbon dioxide capture in a series of isoreticular zeolitic imidazolate frameworks,” *J. Am. Chem. Soc.*, vol. 132, no. 32, pp. 11006–11008, 2010.

[119] N. Masciocchi, G. A. Ardizzoia, G. LaMonica, A. Maspero, and A. Sironi, “Thermally robust metal coordination polymers: The cobalt, nickel, and zinc pyrimidin-2-olate derivatives,” *Eur. J. Inorg. Chem.*, vol. 2, no. 12, pp. 2507–2515, 2000.

[120] S. Y. Yang, L. S. Long, Y. B. Jiang, R. B. Huang, and L. S. Zheng, “An exceptionally stable metal-organic framework constructed from the Zn8(SiO4) core,” *Chem. Mater.*, vol. 14, no. 8, pp. 3229–3231, 2002.

[121] J. Canivet, A. Fateeva, Y. Guo, B. Coasne, and D. Farrusseng, “Water adsorption in MOFs: fundamentals and applications,” *Chem. Soc. Rev.*, vol. 43, no. 16, pp. 5594–

5617, 2014.

[122] N. C. Burtch, H. Jasuja, and K. S. Walton, “Water stability and adsorption in metal-organic frameworks,” *Chemical Reviews*, vol. 114, no. 20. pp. 10575–10612, 2014.

[123] K. Zhang *et al.*, “Alcohol and water adsorption in zeolitic imidazolate frameworks,” *Chem. Commun.*, vol. 49, no. 31, p. 3245, 2013.

[124] K. Zhang *et al.*, “Exploring the framework hydrophobicity and flexibility of zif-8: From biofuel recovery to hydrocarbon separations,” *J. Phys. Chem. Lett.*, vol. 4, no. 21, pp. 3618–3622, 2013.

[125] A. Nalaparaju, X. S. Zhao, and J. W. Jiang, “Molecular Understanding for the Adsorption of Water and Alcohols in Hydrophilic and Hydrophobic Zeolitic Metal−Organic Frameworks,” *J. Phys. Chem. C*, vol. 114, no. 26, pp. 11542–11550, 2010.

[126] A. U. Ortiz, A. P. Freitas, A. Boutin, A. H. Fuchs, and F.-X. Coudert, “What makes zeolitic imidazolate frameworks hydrophobic or hydrophilic? The impact of geometry and functionalization on water adsorption,” *Phys. Chem. Chem. Phys.*, vol. 16, no. 21, pp. 9940–9949, 2014.

[127] A. Phan, C. J. Doonan, F. J. Uribe-Romo, C. B. Knobler, M. Okeeffe, and O. M. Yaghi, “Synthesis, structure, and carbon dioxide capture properties of zeolitic imidazolate frameworks,” *Acc. Chem. Res.*, vol. 43, no. 1, pp. 58–67, 2010.

[128] J. Jiang, *Metal-organic frameworks: Materials modeling towards potential engineering applications*. CRC Press, 2015.

[129] C. Zhang, R. P. Lively, K. Zhang, J. R. Johnson, O. Karvan, and W. J. Koros, "Unexpected molecular sieving properties of zeolitic imidazolate framework-8," *J. Phys. Chem. Lett.*, vol. 3, no. 16, pp. 2130–2134, 2012.

[130] K. Li *et al.*, "Zeolitic imidazolate frameworks for kinetic separation of propane and propene," *J. Am. Chem. Soc.*, vol. 131, no. 30, pp. 10368–10369, 2009.

[131] N. V. Plechkova and K. R. Seddon, "Applications of ionic liquids in the chemical industry," *Chem. Soc. Rev.*, vol. 37, no. 1, pp. 123–150, 2008.

[132] A. Berthod, M. J. Ruiz-Ángel, and S. Carda-Broch, "Recent advances on ionic liquid uses in separation techniques," *J. Chromatogr. A*, pp. 1–15, 2017.

[133] P. McCabe, Warren L, Smith, J., Harriot, *Unit operations of chemical engineering*, 7th ed. McGraw-Hill Education, 2004.

[134] K. Ghandi, "A Review of Ionic Liquids, Their Limits and Applications," *Green Sustain. Chem.*, vol. 4, no. 1, pp. 44–53, 2014.

[135] H. Markusson, J.-P. Belières, P. Johansson, C. A. Angell, and P. Jacobsson, "Prediction of Macroscopic Properties of Protic Ionic Liquids by Ab Initio Calculations," *J. Phys. Chem. A*, vol. 111, no. 35, pp. 8717–8723, 2007.

[136] T. P. Thuy Pham, C. W. Cho, and Y. S. Yun, "Environmental fate and toxicity of ionic liquids: A review," *Water Res.*, vol. 44, no. 2, pp. 352–372, 2010.

[137] A. Klamt, *COSMO-RS: From Quantum Chemistry to Fluid Phase Thermodynamics and*

Drug Design. Amsterdam: Elsevier, 2005.

[138] X. Zhang, Z. Liu, and W. Wang, "Screening of ionic liquids to capture CO2 by COSMO-RS and experiments," *AIChE J.*, vol. 54, no. 10, pp. 2717–2728, 2008.

[139] K. Z. Sumon and A. Henni, "Ionic liquids for CO2 capture using COSMO-RS: Effect of structure, properties and molecular interactions on solubility and selectivity," *Fluid Phase Equilib.*, vol. 310, no. 1–2, pp. 39–55, 2011.

[140] J. Palomar, M. Gonzalez-Miquel, A. Polo, and F. Rodriguez, "Understanding the physical absorption of CO2 in ionic liquids using the COSMO-RS method," *Ind. Eng. Chem. Res.*, vol. 50, no. 6, pp. 3452–3463, 2011.

[141] M. Gonzalez-Miquel, J. Palomar, S. Omar, and F. Rodriguez, "CO2/N2 selectivity prediction in supported ionic liquid membranes (SILMs) by COSMO-RS," *Ind. Eng. Chem. Res.*, vol. 50, no. 9, pp. 5739–5748, 2011.

[142] S. N. V. K. Aki, B. R. Mellein, E. M. Saurer, and J. F. Brennecke, "High-pressure phase behavior of carbon dioxide with imidazolium-based ionic liquids," *J. Phys. Chem. B*, vol. 108, pp. 20355–20365, 2004.

[143] C. Cadena, J. L. Anthony, J. K. Shah, T. I. Morrow, J. F. Brennecke, and E. J. Maginn, "Why is CO2 so Soluble in Imidazolium-Based Ionic Liquids?," *J. Am. Chem. Soc.*, vol. 126, no. 16, pp. 5300–5308, 2004.

[144] M. J. Muldoon, S. N. V. K. Aki, J. L. Anderson, J. K. Dixon, and J. F. Brennecke, "Improving carbon dioxide solubility in ionic liquids," *J. Phys. Chem. B*, vol. 111, no.

30, pp. 9001–9009, 2007.

[145] J. L. Anthony, E. J. Maginn, and J. F. Brennecke, “Solubilities and Thermodynamic Properties of Gases in the Ionic Liquid 1- n -Butyl-3-methylimidazolium Hexafluorophosphate,” *J. Phys. Chem. B*, vol. 106, no. 29, pp. 7315–7320, 2002.

[146] J. L. Anthony, J. L. Anderson, E. J. Maginn, and J. F. Brennecke, “Anion Effects on Gas Solubility in Ionic Liquids,” *J. Phys. Chem. B*, vol. 109, no. 13, pp. 6366–6374, 2005.

[147] P. J. Carvalho and J. A. P. Coutinho, “The polarity effect upon the methane solubility in ionic liquids: a contribution for the design of ionic liquids for enhanced CO2/CH4 and H2S/CH4 selectivities,” *Energy Environ. Sci.*, vol. 4, no. 11, p. 4614, 2011.

[148] M. Ramdin *et al.*, “Solubility of CO2 and CH4 in ionic liquids: Ideal CO2/CH4 selectivity,” *Ind. Eng. Chem. Res.*, vol. 53, no. 40, pp. 15427–15435, 2014.

[149] D. Camper, C. Becker, C. Koval, and R. Noble, “Diffusion and solubility measurements in room temperature ionic liquids,” *Ind. Eng. Chem. Res.*, vol. 45, no. 1, pp. 445–450, 2006.

[150] D. Camper, J. Bara, C. Koval, and R. Noble, “Bulk-fluid solubility and membrane feasibility of Rmim-based room-temperature ionic liquids,” *Ind. Eng. Chem. Res.*, vol. 45, no. 18, pp. 6279–6283, 2006.

[151] A. Finotello, J. E. Bara, D. Camper, and R. D. Noble, “Room-temperature ionic liquids: Temperature dependence of gas solubility selectivity,” *Ind. Eng. Chem. Res.*, vol. 47,

no. 10, pp. 3453–3459, 2008.

[152] M. Ramdin *et al.*, "Solubility of the Precombustion Gases CO_2, CH_4, CO, H_2, N_2, and H_2S in the Ionic Liquid [bmim][Tf_2N] from Monte Carlo Simulations," *J. Phys. Chem. C*, vol. 118, no. 41, pp. 23599–23604, 2014.

[153] J. E. Bara *et al.*, "Gas separations in fluoroalkyl-functionalized room-temperature ionic liquids using supported liquid membranes," *Chem. Eng. J.*, vol. 147, no. 1, pp. 43–50, 2009.

[154] A. I. Labropoulos *et al.*, "Alkyl-methylimidazolium tricyanomethanide ionic liquids under extreme confinement onto nanoporous ceramic membranes," *J. Phys. Chem. C*, vol. 117, no. 19, pp. 10114–10127, 2013.

[155] A. Finotello, J. E. Bara, S. Narayan, D. Camper, and R. D. Noble, "Ideal gas solubilities and solubility selectivities in a binary mixture of room-temperature ionic liquids," *J. Phys. Chem. B*, vol. 112, no. 8, pp. 2335–2339, 2008.

[156] S. M. Mahurin, J. S. Lee, G. A. Baker, H. Luo, and S. Dai, "Performance of nitrile-containing anions in task-specific ionic liquids for improved CO2/N2 separation," *J. Memb. Sci.*, vol. 353, no. 1–2, pp. 177–183, 2010.

[157] J. Jacquemin, M. F. Costa Gomes, P. Husson, and V. Majer, "Solubility of carbon dioxide, ethane, methane, oxygen, nitrogen, hydrogen, argon, and carbon monoxide in 1-butyl-3-methylimidazolium tetrafluoroborate between temperatures 283 K and 343 K and at pressures close to atmospheric," *J. Chem. Thermodyn.*, vol. 38, no. 4, pp. 490–

502, 2006.

[158] K. Fujie, T. Yamada, R. Ikeda, and H. Kitagawa, “Introduction of an Ionic Liquid into the Micropores of a Metal-Organic Framework and Its Anomalous Phase Behavior,” *Angew. Chemie - Int. Ed.*, vol. 53, no. 42, pp. 11302–11305, 2014.

[159] F. W. M. da Silva *et al.*, “CO $_2$ Adsorption on Ionic Liquid—Modified Cu-BTC: Experimental and Simulation Study,” *Adsorpt. Sci. Technol.*, vol. 33, no. 2, pp. 223–242, 2015.

[160] T. J. H. Vlugt and M. Schenk, “Influence of framework flexibility on the adsorption properties of hydrocarbons in the zeolite silicalite,” *J. Phys. Chem. B*, vol. 106, no. 49, pp. 12757–12763, 2002.

[161] M. G. Martin and J. I. Siepmann, “Transferable Potentials for Phase Equilibria. 1. United-Atom Description of n -Alkanes,” *J. Phys. Chem. B*, vol. 102, no. 97, pp. 2569–2577, 1998.

[162] W. L. Jorgensen, D. S. Maxwell, and J. Tirado-Rives, “Development and testing of the OPLS all-atom force field on conformational energetics and properties of organic liquids,” *J. Am. Chem. Soc.*, vol. 118, no. 45, pp. 11225–11236, 1996.

[163] A. L. Myers, J. A. Calles, and G. Calleja, “Comparison of molecular simulation of adsorption with experiment,” *Adsorption*, vol. 3, pp. 107–115, 1997.

[164] J. Jiang, Ed., *Metal-organic frameworks: Materials modeling towards potential engineering applications*. CRC Press, 2015.

[165] A. L. Myers and P. A. Monson, "Physical adsorption of gases: the case for absolute adsorption as the basis for thermodynamic analysis," *Adsorption*, vol. 20, no. 4, pp. 591–622, 2014.

[166] A. Auroux, *Calorimetry and Thermal Methods in Catalysis*, vol. 154. Springer Berlin Heidelberg, 2013.

[167] O. Talu and A. L. Myers, "Molecular simulation of adsorption: Gibbs dividing surface and comparison with experiment," *AIChE J.*, vol. 47, no. 5, pp. 1160–1168, 2001.

[168] W. Zhou, H. Wu, M. R. Hartman, and T. Yildirim, "Hydrogen and methane adsorption in metal-organic frameworks: A high-pressure volumetric study," *J. Phys. Chem. C*, vol. 111, no. 44, pp. 16131–16137, 2007.

[169] O. Talu and A. L. Myers, "Reference potentials for adsorption of helium, argon, methane, and krypton in high-silica zeolites," *Colloids Surfaces A Physicochem. Eng. Asp.*, vol. 187–188, pp. 83–93, 2001.

[170] D. D. Do, D. Nicholson, and H. D. Do, "On the Henry constant and isosteric heat at zero loading in gas phase adsorption," *J. Colloid Interface Sci.*, vol. 324, no. 1–2, pp. 15–24, 2008.

[171] P. J. Linstrom and W. G. Mallard, "NIST Chemistry webBook, NIST Standard Reference Database Number 69," *Natl. Inst. Stand. Technol.*, no. 69, p. 20899, 2014.

[172] S. K. Nune, P. K. Thallapally, A. Dohnalkova, C. Wang, J. Liu, and G. J. Exarhos, "Synthesis and properties of nano zeolitic imidazolate frameworks.," *Chem. Commun.*,

vol. 46, no. 27, pp. 4878–80, 2010.

[173] S. R. Venna and M. A. Carreon, “Highly permeable zeolite imidazolate framework-8 membranes for CO 2/CH4 separation,” *J. Am. Chem. Soc.*, vol. 132, no. 1, pp. 76–78, 2010.

[174] A. Battisti, S. Taioli, and G. Garberoglio, “Zeolitic imidazolate frameworks for separation of binary mixtures of CO2, CH4, N2 and H2: A computer simulation investigation,” *Microporous Mesoporous Mater.*, vol. 143, no. 1, pp. 46–53, 2011.

[175] L. Zhang, G. Wu, and J. Jiang, “Adsorption and Diffusion of CO 2 and CH 4 in Zeolitic Imidazolate Framework-8: Effect of Structural Flexibility,” *J. Phys. Chem. C*, vol. 118, no. 17, pp. 8788–8794, 2014.

[176] D. Liu, Y. Wu, Q. Xia, Z. Li, and H. Xi, “Experimental and molecular simulation studies of CO2 adsorption on zeolitic imidazolate frameworks: ZIF-8 and amine-modified ZIF-8,” *Adsorption*, vol. 19, no. 1, pp. 25–37, 2013.

[177] D. Fairen-Jimenez *et al.*, “Flexibility and swing effect on the adsorption of energy-related gases on ZIF-8: combined experimental and simulation study.,” *Dalton Trans.*, vol. 41, no. 35, pp. 10752–62, 2012.

[178] F. L. Smith and A. H. Harvey, “Avoid common pitfalls when using Henry ’s law,” *Chem. Eng. Prog.*, no. September, pp. 33–39, 2007.

[179] R. Sander, “Compilation of Henry’s law constants (version 4.0) for water as solvent,” *Atmos. Chem. Phys.*, vol. 15, no. 8, pp. 4399–4981, 2015.

[180] T. R. Gaffney, J. F. Kirner, R. Kumar, R. J. Maliszewskyj, and W. P. Schmidt, "O2 VSA process with low O2 capacity adsorbents," US Patent 5,266,102, 30-Nov-1993.

[181] M. W. Ackley, "Multilayer adsorbent beds for PSA gas separation," European Patent number 0875279A2, 04-Nov-1998.

[182] M. W. Ackley, A. B. Stewart, G. W. Henzler, F. W. Leavitt, F. Notaro, and M. S. Kane, "PSA apparatus and process using adsorbent mixtures," US Patent 6,027,548, 22-Feb-2000.

[183] F. Notaro, J. T. Mullhaupt, F. W. Leavitt, and M. W. Ackley, "Adsorption process and system using multilayer adsorbent beds," U.S. Patent 5,810,909, Sep-1998.

[184] S. Rege and R. Yang, "A simple parameter for selecting an adsorbent for gas separation by pressure swing adsorption," *Sep. Sci. Technol.*, vol. 36, no. 15, pp. 3355–3365, 2001.

[185] C. Graham, D. A. Imrie, and R. E. Raab, "Measurement of the electric quadrupole moments of CO2, CO, N2, Cl2 and BF3," *Mol. Phys.*, vol. 93, no. 1, pp. 49–56, 1998.

[186] M. Ramdin *et al.*, "Solubility of the Precombustion Gases CO2, CH4, CO, H2, N2, and H2S in the Ionic Liquid [bmim][Tf2N] from Monte Carlo Simulations," *J. Phys. Chem. C*, vol. 118, no. 41, pp. 23599–23604, 2014.

[187] Y. Hou and R. E. Baltus, "Experimental Measurement of the Solubility and Diffusivity of CO_2 in Room-Temperature Ionic Liquids Using a Transient Thin-Liquid-Film Method," *Ind. Eng. Chem. Res.*, vol. 46, no. 24, pp. 8166–8175, 2007.

[188] L. F. Zubeir *et al.*, "Thermophysical properties of imidazolium tricyanomethanide ionic liquids: experiments and molecular simulation," *Phys. Chem. Chem. Phys.*, vol. 18, no. 33, pp. 23121–23138, 2016.

[189] N. Vergadou, E. Androulaki, J.-R. Hill, and I. G. Economou, "Molecular simulations of imidazolium-based tricyanomethanide ionic liquids using an optimized classical force field," *Phys. Chem. Chem. Phys.*, vol. 18, no. 9, pp. 6850–6860, 2016.

[190] T. Koller, J. Ramos, N. M. Garrido, A. P. Frba, and I. G. Economou, "Development of a united-atom force field for 1-ethyl-3-methylimidazolium tetracyanoborate ionic liquid," *Mol. Phys.*, vol. 110, no. 11–12, pp. 1115–1126, 2012.

[191] Z. Liu, X. Wu, and W. Wang, "A novel united-atom force field for imidazolium-based ionic liquids.," *Phys. Chem. Chem. Phys.*, vol. 8, no. 9, pp. 1096–1104, 2006.

[192] T. M. Koller, J. Ramos, P. S. Schulz, I. G. Economou, M. H. Rausch, and A. P. Fröba, "Thermophysical Properties of Homologous Tetracyanoborate-Based Ionic Liquids Using Experiments and Molecular Dynamics Simulations," *J. Phys. Chem. B*, vol. 121, no. 16, pp. 4145–4157, 2017.

[193] T. M. Koller *et al.*, "Thermophysical Properties of the Ionic Liquids [EMIM][B(CN) $_4$] and [HMIM][B(CN) $_4$]," *J. Phys. Chem. B*, vol. 117, no. 28, pp. 8512–8523, 2013.

[194] B. Assfour, S. Leoni, and G. Seifert, "Hydrogen adsorption sites in zeolite imidazolate frameworks ZIF-8 and ZIF-11," *J. Phys. Chem. C*, vol. 114, no. 31, pp. 13381–13384, 2010.

[195] W. Xue *et al.*, "Effects of ionic liquid dispersion in metal-organic frameworks and covalent organic frameworks on CO2 capture: A computational study," *Chem. Eng. Sci.*, vol. 140, pp. 1–9, 2016.

[196] G. E. Keller, "Gas-Adsorption Processes: State of the Art," in *Industrial Gas Separations*, vol. 223, American Chemical Society, 1983, pp. 145–169.

[197] C. W. Skarstrom, "Method and apparatus for fractionating gas mixtures by adsorption," U.S. patent 2, 944, 627, 1958.

[198] D. Daniel and M. P. G. De, "Process for separating a binary gaseous mixture by adsorption," US Patent 3,155,468, Nov-1964.

[199] Y. S. Bae and R. Q. Snurr, "Development and evaluation of porous materials for carbon dioxide separation and capture," *Angewandte Chemie - International Edition*, vol. 50, no. 49. pp. 11586–11596, 2011.

[200] G. Sneddon, A. Greenaway, and H. H. P. Yiu, "The Potential Applications of Nanoporous Materials for the Adsorption, Separation, and Catalytic Conversion of Carbon Dioxide," *Adv. Energy Mater.*, vol. 4, no. 10, p. 1301873, 2014.

APPENDIX A

ZIF-8 force field parameters

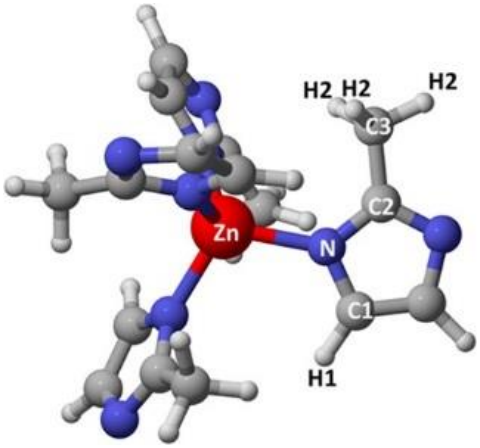

$$u(r_{ij}) = 4\varepsilon_{ij}\left[\left(\frac{\sigma_{ij}}{r_{ij}}\right)^{12} - \left(\frac{\sigma_{ij}}{r_{ij}}\right)^{6}\right] + \frac{1}{4\pi\epsilon_o}\frac{q_i q_j}{r_{ij}}$$

Table A-1: LJ and Coulombic parameters for ZIF-8

Site-site	Partial Charge q (e)	σ (Å)	ε/k_B (K)
Zn	+1.3429	1.96	6.290
N	-0.6822	3.25	85.548
H1	+0.0912	2.51	7.548
H2	+0.0499	2.65	7.900
C1	-0.0622	3.40	43.772
C2	+0.7551	3.40	43.277
C3	-0.2697	3.40	55.053

$$u(l) = \frac{k_l}{2}(l - l_o)^2$$

Table A-2: Bond stretching potential parameters for ZIF-8

Bonds	l_0 ($\dot{A}$)	k_l (kJ mol^{-1} nm^{-2})
Zn−N	2.048	52802.1
N−C2	1.360	257818.1
N−C1	1.376	253048.3
C1−C1	1.375	339991.8
C1−H1	1.077	327690.9
C2−C3	1.498	203760.8
C3−H2	1.091	286855.0

$$u(\theta) = \frac{k_\theta}{2}(\theta - \theta_o)^2$$

Table A-3: Angle bending potential parameters for ZIF-8

Angles	θ_0 (degrees)	k_θ (kJ mol^{-1} rad^{-2})
N−Zn−N	109.5	296.23
Zn−N−C2	130.3	462.74
Zn−N−C1	125.1	475.30
C1−N−C2	104.5	1077.80
C1−C1−N	107.9	909.61
C1−C1−H1	130.6	552.29
C2−C3−H2	108.1	317.98
H2−C3−H2	113.8	955.63
N−C2−N	123.1	958.97
N−C2−C3	121.5	549.78

$$u(\varphi) = k_\varphi[1 + \cos(m\varphi - \varphi_o)^2]$$

Table A-4: Torsional potential parameters for ZIF-8

Dihedrals	φ_0 (degrees)	m	k_φ (kJ mol^{-1})
N−C1−C1−N	180	2	90
N−C1−C1−H1	180	2	90
C1−C1−N−Co	180	2	25.1
C1−C1−N−C2	180	2	25.1
C3−C2−N−Co	180	2	41.8
C3−C2−N−C1	180	2	41.8

APPENDIX B

Force field parameters for gas molecules

$$u(r_{ij}) = 4\varepsilon_{ij}\left[\left(\frac{\sigma_{ij}}{r_{ij}}\right)^{12} - \left(\frac{\sigma_{ij}}{r_{ij}}\right)^{6}\right] + \frac{1}{4\pi\epsilon_o}\frac{q_i q_j}{r_{ij}}$$

Table B- 1 LJ and Coulombic Parameters (Adsorbates) in the TraPPE Potential

Adsorbate	UA	Partial Charge q (e)	σ ($\dot{A}$)	ε/k_B (K)
CH_4	CH_4	0.000	3.73	148.00
CO_2	C	+0.700	2.80	27.00
	O	-0.350	3.05	79.00
N_2	N	-0.482	3.31	36.00
	M	+0.964	0.00	0.00

$$u(l) = \frac{k_l}{2}(l - l_o)^2$$

$$u(\theta) = \frac{k_\theta}{2}(\theta - \theta_o)^2$$

Table B- 2: Bonds length and angles in the TraPPE-UA potential

Adsorbate	Angle	θ_0 (degrees)	Bond	l_0 ($\dot{A}$)
CH_4	N/A	N/A	N/A	N/A
CO_2	O-C-O	180.0	C-O	1.16
N_2	N-M-N	180.0	N-M	0.55

$$u(r_{ij}) = 4\varepsilon_{ij}\left[\left(\frac{\sigma_{ij}}{r_{ij}}\right)^{12} - \left(\frac{\sigma_{ij}}{r_{ij}}\right)^{6}\right] + \frac{1}{4\pi\epsilon_o}\frac{q_i q_j}{r_{ij}}$$

Table B- 3: Parameters of different methane molecular models

Model	Site	Partial Charge q (e)	σ ($\dot{A}$)	ε/k_B (K)
OPLS-AA	C	-0.240	3.50	32.21
	H	0.060	2.50	15.10
OPLS-UA	CH_4	0.000	3.73	147.90
TraPPE-EH	C	0.000	3.31	0.00
	M	0.000	3.31	15.30
TraPPE-UA	CH_4	0.000	3.73	148.00

APPENDIX C

Ionic liquids (ILs) force field parameters

1-Butyl-3 methylimidazolium bis(trifluoromethanesulfonyl)Imide

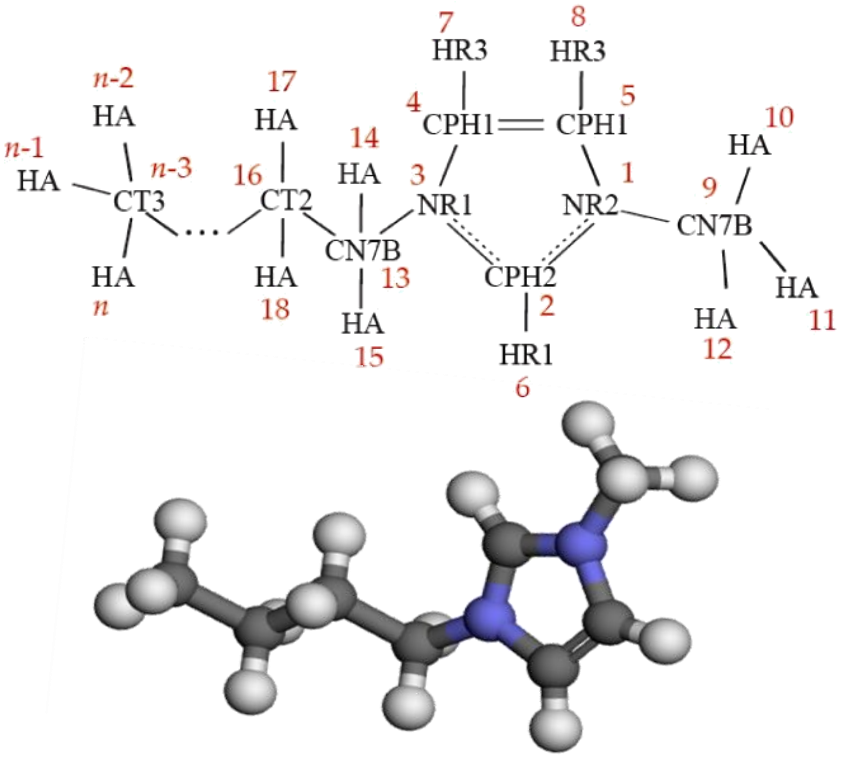

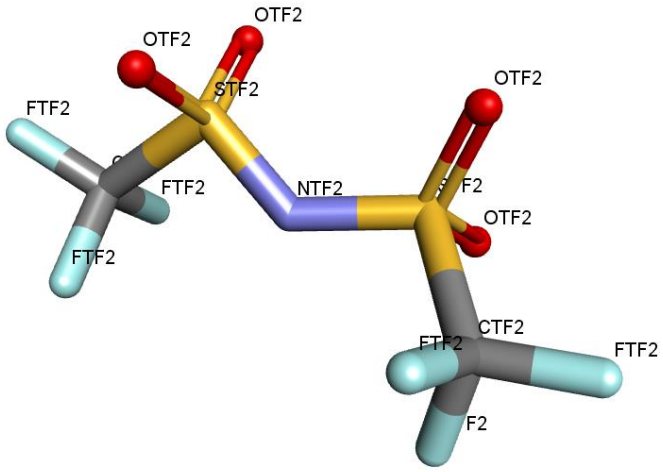

$$u(r_{ij}) = 4\varepsilon_{ij}\left[\left(\frac{\sigma_{ij}}{r_{ij}}\right)^{12} - \left(\frac{\sigma_{ij}}{r_{ij}}\right)^{6}\right] + \frac{1}{4\pi\epsilon_o}\frac{q_i q_j}{r_{ij}}$$

Table C.1- 1: Partial charges and LJ parameters for [Tf_2N^-]

Atom	Partial Charge q (e)	σ ($\dot{A}$)	ε/k_B (K)
CTF2	0.348789	3.499	33.212
FTF2	-0.131010	2.951	26.671
STF2	0.858581	3.549	125.805
OTF2	-0.534882	2.960	105.676
NTF2	-0.449451	3.250	85.547

$$u(r_{ij}) = 4\varepsilon_{ij}\left[\left(\frac{\sigma_{ij}}{r_{ij}}\right)^{12} - \left(\frac{\sigma_{ij}}{r_{ij}}\right)^{6}\right] + \frac{1}{4\pi\epsilon_o}\frac{q_i q_j}{r_{ij}}$$

Table C.1- 2: Partial charges and LJ parameters for [$bmim^+$]

Atom	Partial Charge q (e)	σ ($\dot{A}$)	ε/k_B (K)
NR1	0.146046	3.296	100.644
CPH1	-0.006432	3.207	25.161
NR2	0.092254	3.296	100.644
CPH2	-0.193107	3.207	25.161
CPH2	-0.152475	3.207	25.161
HR1	0.208287	1.604	23.148
HR2	0.205544	2.616	3.925
HR3	0.184183	2.616	3.925
CN7B	-0.171877	4.054	10.064
HA	0.119267	2.352	11.071
HA	0.148216	2.352	11.071

HA	0.087322	2.352	11.071
CN7B	0.005903	4.054	10.064
HA	0.054165	2.352	11.071
HA	0.045561	2.352	11.071
CT2	0.076942	3.875	27.677
HA	-0.029155	2.352	11.071
HA	0.000652	2.352	11.071
CT2	0.227458	3.875	27.677
HA	-0.024423	2.352	11.071
HA	-0.051806	2.352	11.071
CT3	-0.261600	3.671	40.258
HA	0.061505	2.352	11.071
HA	0.051733	2.352	11.071
HA	0.136136	2.352	11.071

$$u(l) = \frac{k_l}{2}(l - l_o)^2$$

Table C.1- 3: Bond stretching potential parameters for [bmim$^+$] in [bmim][Tf$_2$N]

Atom 1	Atom 2	k_l (kcal mol^{-1} $\dot{A}^{-2}$)	l_0 ($\dot{A}$)
CN7B	NR1	220.00	1.4762
CN7B	NR2	220.00	1.4762
CPH1	NR1	400.00	1.3819
CPH1	NR2	400.00	1.3819
CPH2	NR1	400.00	1.3366
CPH2	NR2	400.00	1.3366
CPH1	CPH1	410.00	1.3610

CPH2	HR1	340.00	1.0779
CPH1	HR3	365.00	1.0775
CN7B	HA	309.00	1.0889
CT2	HA	309.00	1.0954
CT3	HA	322.00	1.0935
CN7B	CT2	200.00	1.5308
CT2	CT2	222.50	1.5373
CT2	CT3	222.50	1.5314
CT1	CN7B	200.00	1.5240
CT1	HA	322.00	1.0893

$$u(\theta) = \frac{k_\theta}{2}(\theta - \theta_o)^2$$

Table C.1- 4: Angle bending potential parameters for [bmim$^+$] in [bmim][Tf_2N]

Atom 1	Atom 2	Atom 3	k_θ (kcal mol^{-1} rad^{-2})	θ_0 (degrees)
CT2	CN7B	NR1	140.00	112.34
CPH1	NR1	CPH2	130.00	108.25
CPH1	NR2	CPH2	130.00	108.25
HA	CN7B	NR1	30.00	109.41
HA	CN7B	NR2	30.00	109.41
HR1	CPH2	NR1	25.00	125.44
HR1	CPH2	NR2	25.00	125.44
NR1	CPH1	CPH1	130.00	107.28
NR2	CPH1	CPH1	130.00	107.28
NR1	CPH2	NR2	130.00	109.11
HR3	CPH1	CPH1	25.00	130.74

NR2	CPH1	HR3	25.00	122.04
NR1	CPH1	HR3	25.00	122.04
HA	CN7B	HA	35.50	108.44
HA	CN7B	CT2	33.40	111.68
HA	CT2	CN7B	33.40	109.13
CN7B	CT2	CT2	58.35	111.50
CT2	CT2	CT3	58.00	112.34
CT2	CT2	CT2	58.00	112.34
HA	CT2	HA	35.50	106.13
HA	CT3	HA	35.50	107.24
CT2	CT2	HA	26.50	108.43
CT2	CT3	HA	34.60	111.62
CT3	CT2	HA	34.60	109.47
CN7B	NR2	CPH2	130.00	125.75
CN7B	NR1	CPH2	130.00	125.75
CN7B	NR2	CPH1	130.00	125.67
CN7B	NR1	CPH1	130.00	125.67
HA	CT1	HA	35.50	108.27
HA	CT1	CN7B	33.40	110.64
HA	CN7B	CT1	33.40	111.58
NR1	CN7B	CT1	140.00	112.31

$$u(\chi) = k_{\chi}[1 + \cos(m\chi - \delta)]$$

Table C.1- 5: Torsional potential parameters for [bmim^{+}] in [bmim][Tf$_2$N]

Atom 1	Atom 2	Atom 3	Atom 4	k_{χ} (kcal mol^{-1})	n	δ (deg)
CPH2	NR1	CPH1	CPH1	14.000	2	180
CPH2	NR2	CPH1	CPH1	14.000	2	180
NR1	CPH1	CPH1	NR2	14.000	2	180
NR1	CPH2	NR2	CPH1	14.000	2	180
NR2	CPH2	NR1	CPH1	14.000	2	180
HR1	CPH2	NR1	CPH1	3.000	2	180
HR1	CPH2	NR2	CPH1	3.000	2	180
HR3	CPH1	CPH1	HR3	2.000	2	180
CPH1	CPH1	NR1	CN7B	0.000	1	0
CPH1	CPH1	NR2	CN7B	0.000	1	0
HR3	CPH1	NR2	CPH2	3.000	2	180
HR3	CPH1	NR1	CPH2	3.000	2	180
NR1	CPH1	CPH1	HR3	3.000	2	180
NR2	CPH1	CPH1	HR3	3.000	2	180
NR1	CPH2	NR2	CN7B	0.000	2	180
NR2	CPH2	NR1	CN7B	0.000	2	180
HR1	CPH2	NR1	CN7B	0.000	2	180
HR1	CPH2	NR2	CN7B	0.000	2	180
HR3	CPH1	NR1	CN7B	0.000	2	180
HR3	CPH1	NR2	CN7B	0.000	2	180
CPH2	NR1	CN7B	HA	0.195	2	180

CPH2	NR2	CN7B	HA	0.195	2	180
CPH1	NR2	CN7B	HA	0.000	3	0
CPH1	NR1	CN7B	HA	0.000	3	0
CPH2	NR1	CN7B	CT2	0.100	3	180
CPH1	NR1	CN7B	CT2	0.200	4	0
NR1	CN7B	CT2	CT2	0.000	3	0
HA	CT2	CT3	HA	0.160	3	0
CT2	CT2	CT3	HA	0.160	3	0
NR1	CN7B	CT2	HA	0.000	3	0
CN7B	CT2	CT2	CT3	0.150	1	0
HA	CN7B	CT2	HA	0.195	3	0
CT2	CT2	CN7B	HA	0.195	3	0
HA	CT2	CT2	CN7B	0.195	3	0
HA	CT2	CT2	HA	0.195	3	0
HA	CT2	CT2	CT3	0.195	3	0
HA	CT1	CN7B	HA	0.195	3	0
HA	CT1	CN7B	NR1	0.000	3	0
CT1	CN7B	NR1	CPH2	0.100	3	180
CT1	CN7B	NR1	CPH1	0.200	4	0

$$u(\psi) = k_{\psi}(\psi - \psi_0)^2$$

Table C.1- 6: Improper torsional potential parameters for [bmim$^+$] in [bmim][Tf_2N]

Atom 1	Atom 2	Atom 3	Atom 4	$k\psi$ (kcal mol^{-1} rad^{-2})	ψ (degrees)
CPH2	NR1	NR2	HR1	0.5	0
NR1	CPH1	CPH2	CN7B	0.6	0

NR2	CPH1	CPH2	CN7B	0.6	0
CPH1	CPH1	NR2	HR3	0.5	0
CPH1	CPH1	NR1	HR3	0.5	0

$$u(l) = \frac{k_l}{2}(l - l_o)^2$$

Table C.1- 7: Bond stretching potential parameters for [Tf_2N^{-1}]

Atom 1	Atom 2	k_l (kcal mol^{-1} $\dot{A}^{-2}$)	l_0 ($\dot{A}$)
CTF2	FTF2	441.80	1.3230
CTF2	STF2	235.42	1.8180
STF2	OTF2	637.07	1.4420
NTF2	STF2	372.01	1.5700

$$u(\theta) = \frac{k_\theta}{2}(\theta - \theta_o)^2$$

Table C.1- 8: Angle bending potential parameters for [Tf_2N^{-1}]

Atom 1	Atom 2	Atom 3	k_θ (kcal mol^{-1} rad^{-2})	θ_0 (degrees)
FTF2	CTF2	FTF2	93.33	107.10
STF2	CTF2	FTF2	82.93	111.80
CTF2	STF2	OTF2	103.97	102.80
OTF2	STF2	OTF2	115.80	118.50
OTF2	STF2	NTF2	94.51	113.60
CTF2	STF2	NTF2	97.51	100.20
STF2	NTF2	STF2	80.19	125.60

$$u(\chi) = k_{\chi}[1 + \cos(m\chi - \delta)]$$

Table C.1- 9: Torsional potential parameters for [Tf_2N^{-1}]

Atom 1	Atom 2	Atom 3	Atom 4	k_{χ} (kcal mol^{-1})	n	δ (degrees)
FTF2	CTF2	STF2	OTF2	0.1734	3	0
STF2	NTF2	STF2	OTF2	-0.0018	3	0
FTF2	CTF2	STF2	NTF2	0.1580	3	0
STF2	NTF2	STF2	CTF2	7.8329	1	0
				-2.4904	2	180
				-0.7636	3	0

1-Butyl-3 methylimidazolium tricyanomethanide

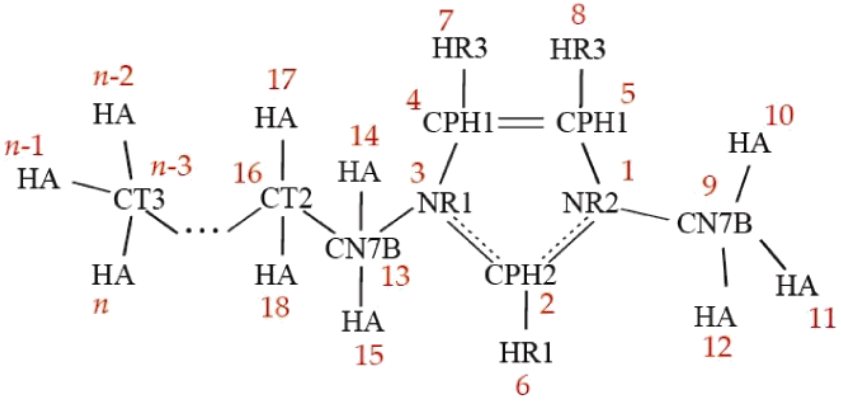

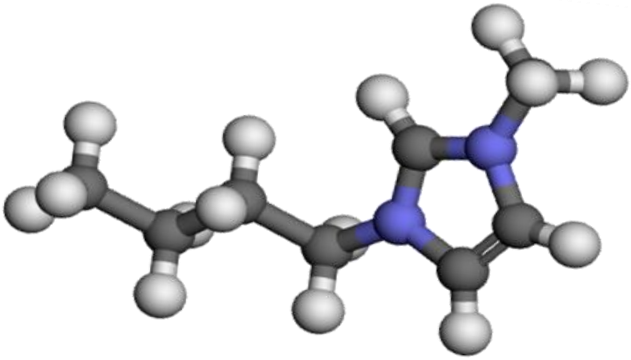

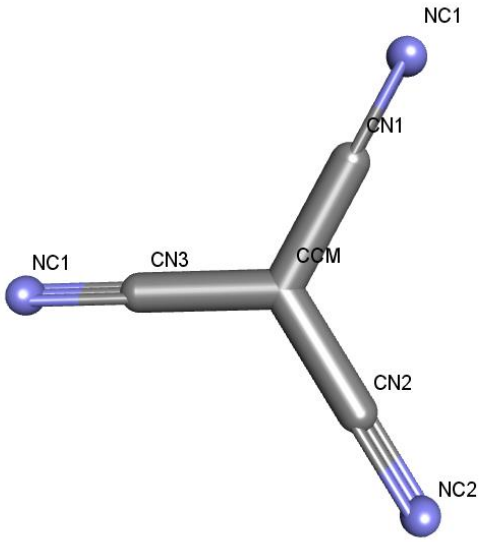

$$u(r_{ij}) = \frac{1}{4\pi\epsilon_o}\frac{q_i q_j}{r_{ij}}$$

Table C.2- 1: Partial charges for [TCM$^-$]

Atom	Average charge (e)
CCM	-0.4903
CN	0.4690
CN	0.4872
CN	0.4845
NC	-0.5625
NC	-0.5507
NC	-0.5727
Total	-0.7355

$$u(r_{ij}) = \frac{1}{4\pi\epsilon_o}\frac{q_i q_j}{r_{ij}}$$

Table C.2- 2: Partial charges for [bmim$^+$] in [bmim][TCM]

Atom	Average charge (e)	Atom	Average charge (e)
NR2	0.1664	HA	0.0170
CPH2	-0.0849	HA	-0.0796
NR1	0.1632	CT2	0.1861

CPH1	0.0032	HA	-0.0802
CPH1	0.0069	HA	-0.1106
HR1	0.1326	CT2	0.2262
HR3	0.0423	HA	-0.0988
HR3	0.0348	HA	-0.1239
CN7B	0.4601	CT3	0.4702
HA	-0.1643	HA	-0.1566
HA	-0.1301	HA	-0.1748
HA	-0.0270	HA	-0.1925
CN7B	0.2498		

$$u(r_{ij}) = 4\varepsilon_{ij}\left[\left(\frac{\sigma_{ij}}{r_{ij}}\right)^{12} - \left(\frac{\sigma_{ij}}{r_{ij}}\right)^{6}\right]$$

Table C.2- 3: LJ parameters for [TCM$^-$]

Atom	σ ($\dot{A}$)	ε/k_B (K)
CCM	3/546	12.077
CN	3.118	65.419
NC	3.065	196.256

$$u(l) = \frac{k_l}{2}(l - l_o)^2$$

Table C.2- 4: Bond stretching potential parameters for [TCM$^-$]

Atom 1	Atom 2	k_l (kcal mol^{-1} $\dot{A}^{-2}$)	l_0 ($\dot{A}$)

CCM	CN	430.00	1.408
CN	NC	1210.0	1.167

$$u(\theta) = \frac{k_\theta}{2}(\theta - \theta_o)^2$$

Table C.2- 5: Angle bending potential parameters for [TCM$^-$]

Atom 1	Atom 2	Atom 3	k_θ (kcal mol^{-1} rad^{-2})	θ_0 (degrees)
NC	CN	CCM	30.0	179.99
CN	CCM	CN	44.0	120.00

$$u(\chi) = k_\chi[1 + \cos(m\chi - \delta)]$$

Table C.2- 6: Torsional potential parameters for [TCM$^-$]

Atom 1	Atom 2	Atom 3	Atom 4	k_χ (kcal mol^{-1})	n	δ (degrees)
NC	CN	CCM	CN	0.00	2	180

$$u(\psi) = k_\psi(\psi - \psi_0)^2$$

Table C.2- 7: Improper torsional potential parameters for [TCM$^-$]

Atom 1	Atom 2	Atom 3	Atom 4	k_ψ (kcal mol^{-1} rad^{-2})	Ψ_0 (degrees)
CCM	CN	CN	NC	26.7	0

$$u(l) = \frac{k_l}{2}(l - l_o)^2$$

Table C.2- 8: Bond stretching potential parameters for [bmim$^+$] in [bmim][TCM]

Atom 1	Atom 2	k_l (kcal mol^{-1} $\dot{A}^{-2}$)	l_0 ($\dot{A}$)
CN7B	NR1	220.00	1.4762
CN7B	NR2	220.00	1.4762
CPH1	NR1	400.00	1.3819
CPH1	NR2	400.00	1.3819
CPH2	NR1	400.00	1.3366
CPH2	NR2	400.00	1.3366
CPH1	CPH1	410.00	1.3610
CPH2	HR1	340.00	1.0779
CPH1	HR3	365.00	1.0775
CN7B	HA	309.00	1.0889
CT2	HA	309.00	1.0954
CT3	HA	322.00	1.0935
CN7B	CT2	200.00	1.5308
CT2	CT2	222.50	1.5373
CT2	CT3	222.50	1.5314
CT1	CN7B	200.00	1.5240
CT1	HA	322.00	1.0893

$$u(\theta) = \frac{k_\theta}{2}(\theta - \theta_o)^2$$

Table C.2- 9: Angle bending potential parameters for [bmim$^+$] in [bmim][TCM]

Atom 1	Atom 2	Atom 3	k_θ (kcal mol^{-1} rad^{-2})	θ_0 (degrees)
CT2	CN7B	NR1	140.00	112.34
CPH1	NR1	CPH2	130.00	108.25
CPH1	NR2	CPH2	130.00	108.25
HA	CN7B	NR1	30.00	109.41
HA	CN7B	NR2	30.00	109.41
HR1	CPH2	NR1	25.00	125.44
HR1	CPH2	NR2	25.00	125.44
NR1	CPH1	CPH1	130.00	107.28
NR2	CPH1	CPH1	130.00	107.28
NR1	CPH2	NR2	130.00	109.11
HR3	CPH1	CPH1	25.00	130.74
NR2	CPH1	HR3	25.00	122.04
NR1	CPH1	HR3	25.00	122.04
HA	CN7B	HA	35.50	108.44
HA	CN7B	CT2	33.40	111.68
HA	CT2	CN7B	33.40	109.13
CN7B	CT2	CT2	58.35	111.50
CT2	CT2	CT3	58.00	112.34
CT2	CT2	CT2	58.00	112.34
HA	CT2	HA	35.50	106.13
HA	CT3	HA	35.50	107.24
CT2	CT2	HA	26.50	108.43

CT2	CT3	HA	34.60	111.62
CT3	CT2	HA	34.60	109.47
CN7B	NR2	CPH2	130.00	125.75
CN7B	NR1	CPH2	130.00	125.75
CN7B	NR2	CPH1	130.00	125.67
CN7B	NR1	CPH1	130.00	125.67
HA	CT1	HA	35.50	108.27
HA	CT1	CN7B	33.40	110.64
HA	CN7B	CT1	33.40	111.58
NR1	CN7B	CT1	140.00	112.31

$$u(\chi) = k_{\chi}[1 + \cos(m\chi - \delta)]$$

Table C.2- 10: Torsional potential parameters for [bmim^{+}] in [bmim][TCM]

Atom 1	Atom 2	Atom 3	Atom 4	k_{χ} (kcal mol^{-1})	n	δ (degrees)
CPH2	NR1	CPH1	CPH1	14.000	2	180
CPH2	NR2	CPH1	CPH1	14.000	2	180
NR1	CPH1	CPH1	NR2	14.000	2	180
NR1	CPH2	NR2	CPH1	14.000	2	180
NR2	CPH2	NR1	CPH1	14.000	2	180
HR1	CPH2	NR1	CPH1	3.000	2	180
HR1	CPH2	NR2	CPH1	3.000	2	180
HR3	CPH1	CPH1	HR3	2.000	2	180
CPH1	CPH1	NR1	CN7B	0.000	1	0
CPH1	CPH1	NR2	CN7B	0.000	1	0
HR3	CPH1	NR2	CPH2	3.000	2	180
HR3	CPH1	NR1	CPH2	3.000	2	180

NR1	CPH1	CPH1	HR3	3.000	2	180
NR2	CPH1	CPH1	HR3	3.000	2	180
NR1	CPH2	NR2	CN7B	0.000	2	180
NR2	CPH2	NR1	CN7B	0.000	2	180
HR1	CPH2	NR1	CN7B	0.000	2	180
HR1	CPH2	NR2	CN7B	0.000	2	180
HR3	CPH1	NR1	CN7B	0.000	2	180
HR3	CPH1	NR2	CN7B	0.000	2	180
CPH2	NR1	CN7B	HA	0.195	2	180
CPH2	NR2	CN7B	HA	0.195	2	180
CPH1	NR2	CN7B	HA	0.000	3	0
CPH1	NR1	CN7B	HA	0.000	3	0
CPH2	NR1	CN7B	CT2	0.100	3	180
CPH1	NR1	CN7B	CT2	0.200	4	0
NR1	CN7B	CT2	CT2	0.000	3	0
HA	CT2	CT3	HA	0.160	3	0
CT2	CT2	CT3	HA	0.160	3	0
NR1	CN7B	CT2	HA	0.000	3	0
CN7B	CT2	CT2	CT3	0.150	1	0
HA	CN7B	CT2	HA	0.195	3	0
CT2	CT2	CN7B	HA	0.195	3	0
HA	CT2	CT2	CN7B	0.195	3	0
HA	CT2	CT2	HA	0.195	3	0
HA	CT2	CT2	CT3	0.195	3	0
HA	CT1	CN7B	HA	0.195	3	0
HA	CT1	CN7B	NR1	0.000	3	0
CT1	CN7B	NR1	CPH2	0.100	3	180

CT1	CN7B	NR1	CPH1	0.200	4	0

$$u(\psi) = k_{\psi}(\psi - \psi_0)^2$$

Table C.2- 11: Improper torsional potential parameters for [bmim$^+$] in [bmim][TCM]

Atom 1	Atom 2	Atom 3	Atom 4	k_{ψ} (kcal mol^{-1} rad^{-2})	ψ (degrees)
CPH2	NR1	NR2	HR1	0.5	0
NR1	CPH1	CPH2	CN7B	0.6	0
NR2	CPH1	CPH2	CN7B	0.6	0
CPH1	CPH1	NR2	HR3	0.5	0
CPH1	CPH1	NR1	HR3	0.5	0

1-Butyl-3 methylimidazolium tertracyanoborate

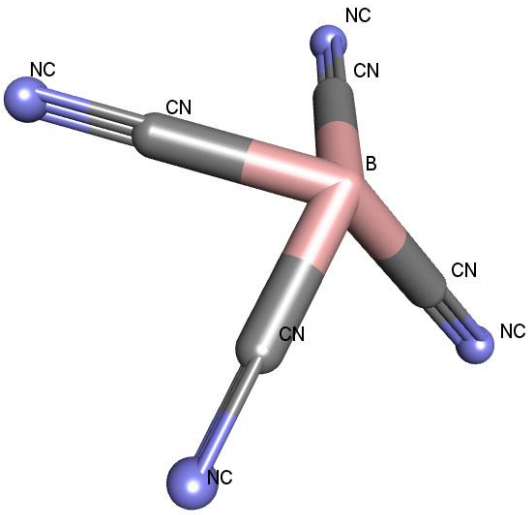

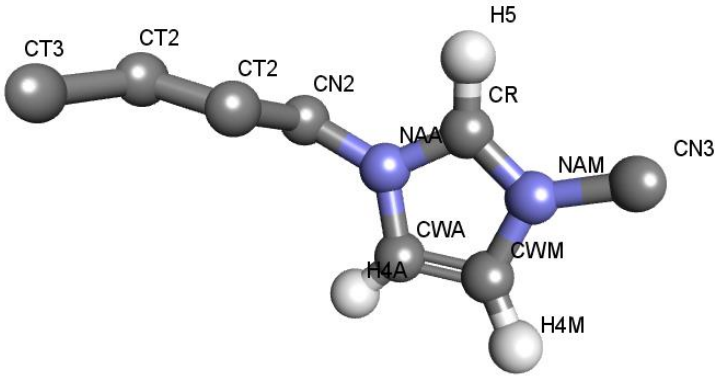

$$u(r_{ij}) = 4\varepsilon_{ij}\left[\left(\frac{\sigma_{ij}}{r_{ij}}\right)^{12} - \left(\frac{\sigma_{ij}}{r_{ij}}\right)^{6}\right] + \frac{1}{4\pi\epsilon_o}\frac{q_i q_j}{r_{ij}}$$

Table C.3- 1: Partial charges for [$B(CN)_4^-$] in [bmim][$B(CN)_4$]

Atom	Partial Charge q (e)	σ ($\dot{A}$)	ε/kB (K)
B	0.3386	3.581	0.120
CN	0.1406	3.3	33.207
NC	-0.4381	3.25	61.339

$$u(r_{ij}) = 4\varepsilon_{ij}\left[\left(\frac{\sigma_{ij}}{r_{ij}}\right)^{12} - \left(\frac{\sigma_{ij}}{r_{ij}}\right)^{6}\right] + \frac{1}{4\pi\epsilon_o}\frac{q_i q_j}{r_{ij}}$$

Table C.3- 2: LJ and Coulombic parameters for [$bmim^+$] in [bmim][$B(CN)_4$]

Atom	Partial Charge q (e)	σ ($\dot{A}$)	ε/kB (K)
CR	-0.005	3.4	43.2740
NAM	-0.0414	3.25	85.5497
NAA	-0.0755	3.25	85.5497
CWM	-0.189	3.4	43.2740
CWA	-0.1412	3.4	43.2740
CN2	0.2742	3.822	71.7064
CN3	0.286	3.813	94.9430
CT2	0.0198	3.947	67.1120
CT3	0.0098	3.902	92.9465
H4M	0.2451	2.511	7.5531
H4A	0.2287	2.511	7.5531
H5	0.2201	1.782	7.5531

$$u(l) = \frac{k_l}{2}(l - l_o)^2$$

Table C.3- 3: Bond stretching potential parameters for [bmim$^-$] and [B(CN)$_4^-$]

Bonds	l_0 ($\dot{A}$)	k_l (kcal mol^{-1} $\dot{A}^{-2}$)
CW–H4	1.07	1611
CR–H5	1.07	1590
CR–NA	1.325	1674
CW–NA	1.378	1506
CW–CW	1.343	1715
CN3–NA	1.472	1409
CN2–NA	1.472	1409
CN2–CT2	1.526	1087
CT2–CT2	1.526	1087
CT2–CT3	1.526	1087
B-CN	1.572	1213
CN-NC	1.157	795.0

$$u(\theta) = \frac{k_\theta}{2}(\theta - \theta_o)^2$$

Table C.3- 4: Angle bending potential parameters for [bmim$^-$] and [B(CN)$_4^-$]

Angle	k_θ (K rad^{-2})	θ (degrees)
NA–CN2–CT2	35239.80	112.2
CN2–CT2–CT2	31631.63	109.5
CT2–CT2–CT3	31631.63	109.5
CW–NA–CN3	25136.92	125.7
CR–NA–CN3	25136.92	126.3
CW–NA–CN2	25136.92	125.7
CR–NA–CN2	25136.92	126.3

CW–CW–NA	60376.73	107.1
CR–NA–CW	60376.73	108
NA–CR–NA	60376.73	109.9
H4–CW–NA	15154.32	122.1
H5–CR–NA	15154.32	125.7
CW–CW–H4	15154.32	130.7
B-CN-NC	25136.92	180
CN-NC-CN	25136.92	109.47

$$u(\chi) = k_{\chi}[1 + \cos(m\chi - \delta)]$$

Table C.3- 5: Torsional potential parameters for [bmim$^-$] and [B(CN)$_4^-$]

Torsional	k_{χ} (kJ mol^{-1})	δ (degrees)	n
NA–CR–NA–CW	50.21	180	2
NA–CR–NA–CT3	8.368	180	2
NA–CR–NA–CT2	8.368	180	2
H5–CR–NA–CW	6.276	180	2
H5–CR–NA–CT3	6.276	180	2
H5–CR–NA–CT2	6.276	180	2
CW–CW–NA–CR	50.21	180	2
CW–CW–NA–CT3	8.368	180	2
CW–CW–NA–CT2	8.368	180	2
H4–CW–NA–CR	8.368	180	2
H4–CW–NA–CT3	6.276	180	2
H4–CW–NA–CT2	6.276	180	2
NA–CW–CW–H4	6.276	180	2
NA–CW–CW–NA	50.21	180	2
H4–CW–CW–H4	6.276	180	2
CN2–CT2–CT2–CT3	4.18	0	3

CT2–CT2–CT2–CT3	4.18	0	3
NA–CN2–CT2–CT2	4.18	0	3
CT2–CN2–NA–CW	-0.745	0	1
CT2–CN2–NA–CR	-0.987	0	1

$$\boldsymbol{u(\psi) = k_{\psi}[1 + \cos(m\psi - \delta)]}$$

Table C.3- 6: Improper torsional potential parameters for [bmim$^-$] and [B(CN)$_4^-$]

Torsion	k_{ψ} (kJ mol^{-1})	δ (degrees)	n
NA–NA–CR–H5	4.602	180	2
CW–NA–CW–H4	4.602	180	2
CR–CW–NA–CN3	4.184	180	2
CR–CW–NA–CN2	4.184	180	2

APPENDIX D

Mathematical derivations

Langmuir adsorption isotherm from statistical thermodynamics

The partition function for a single adsorbed molecule, in the harmonic oscillator approximation, is;

$$q(T) = q_x q_y q_z \exp(-\frac{U_{00}}{k_B T}) \tag{D.1-1}$$

$$Q_{NVT} = A\, q(T)^N;\ A = \frac{M!}{N!\,(M-N)!} \tag{D.1-2}$$

A is the number of ways N indistinguishable molecules can be distributed among labeled sites. Using Stirling's theorem;

$$\ln N\,! = N \ln N - N \tag{D.1-3}$$

$$\ln Q = N \ln(A\, q) \tag{D.1-4}$$

$$\ln Q = N \ln A + N \ln q \tag{D.1-5}$$

$$\ln Q = N \ln M! - N \ln N! - N\ \ln((M-N)!) + N \ln q \tag{D.1-6}$$

$$\ln Q = N\,(M \ln M - M) - N\,(N \ln N - N) - N\,(\,(M-N)\ln(M-N) - M + N) + N \ln q \tag{D.1-7}$$

$$\ln Q = M \ln M - N \ln N - (M-N)\ln(M-N) + N \ln q \tag{D.1-8}$$

$$\frac{\mu}{k_B T} = -\left(\frac{\partial \ln q}{\partial N}\right)_{M,T} = -\left(\frac{\partial (M \ln M - N \ln N - (M-N)\ln(M-N) + N \ln q)}{\partial N}\right)_{M,T} \tag{D.1-9}$$

$$\frac{\mu}{k_B T} = \ln N + 1 - \ln(M-N) - 1 - \ln q \tag{D.1-10}$$

$$\frac{\mu}{k_B T} = \ln \frac{N}{(M-N)q} \tag{D.1-11}$$

$$Given\ \theta = \frac{N}{M}\ ; Fractional\ coverage$$

$$ideal\ gas: \mu(p,T) = \mu^0(T) + k_B T \ln p \tag{D.1-12}$$

$$\frac{\mu}{k_B T} = \ln \frac{\theta}{(1-\theta)q} \tag{D.1-13}$$

$$\frac{\mu}{k_B T} = \ln \frac{\theta}{(1-\theta)q} = \frac{\mu_{gas}}{k_B T} = \frac{\mu^0(T)}{k_B T} + \ln p \tag{D.1-14}$$

$\frac{\theta}{1-\theta} = q\ p \exp(\frac{\mu^0(T)}{k_B T})$; Langmuir adsorption isotherm (D.1-15)

APPENDIX E

Density values calculated from mc simulations and from NIST database

In all mass density calculations for the studied fluid, the statistical uncertainty is less than 0.01

Table E- 1: Density for supercritical CH_4 at 250 K

P (bar)	NIST density (kg m^{-3})	MC density (kg m^{-3})
200.0	223.23	224.84
250.0	250.65	251.14
300.0	270.18	269.30

Table E- 2: Density for liquid C_4H_{10} at 300 K

P (bar)	NIST density (kg m^{-3})	MC density (kg m^{-3})
10	570.56	571.99
30	573.65	575.40
50	578.79	578.61
70	581.75	581.65
100	586.78	585.97

Table E- 3: Density values for liquid C_3H_8 at 300 K

P (bar)	NIST density (kg m^{-3})	MC density (kg m^{-3}) with no tail corrections	MC density (kg m^{-3}) with tail correction
10	570.56	484.01	489.71
30	573.65	491.58	494.41
50	578.79	500.44	501.04
70	581.75	504.76	506.65
100	586.78	510.73	512.85

Table E- 4: VLE density values for CH_4 at different temperatures

T (K)	NIST liquid density (kg m^{-3})	MC liquid density (kg m^{-3})	NIST vapor density (kg m^{-3})	MC vapor density (kg m^{-3})
105.0	431.92	431.19	1.06	0.97
135.0	385.64	381.73	7.85	8.15
160.0	336.31	335.34	25.38	24.59
180.0	276.23	287.02	61.38	59.19
190.0	200.78	238.72	125.18	100.20